Gran Sasso Science Institute

Scuola Internazionale Superiore di Studi Avanzati

Non linear cosmic ray transport and cosmic ray driven galactic winds

PhD thesis

submitted October 30, 2016

PhD Candidate

Sarah Recchia

Advisor

Pasquale Blasi
INAF and Gran Sasso Science Institute

Advisor

Giovanni Morlino
Gran Sasso Science Institute

Gran Sasso Science Institute

Ciclo XXIX – A.A 2013-2016

Contents

Introduction

The bulk of Cosmic Rays (CRs) reaching our planet is likely of Galactic origin and is thought to be accelerated in sources located in the Galactic disk (mainly Supernova remnants (SNRs)). The energy density of Galactic CRs, $\sim$ 1 eV/cm^3, can be accounted for if one assumes that 3-10% of the mechanical energy injected by SNe in the Galaxy is channeled into accelerated particles.
The observed large residence time of CRs in the Galaxy (compared to the time required for ballistic propagation of relativistic particles on Galactic distances) suggests that Galactic CRs are well coupled to the interstellar medium (ISM) and are likely to undergo diffusive motion, due to scattering off magnetic turbulence in the ISM.
Most of current models of CR propagation treat the CR transport properties (such as the diffusion coefficient and the size of the propagation region) as fitting parameters and do not take into account the possible active role of CRs in determining them. In fact, the escape of CRs from the Galaxy leads to a gradient in the CR distribution function which can cause the excitation of Alfvén waves, due to CR streaming instability, that in turn determine the scattering properties of CRs, namely their diffusive transport. In addition, the CR pressure gradient can act as a force on the background plasma, directed away from the Galactic disk. If this force is large enough to win against gravity (due to Dark Matter, gas and stars), a wind can be launched, which affects the CR convective transport.
The dynamics of CR-driven winds in the presence of self-generated turbulence is intrinsically non-linear. In fact, the CR density gradient determines the wind properties (velocity, pressure, magnetic field) and the excitation of the plasma waves which cause CR diffusion. On the other hand, Galactic winds could have a sizable effect on the CR distribution function, by advecting CRs out of the Galaxy, by influencing their spectral features, by affecting their radial distribution in the Galactic disk but also, possibly, by reaccelerating them at the wind termination shock (see Zirakashvili & Voelk (2006)). In addition, in such a scenario the CR diffusion coefficient, convection velocity and the size of the propagation region are not pre-assigned, but rather they are derived self-consistently with the CR distribution function.
The importance of Galactic winds is not only restricted to CR physics. In

fact, galactic outflows have been observed in many galaxies and constitute an important ingredient in the galactic evolution. For instance, galactic winds affect the amount of gas available and pollute the galactic halos with hot plasma and metals, thus influencing the properties of the ISM and the star formation rate. As for the Milky Way, observations have not yet provided a clear answer as to the existence of such outflows, although the detection of absorption lines in the X-ray band (Oxygen O_{VII} and O_{VIII} lines) show the presence of a hot dilute gas in the Galactic halo and the recent observation of the so called Fermi Bubbles in the Galactic Center region are likely to be connected with Galactic winds.
Galactic winds may be powered by several mechanisms, for instance by thermal and radiation pressure gradients. However those mechanisms are unlikely to occur in the Milky Way, with the only possible exception of the Galactic Center region, since thermal and radiation pressure gradients are expected to be too small. Nevertheless, the CR pressure gradient may provide the force necessary to launch winds, making CR-driving an appealing mechanism for wind formation in our Galaxy.

In this thesis we solve the coupled system of the hydrodynamic equations for CR-driven winds and for the CR transport in such winds. In our approach the CR transport is due to diffusion on self-generated Alfvén waves and to advection with these waves and with the wind. We then apply our solution method to the Milky Way and we investigate: 1) how the wind launching depends on the properties of the ISM (gas density and temperature, Galactic magnetic field), on the CR pressure and on the Galactic gravitational potential (including the Dark Matter halo); 2) the implications of CR-driven winds on the observed CR proton spectrum; 3) the effect of non-linear CR propagation in the presence of self-generated diffusion, both with and without CR-driven winds, on the CR distribution function in the Galaxy as a function of the Galactocentric distance, and we compare our predictions with the observed radial CR density and spectral slope, as inferred from observations of γ-rays.

Chapter 1

Cosmic Ray transport and Galactic winds

In Sec. 1.1 we briefly summarize the main properties of the observed CR spectrum, in terms of spectral features, energy density, chemical composition and anisotropy and we report the main aspects of the current paradigm for the origin of Galactic CRs, i.e the SNR paradigm. We focus in particular on the diffusive Galactic CR propagation model and on its effects on the CR spectrum and on the abundances of secondary spallation nuclei. We also explore the possible occurrence and implications of non-linear transport processes, such as the self-generation of plasma waves due to CR streaming instability and CR-driven Galactic outflows, and we briefly discuss the possible effects of the neutral gas in the ISM on CR propagation.
In Sec. 1.2 we discuss the observational evidence and importance of winds in other galaxies for the galactic evolution and for the ISM and intergalactic medium (IGM) properties and we summarize their main powering mechanisms. As for the Milky Way, we report observations which seem to indicate the presence of winds in our own Galaxy (despite the existence of such winds as not yet been proven) and we discuss the possible role of CR-driving. Finally, we report the state of the art of the modeling of CR-driven winds.
We conclude in Sec. 1.4 with an overview of the thesis work.

1.1 Galactic Cosmic Rays and their transport

CRs are charged particles accelerated to very high energies which travel through the Universe and reach the Earth. They are directly detected at Earth with balloon, satellite and air-shower detectors, but are also indirectly tracked through the products of their interaction with the ISM: synchrotron radiation at radio frequencies due to CR electrons and diffuse gamma radiation due to the decay of π_0, produced by CR protons interactions and by CR electrons (by bremsstrahlung and inverse Compton).

The energy density of CRs at the position of the Sun is $\sim$ 1 eV/cm^3. The CR hadronic flux measured at the Earth is composed by protons ($\sim$ 87%), Helium ($\sim$ 12%) and heavier nuclei ($\sim$ 1%) and reaches energies of $\sim 10^{20}$ eV, while the leptonic flux is $\sim$ 100 times smaller and reaches energies of $\sim 10^{14}$ eV. The all-particle CR spectrum is shown in Fig. 1.1. Remarkably, the CR spectrum is very close to a broken power law, extending form $\sim$ 30 GeV up to $\sim 10^{20}$ eV for the hadronic component. Below $\sim$ 30 GeV the spectrum is affected by solar modulation.

A spectral break, called the "knee", occurs at $E_{knee} \approx 3 \times 10^{15}$ eV, where the spectral slope changes from $\propto E^{-2.7}$ to $\propto E^{-3.1}$ and the chemical composition seems to become heavier. At larger energies the chemical composition is still debated. A second spectral break, called the "ankle", occurs at $E_{ankle} \approx 3 \times 10^{18}$ eV, where the CR spectrum flattens to $\propto E^{-2.7}$.
Also below the knee the CR spectrum presents an interesting feature detected most clearly in the proton and Helium spectra: the PAMELA experiment found a spectral hardening at $\sim$ 230 GV, where the slope of the proton spectrum changes from $\gamma = 2.89 \pm 0.015$ to $\gamma = 2.67 \pm 0.03$ (see Adriani et al. (2011)). The same result has been confirmed also by the AMS-02 experiment (see Aguilar et al. (2015)).
Important information on the CR propagation through the Galaxy can be gathered from the abundances of secondary spallation nuclei relative to their primary nuclei (e.g B/C), from the abundances of radioactive secondaries (e.g ^{10}Be), and from the CR anisotropy. For instance, the B/C ration as a function of the energy is shown in Fig. 1.2, and appears to decrease with energy, while the CR anisotropy is quite small ($\sim$ 0.001 at TeV energies).
Any theory of the origin of CRs has to be able to explain in a unified framework all these aspects: the spectral features, the maximum energy, the chemical composition and the degree of anisotropy (see e.g Berezinskii et al. (1990) for an extensive review of CR physics).

Nowadays, the bulk of CRs (presumably up to energies of $\sim 10^{17}$ eV) is thought to be accelerated at the shocks of supernova remnants (SNRs) located in the Galactic disk and to propagate diffusively in the Galaxy due to scattering on magnetic inhomogeneities. The Galactic magnetic field plays a prominent role in the confinement process. In particular, the presence of a random component for the magnetic field causes the pitch angle scattering of CRs and provides their spatial diffusion. The scattering process is of resonant nature, so that CRs with Larmor radius $r_L = \frac{pc}{ZeB}$ will be scattered by magnetic waves with wave number $k = \frac{1}{r_L}$.
The idea of SNRs as the accelerators of Galactic CRs has been put forward in the '30s (Baade & Zwicky (1934)), while the argument was made in a more quantitative form in the '60s (Ginzburg & Syrovatsky (1961)), based on energetic considerations. In fact, the energy density of CRs can be accounted for if one assumes that $3-10\%$ of the mechanical energy released by

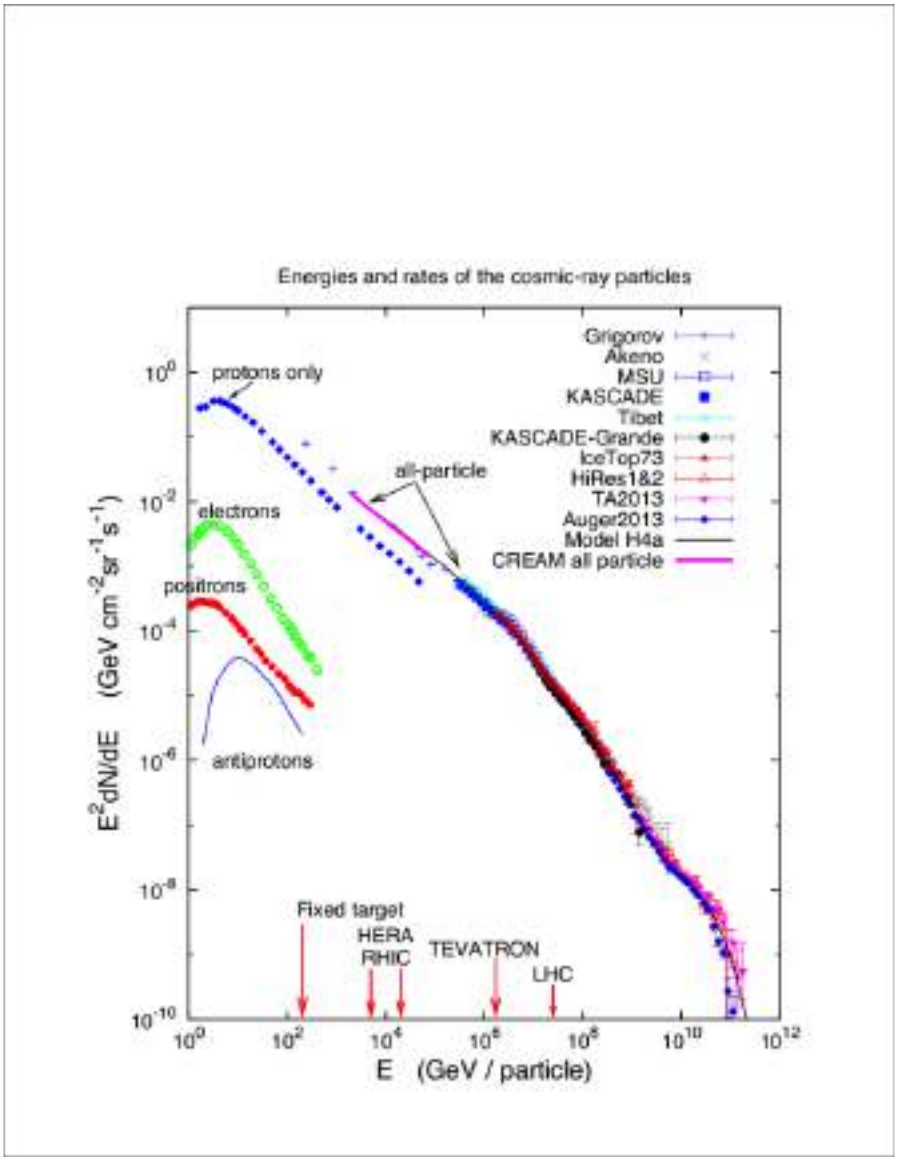

Figure 1.1: Spectrum of cosmic rays at the Earth. The all-particle spectrum measured by different experiments is plotted, together with the proton spectrum. The contributions from electrons, positrons and antiprotons as measured by the PAMELA experiment are also shown.

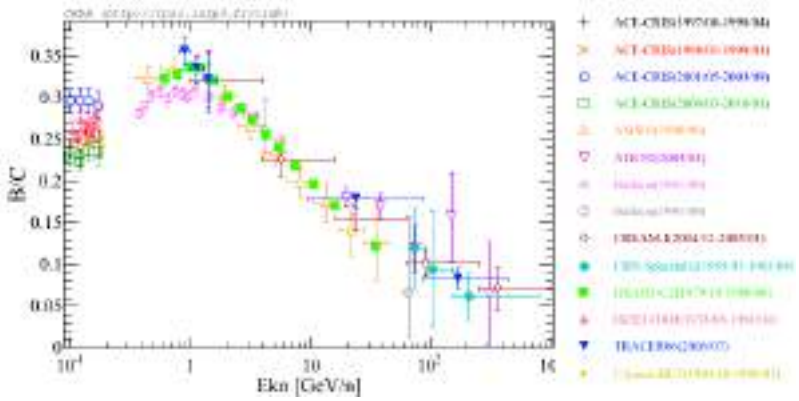

Figure 1.2: B/C ratio as a function of energy per nucleon. Data have been extracted from the Cosmic Ray Database (Maurin et al. (2014)).

SNe in the Galaxy is channeled into accelerated particles. The mechanism invoked for CR acceleration at SN shocks is the so called diffusive shock acceleration (DSA), which predicts a power law spectrum. Since the energy channeled into CRs during the acceleration process is quite large ($3-10\%$ of the mechanical energy released in the SN explosion), the dynamical reaction of accelerated particles can have important effects on the shock structure, leading to nonlinearities in the acceleration process. This aspect is investigated in the non linear theory of DSA. A presentation of the theory of DSA is beyond the scope of the present work and we refer the reader to (Blasi (2013)) for an extensive review.
The fact that CRs are accelerated at SN shocks is also confirmed by numerous observations in radio, X-rays and $\gamma-$rays from SNRs, however it still remain unproven that SNRs can accelerate CRs up to the knee. The combination of DSA and diffusive propagation in the Galaxy constitute a robust theoretical framework for the origin of Galactic CRs which has become a real paradigm.
In this framework the main features of CRs reported above can be interpreted as follows:1) the nearly power law spectrum is a natural consequence of the acceleration mechanism 2) the knee results from the CR acceleration mechanism being rigidity dependent. In fact, if $E \approx 3\times10^{15}$ GeV is the maximum energy achieve by protons in SN shocks, heavier nuclei with charge Z will reach an energy Z times larger. Fe nuclei could thus reach an energy 26 times larger than the protons and the knee would result from the superposition of the cut-offs of different nuclei. 3) The observed small anisotropy and the abundances of spallation secondary nuclei can be explained by the diffusive CR propagation. The decrease in the B/C ratio with energy can be accounted for with a diffusion coefficient which increases with energy, i.e with a poorer confinement of CRs of higher energies. 4) The spectral hardening at

$\sim$ 230 GV is presumably due to transport effects. For instance Tomassetti (2012) showed that a spatially dependent diffusion coefficient may lead to a spectral hardening. Blasi et al. (2012) and Aloisio & Blasi (2013) showed that a spectral hardening may naturally appear as the transition from scattering on self-generated turbulence to scattering on a pre-existing turbulence. 5) CR with energies beyond the "ankle", called *Ultra High Energy Cosmic Rays* (UHECRs), are thought to be of extragalactic origin, since they cannot be confined in the Galaxy, given that their Larmor radius in the typical Galactic magnetic field is of the same order of the Galactic size. Notice however that the transition energy from Galactic to extragalactic CRs is still matter of debate.

1.1.1 Diffusive propagation of Galactic Cosmic Rays

The current paradigm describes the Galactic CR transport as a diffusion process off magnetic waves, in which also CR advection, due to the scattering waves themselves and/or to large scale motion of the ISM is considered, together with possible energy loss and gain, nuclear fragmentation, and radioactive decay of unstable nuclei. The CR distribution function can be calculated once the CR injection term, the shape of the propagation region and the boundary conditions for the problems have been assigned.
Usually in those models it is assumed that CRs do not play a dynamical role in their transport and that the Galactic halo is static and has a preassigned geometry. In most cases the CR diffusion coefficient and advection velocity are considered to be the same in the whole Galaxy and are treated as fitting parameters, together with the size of the propagation volume. The same happens also for many of more complicated models, in which, for instance, inhomogeneities of the diffusion coefficient and breaks in the injection spectrum are included: the model features are treated as fitting parameters and do not derive from physical arguments (see e.g Berezinskii et al. (1990); Blasi (2014); Ptuskin (2006)).
In what follows we illustrate a basic version of the CR diffusion model, in which we assume that the CR propagation occurs only perpendicular to the Galactic disk and the Galaxy is schematized as a cylinder of radius $R \sim 15 - 20$ kpc and total height $2H$ with $H \gtrsim 3$ kpc. The CR sources are located in a thin disk of thickness $2h$ ($\sim$ 300 pc) and the CR diffusion coefficient and advection velocity are preassigned and spatially independent. Despite the simple picture, this model retains the most important characteristics of more sophisticated scenarios, in particular the scaling with energy of the resulting CR spectrum and the relation between the diffusion coefficient and the B/C ratio.

Convection-diffusion equation for protons

The stationary convection-diffusion equation for CR protons (neglecting possible energy gain or loss) reads

$$-\frac{\partial}{\partial z}\left[D\frac{\partial f}{\partial z}\right]+u\frac{\partial f}{\partial z}-\frac{d\,u}{d\,z}\frac{p}{3}\frac{\partial f}{\partial p}=Q(z,p), \tag{1.1}$$

where z and p are the distance from the Galactic disk and the particle momentum respectively, $f(z,p)$ is the CR distribution function, $u(z)$ is the advection velocity (which may be due to the presence of winds and/or to convection with Alfvén waves), $D(z,p)$ is the CR diffusion coefficient and $Q(z,p)$ is the CR injection term. Notice that we are assuming that the CR propagation is one-dimensional and only occurs perpendicular to the Galactic disk.
We solve this equation under the following simplifying assumptions: the diffusion coefficient $D(p)$ only depends on momentum, the advection velocity is constant in z and directed away from the disk (thus $\frac{d\,u}{d\,z}=2u\delta(z)$), the injection occurs at the Galactic disk ($Q(z,p)=Q_0(p)\delta(z)$) and the injection spectrum is a power law in momentum (where ξ_{CR} is the CR injection efficiency (typically $\sim 10\%$), E_{SN} is the energy released by a SN explosion ($\sim 10^{51}$erg), $\mathcal{R}_{SN}$ is the rate of SN explosions ($\sim 1/30\,\mathrm{yr}^{-1}$), and $I(\gamma)$ is a normalization factor)

$$Q_0(p)=\frac{\xi_{CR}E_{SN}\mathcal{R}_{SN}}{I(\gamma)c(mc)^4}\left(\frac{p}{mc}\right)^{-\gamma}. \tag{1.2}$$

Finally, we assume that the halo height H is fixed, and that at $|z|=H$ CRs escape freely from the Galaxy, i.e $f(z,H)=0$. Notice that this condition is necessary to guarantee the stationarity of the problem.
Eq. 1.1 can be solved by integrating between 0^+ and a generic $z<H$ with the boundary condition $f(0,p)=f_0(p)$ and $f(H,p)=0$, which gives

$$f(z,p)=f_0(p)\frac{1-\exp^{-\zeta(1-\frac{z}{H})}}{1-\exp^{-\zeta}}, \tag{1.3}$$

where $\zeta(p)=\frac{u\,H}{D(p)}$. The expression of $f_0(p)$ can be obtained by integration of Eq. 1.1 around the disk and reminding that $\frac{d\,u}{d\,z}=2u\delta(z)$:

$$-2D(p)\left[\frac{\partial f}{\partial z}\right]_{z=0^+}-\frac{2}{3}u\,p\frac{d\,f_0}{d\,p}=Q_0(p). \tag{1.4}$$

Calculating $\left[\frac{\partial f}{\partial z}\right]_{z=0^+}$ from Eq. 1.3 we get

$$\left[\frac{\partial f}{\partial z}\right]_{z=0^+}=\frac{u\,f_0}{D(p)}\frac{1}{\lambda(p)}, \tag{1.5}$$

where $\lambda(p) = 1 - \exp^{\zeta(p)}$. Finally one can solve for the spectrum in the disk:

$$f_0(p) = \frac{3}{2\,u}\int_p^\infty \frac{dp'}{p'} Q_0(p) \exp\left[\int_p^{p'} \frac{d\,p''}{p''}\frac{3}{\lambda(p'')}\right]. \tag{1.6}$$

Two interesting limits of Eq. 1.6 can be obtained in the advection-dominated regime ($\frac{u\,H}{D(p)} \gg 1$) and in the diffusion-dominated regime ($\frac{u\,H}{D(p)} \ll 1$): in the assumption that $D(p) \sim p^\delta$ is also a power law in momentum we get

$$f_0^{diff}(p) = \frac{Q_0(p)\,H}{2\,D(p)} \sim p^{-\gamma-\delta} \tag{1.7}$$

$$f_0^{adv}(p) = \frac{Q_0(p)}{2\,u} \sim p^{-\gamma}. \tag{1.8}$$

As deduced from the energy dependence of the B/C ratio (see below), the CR diffusion coefficient is an increasing function of momentum, which here we model as a power law. In this scenario, for low enough CR energy, advection dominates over diffusion and the observed CR spectrum has roughly the injection slope. At increasing CR energy, diffusion becomes more and more important and causes a steepening of the CR spectrum. At the energies for which diffusion is dominant the spectral slope reduces to the sum of the injection and diffusion coefficient slope $\gamma + \delta$. The comparison with the CR data allows to estimate the model parameters. Typical values of such parameters are: injection slope $\gamma \sim 4.1$, diffusion coefficient with slope $\delta \sim 0.6$ and a characteristic value of $\sim 3 \times 10^{28}$ cm^2/s at ~ 1 GeV, halo size of $H \sim 4$ kpc and advection velocity of ~ 20 km/s.

Diffusion equation and B/C ratio

If we consider the convection-diffusion equation for primary nuclei (such as Carbon) we have to include the spallation term in Eq. 1.1, i.e the nuclear fission due to collisions of primary nuclei with nuclei of the ISM. For simplicity here we also assume that $u = 0$ and Eq. 1.1 becomes

$$-\frac{\partial}{\partial z}\left[D\frac{\partial f}{\partial z}\right] + \frac{f}{\tau_{sp}} = Q_0(p)\delta(z), \tag{1.9}$$

where the spallation time scale is given by

$$\tau_{sp} = \frac{1}{n_{ISM}\sigma_{sp}v} \tag{1.10}$$

and n_{ISM} is the density of the ISM, σ_{sp} is the spallation cross section and v is the particle velocity. Notice that n_{ISM} depends on z and it is larger in the disk. Here we approximate it as $n_{ISM} \simeq 2\,h\,n_d\delta(z)$, i.e we assume that the

spallation process only occurs in the disk, of density n_d and half-thickness h. Eq. 1.9 thus becomes

$$-\frac{\partial}{\partial z}\left[D\frac{\partial f}{\partial z}\right] = Q_0(p)\delta(z) - 2\,h\,n_d\,v\,\sigma_{sp}\delta(z)\,f. \tag{1.11}$$

This equation can be solved in the same way and with the same boundary conditions at $z = 0$ and $z = H$ as Eq. 1.1: integration between 0^+ and $z < H$ and integration around the disk gives respectively

$$f(z,p) = f_0(p)\frac{H - |z|}{H} \tag{1.12}$$

and

$$f_0(p) = \frac{Q_0(p)\frac{H}{2\,D}}{1 + \frac{h}{H}n_d v\sigma_{sp}\frac{H^2}{D(p)}}. \tag{1.13}$$

Notice that $\frac{h}{H}n_d$ is the average density felt by CRs during their Galactic propagation, while $\frac{H^2}{D}$ is the diffusion time and $\frac{H}{hn_d v\sigma_{sp}}$ is the effective spallation time. The grammage (matter thickness traversed by CRs during their propagation) is defined as

$$\chi(p) = m_p\left(n_d\frac{h}{H}\right)v\left(\frac{H^2}{D}\right), \tag{1.14}$$

where m_p is the proton mass. We also define $\chi_{sp} = \frac{m_p}{\sigma_{sp}}$. Notice that if $\chi(p) \gg \chi_{sp}$ the primary CR undergoes many spallation processes during their diffusive propagation. This is due to the fact that in this limit the diffusion time is much larger that the spallation time. In the opposite limit, diffusion is much faster than spallation. Eq. 1.13 becomes

$$f_0(p) = \frac{Q_0(p)}{2n_d h m_p v}\frac{1}{\frac{1}{\chi(p)} + \frac{1}{\chi_{sp}}}. \tag{1.15}$$

We have the two limits of strong and weak spallation:

$$\chi(p) \gg \chi_{sp}\ \text{(strong spallation)} \qquad f_0(p) \longrightarrow \frac{Q_0(p)}{2n_d h m_p v}\chi_{sp} \tag{1.16}$$

$$\chi(p) \ll \chi_{sp}\ \text{(weak spallation)} \qquad f_0(p) \longrightarrow Q_0(p)\frac{H}{2\,D}. \tag{1.17}$$

Thus, when spallation dominates, the spectrum at the disk will have roughly the injection slope (the same effect of advection), while in the limit of weak spallation we recover the diffusion-dominated regime. Since $D(p)$ is an increasing function of momentum spallation may dominate at low energies (usually less than 1 GeV).

Given those considerations, in this framework we can write the Carbon spectrum at the disk as

$$f_C(p) = \frac{Q_C(p)}{2n_d h m_p v} \frac{1}{\frac{1}{\chi_C(p)} + \frac{1}{\chi_{C,sp}}}. \tag{1.18}$$

As for Boron, which is a secondary nucleus produced (mostly) from Carbon, the transport equation is the same (notice that Boron also undergoes spallation in the ISM), with the only difference that the injection term is due to the spallation of Carbon:

$$Q_B(p)dp = 2\,h\,n_d\,v\,\sigma_{sp} f_C\left(p'\right) dp', \tag{1.19}$$

where $\frac{dp'}{dp} = \frac{A}{A-1}$ and A is the atomic number of Carbon. The Boron spectrum in the disk is thus given by

$$f_B(p) = \frac{Q_B(p)}{2n_d h m_p v} \frac{1}{\frac{1}{\chi_B(p)} + \frac{1}{\chi_{B,sp}}} \tag{1.20}$$

$$Q_B(p) = 2\,h\,n_d\,v\,\sigma_{sp} f_C\left(\frac{A}{A-1}p\right) \frac{A}{A-1}. \tag{1.21}$$

For the B/C ratio we get

$$\frac{f_B(p)}{f_C(p)} \approx \frac{1}{\frac{\chi_{C,sp}}{\chi_B(p)} + \frac{\chi_{C,sp}}{\chi_{B,sp}}}. \tag{1.22}$$

In the limit in which diffusion dominate over spallation (this happens at large enough energies) we get the important result

$$\frac{f_B(p)}{f_C(p)} \approx \frac{\chi_B(p)}{\chi_{C,sp}} \propto \frac{1}{D(p)}, \tag{1.23}$$

i.e by measuring the B/C ratio as function of the energy we can also estimate the Galactic CR diffusion coefficient. Notice that for larger diffusion coefficient the confinement time is smaller, resulting in smaller abundances of secondary nuclei.

1.1.2 Non-linear Cosmic Ray transport: self-generation and Galactic winds

We have seen that many models of Galactic CR propagation do not take into account the possible role of CRs in determining their own transport properties. However, the observed secular escape of CRs from the Galaxy, together with the fact that the Galactic CR energy density is comparable

with the thermal and magnetic energy densities, poses the question of the importance of the dynamical role of CRs due to their gradient in the Galaxy. The CR back reaction may largely affect both CR diffusion and convection. In fact, it is known that the gradient in the CR distribution leads to the excitation of the so called "streaming instability" (see e.g Skilling (1975)), which causes the generation of Alfvén waves, which move in the direction of the decreasing CR density. Those waves can resonate with CRs, thus increasing their scattering frequency and affecting their diffusion coefficient. The streaming instability is assumed to be saturated due to non-linear Landau damping (NLLD) (see e.g Zhou & Matthaeus (1990)).
Such process is non-linear, since CRs play and active role in determining their transport properties. Streaming instability may provide a mechanism of self-confinement for CRs in the Galaxy, which may be dominant compared to the scattering on non self-generated turbulence. Moreover, since self-generated Alfvén waves move in the direction of the decreasing CR density, they lead to CR convection at Alfvén speed. It has been shown by Blasi et al. (2012) and by Aloisio & Blasi (2013) that self-generation may if fact account for the CR spectrum below ~ 200 GeV. Notice that in the presence of self-generated turbulence, the CR diffusion coefficient is no more a fitting parameter, but derives self-consistently from the CR propagation model. The considerations on the effects of convection and diffusion on the CR spectral slope (derived in Sec. 1.1.1) are still applicable, however in this case the momentum scaling of the diffusion coefficient and the transition energy between advection and diffusion dominated regimes, depend in a complicated manner from the CR source distribution and CR distribution function. For instance, a decrease in the CR source density in the presence of self-generation leads to a smaller CR density compared to the case of pre-assigned diffusion coefficient. In fact, in the presence of self-generation, a decrease in the CR density leads to a smaller production of waves, i.e to a larger diffusion coefficient and a faster escape of CRs, which in turns decreases even more the CR density. Similarly, an increase in the advection velocity leads to a decrease of the CR density, i.e to a larger diffusion coefficient. In this case, despite the larger advection velocity, the transition energy between advection and diffusion dominated regimes may not change or even become smaller. Thus, streaming instability constitutes a mechanism of self-regulation of the CR transport.

In addition to the effects on the CR diffusion, an efficient CR generation of Alfvén waves would lead to a strong coupling between the CRs and the ISM, allowing for an effective transfer of energy and momentum between them. This means that CRs exert a force on the ISM directed away from the Galactic disk. If this force is larger than the gravitational pull, a Galactic wind may take place. In such scenario the CR force on the background plasma is expected to act all along the halo and to have an important impact on the gas dynamic and magnetic field configuration. The dynamics of CR-

driven winds, including the CR transport in the presence of self-generated turbulence, is intrinsically non-linear. In fact, the gradient in the CR density determines the wind properties (velocity, pressure, magnetic field) and the excitation of the plasma waves which cause the CR scattering, hence affecting the CR diffusive properties. On the other hand, Galactic winds could have a sizable effect on the CR distribution function, by advecting them out of the Galaxy, by influencing their spectral features, by affecting their radial distribution in the Galactic disk but also, possibly, by reaccelerating them at the wind termination shock.

The size of the diffusive halo in the presence of Galactic winds

An important aspect of the Galactic wind scenario is that the size of the CR propagation region is no more preassigned. Instead, it is determined self-consistently with the CR propagation properties and becomes a function of the particle momentum. This is due to the fact that in the presence of Galactic winds, the CR advection velocity $U(z)$ increases with the distance from the Galactic disk and eventually CR advection starts to dominate over diffusion. This happens at the critical distance $s^*(p)$ for which the advection and diffusion time scales are equal:

$$\frac{s^{*2}(p)}{D(s^*,p)} = \frac{s^*(p)}{U(s^*)}. \tag{1.24}$$

Interestingly, since the diffusion coefficient increases with momentum, $s^*(p)$ also increases with momentum. The quantity $s^*(p)$ roughly sets the halo size at a given particle momentum p and the larger the CR energy, the larger the propagation volume. This fact may have important consequences both on the CR spectrum and anisotropy.

1.1.3 The role of ion-neutral damping

An important issue which arises when considering the CR diffusive transport in the ISM is that Alfvén waves propagating in a partially ionized medium are damped due to ion-neutral damping (see e.g Kulsrud & Cesarsky (1971); Ferriere et al. (1988); Everett & Zweibel (2011)). The damping process is very fast. For instance the expected damping time-scale is of few tens of years for waves resonant with CRs of momentum $\lesssim 75$ GeV/c and for the typical parameters of the ISM. This means that the bulk of CRs in the Galaxy should diffuse very little and should mostly stream freely. This is at odds with the observed residence time of CRs in the Galaxy. A possible explanation may be that, while the near-disk region (0.5-1 kpc above and below the Galactic disk) is plagued by severe ion-neutral damping, farther away from the Galactic disk, in the outer halo, the neutral component is negligible and the CR scattering can be efficient. In such scenario, the actual diffusion

region would be the outer halo. However, we may also speculate that the neutral component is spatially separated from the ionized component and mostly clumped in molecular clouds, so that most of the Galactic volume is filled with ionized gas and the CR scattering may be efficient even in the near-disk region (see Ferrière (2001) for a review of the various gas phases of the ISM).
Those scenarios are applicable also in the presence of CR-driven winds: since such winds can take place only in regions of strong CR-ISM coupling, in the first case the wind launching is expected to be possible only in the the outer halo, while in the second case it may take place also near the Galactic disk. Notice that the first scenario also poses the important question of what the CR transport in the near-disk region may be. In fact, despite the effect of ion-neutral damping, we could speculate that some type of turbulence, probably due to SNe themselves, may still be maintained in the near-disk region. In general, the conditions in this region determine the connection between the CR sources in the disk and the actual diffusion region and may have an important impact on the overall CR transport.

1.2 Galactic winds in galaxies

Large-scale galactic outflows constitute an important feedback process in the ecology and evolution of galaxies. In fact, since they remove gas from the galaxies and inject it into the intergalactic space, they limit the star formation rate. Galactic models that do not include such feedback processes tend to overpredict the amount of baryons and the star formation rate of galaxies (see e.g. Crain et al. (2007)). Moreover, galactic winds pollute the galactic halos and the intergalactic space with hot plasma and metals. This affects the properties of the ISM and IGM, such as the chemical composition, the temperature, the degree of ionization and cooling rate (see e.g Dalgarno & McCray (1972); Miller & Bregman (2015)). In addition, the material injected by galactic winds in the IGM may represent an important contribution to the number of baryons in the Universe (see e.g. Kalberla & Dedes (2008); Miller & Bregman (2015)) and may contribute to solve the problem of missing baryons in the local Universe (see e.g Anderson & Bregman (2010)).
Galactic winds are ubiquitous in most galaxies with a high star-formation rate and/or with active galactic nuclei, both in the local Universe and at high redshift. They can expel several $M_{\odot}$ per year at a speed which can reach a sizable fraction of the speed of light (see e.g Veilleux et al. (2005); King & Pounds (2015)). They have been directly observed in many galaxies through their continuous and line emissions, which range from radio to X-rays depending on the chemical composition and temperature of the ejected gas and dust, and through absorption lines (see Veilleux et al. (2005); Martin et al. (2012)). In many other galaxies winds have not been directly observed,

but hot halos likely generated by the galactic winds themselves have been detected.
Despite their importance, the physics of galactic winds is still not completely understood and several production mechanisms have been proposed (see Veilleux et al. (2005) for a review). Winds may be thermally-driven, i.e generated by the heating of the ISM due to SN explosions (see e.g Chevalier & Clegg (1985)) or by accretion onto the super-massive black holes in the center of AGN (see e.g King & Pounds (2015)); radiation pressure-driven, namely generated by continuum absorption and scattering of starlight radiation on gas and dust grains (see e.g Scoville (2003); Murray et al. (2005)); CR-driven, namely due to the pressure exerted by escaping CRs on the ISM (see e.g Uhlig et al. (2012)). The first two mechanisms are likely to take place in starburst galaxies and galaxies with active nuclei.

1.3 Cosmic Ray-driven winds in the Milky Way

As for the Milky Way, observations have not yet provided clear evidence of the existence Galactic winds. However, hot dilute gas, possibly connected with such winds, has been detected through the continuous emission in the X-ray band (Breitschwerdt & Schmutzler (1994); Breitschwerdt & Schmutzler (1999); Everett et al. (2008)) and through the absorption lines (Oxygen O_{VII} and O_{VIII} lines) in the spectrum of distant Quasars (Miller & Bregman (2015)). Form the Oxygen absorption lines it has been estimated a halo mass of $\sim 10^{10}$ $M_{\odot}$, a halo extension of ~ 100 kpc, a halo temperature of $\sim 10^6 - 10^7$ K and a metallicity of $Z \sim 0.2 - 0.3$. The latter implies that such gas comes from the Galaxy and not from the intergalactic space (Miller & Bregman (2015)).
Moreover, the recent observation of the so called Fermi Bubbles may be associated to recent bursts near the Galactic Center region (see Cheng et al. (2011); Zubovas et al. (2011)) or to past starburst activities (see Lacki (2014)).
In the Milky Way the thermal and radiation pressure gradients are expected to be too small (except maybe for the Galactic Center region) to drive outflows. However, CRs escaping from the Galaxy may provide the force necessary to launch winds. As we pointed out in Sec. 1.1, the fact that the CR energy density is comparable to the thermal and magnetic energy densities and that CRs are observed to be well coupled to the ISM, makes CR-driving an appealing mechanism for wind formation in our Galaxy. This point has been addressed for the first time by Ipavich (1975), which made an attempt to account for the CR contribution to Galactic winds. The author presented a simplified, spherically symmetric Galactic wind model in which he included the CR pressure in the wind hydrodynamics but without taking into account the Dark Matter (DM) halo gravitational potential. He showed that, in or-

der for a Galactic wind to be launched solely due to thermal gradients, high (order of $\sim 10^8 - 10^9$K) temperature for the gas is required, which is not observed in the Galaxy. However, the addition of the CR contribution (due to the fact that the CR pressure acts up to much larger heights from the disk compared to the thermal pressure) makes possible to launch wind without restricting requirement on the gas temperature or on the other physical quantities involved in the calculation (gas density, CR pressure and the mass of the Galaxy).
Later Breitschwerdt et al. (1991) presented an extensive study of the hydrodynamics of CR-driven winds. They considered a realistic geometry in which the wind is assumed to be launched at some distance ($\sim$ 1kpc) from the Galactic disk and the flow proceeds with nearly cylindrical symmetry up to $\sim$ 15 kpc and then opens up spherically. In addition, they included in the wind dynamics the Alfvén waves, generated by CR streaming, and took into account the DM halo gravitational potential. They showed that, with the contribution of CRs and Alfvén waves, Galactic winds can be launched for a large range of input parameters. Finally, they also discussed the important role of wave damping.
The paper by Breitschwerdt et al. (1991) represented a milestone in the sphere of CR-driven winds and their approach was adopted in much of the later work on the subject, including the recent paper by Everett et al. (2008), which used a CR-driven wind model (including damping of Alfvén waves) to explain the observed Galactic soft X-ray emission. The role of CRs in driving winds has been confirmed by later work, in time-dependent calculations (Dorfi & Breitschwerdt (2012)), in hydrodynamical simulations (see Uhlig et al. (2012); Booth et al. (2013); Salem & Bryan (2014)) and in MHD simulations (see Girichidis et al. (2016); Ruszkowski et al. (2016)).
Finally, the important physical and mathematical issue of what happens in the region between the disk and the wind base (see also Sec. 1.1.3) has been addressed in Breitschwerdt et al. (1993), while the effect of the Galactic rotation has been studied in Zirakashvili et al. (1996).

In all these works, no matter the level of refinement, only the hydrodynamic wind problem was addressed, while no information was retained on the CR spectrum. On the other hand, the CR spectrum represents the main observable we can use in order to constraint wind models, hence its prediction is essential. The first, and, to our knowledge, the only attempt to account for both CR-driven winds and their effects of the CR transport was made by Ptuskin et al. (1997). They adopted a simplified approach in which the wind velocity was extrapolated from the hydrodynamic calculation of Zirakashvili et al. (1996) and approximated with a linear function of the heights above the disk to infer some general implications for the spectrum of CRs and for the halo size (see also Sec. 1.1.2). Nevertheless, as we will show in Chapter 4, this approach is too simplified and it is unable to predict

the CR spectrum with accuracy.

1.4 Overview of the thesis work

In this thesis we present the first semi-analytical method to solve self consistently the hydrodynamic problem of the generation of CR-driven Galactic winds and the kinetic problem of the transport of CRs in such winds and in the self-generated turbulence. In our approach neither the CR diffusion properties nor the wind velocity are preassigned. Instead, they are an output of the calculation, together with the CR distribution function. In addition both the CR diffusion coefficient and advection velocity are determined by the CRs themselves. In fact, the CR streaming instability, locally balanced by non-linear Landau damping (NLLD), sets the Alfvén wave spectrum, which in turn determines the CR diffusion coefficient. On the other hand, the CR and wave pressures, together with the thermal pressure, determine the wind and Alfvén speeds, namely the CR advection velocity.
The solution of the wind problem allows for an extensive investigation of the properties and implications of CR-driven Galactic winds:

1) the wind launching depends on the properties of the ISM (gas density and temperature, Galactic magnetic field), on the CR pressure and on the Galactic gravitational potential. All these quantities depend on the position in the Galaxy and are constrained by observations. We studied how the possible presence and properties of Galactic winds, launched at the Sun position, are affected when changing the input parameters within the range allowed by observations. In particular, we considered several Dark Matter models and showed that the effect on the wind properties is quite important.

2) In our theoretical framework, the CR spectrum results from the complex interplay between diffusion and advection on self-generated turbulence and advection with the CR-driven wind. We investigated how the CR spectrum is modified by the presence of a self-generated wind, with a special emphasis on the comparison with the CR spectrum observed at the Earth. In particular, we found that in many cases, input parameters compatible with observations lead to a spectrum that is quite different from the observed one. However, it was still possible to find specific cases in which there is a good agreement with the observed spectrum and the wind characteristics are compatible with the Galactic halo properties deduced from the recent observations of Oxygen emission and absorption lines from the ISM (see Miller & Bregman (2015)).

3) Recent results obtained by analizing Fermi-LAT data (see Acero et al. (2016); Yang et al. (2016)) show a substantial variation of the CR density

as a function of the distance from the Galactic Center, also accompanied by a gradual spectral softening while moving outward from the center of the Galaxy. These findings are difficult to explain in the context of standard models of CR propagation, where the diffusion coefficient is assumed to be constant in the whole Galactic volume. Hence we studied the radial dependence of the CR spectrum in the framework of our non-linear propagation model, both with and without the inclusion of Galactic winds. In the model without winds we find that, for a realistic distribution of CR sources and for reasonable assumptions on the spatial dependence of the magnetic field on the Galactocentric distance, both the observed spatial profile of the CR density and the spectral behavior are well reproduced, in particular those reported in (Acero et al. (2016)). With inclusion of winds, we find that in the outer Galactic ring (Galactocentric distance $\gtrsim$ 10 kpc) the wind is not launched, so that our wind model cannot explain the CR gradient in the outer Galaxy, while it is well explained in the model without winds. In the inner Galaxy (Galactocentric distance $\lesssim$ 10 kpc), the possibility to launch winds and the wind properties strongly depend on the Dark Matter halo model. In this region, the CR density and the spectral behavior reported in (Yang et al. (2016)) are reproduced quite well, while the agreement with (Acero et al. (2016)) is poorer.

The thesis is organized as follows: in Chapter 2 we illustrate the mathematical and technical details of the solution method for the CR-driven wind model. In Chapter 3 we present our results on the dependence of the wind properties on the input parameters. In Chapter 4 we analyze the CR spectral characteristics in a CR-driven wind, also making a comparison with the observed CR spectrum. Finally, in Chapter 5 we study the radial distribution of Galactic CRs in view of the recent analysis of *Fermi*-LAT data. Our conclusions are reported in Chapter Conclusions.

Chapter 2

A semi-analitical approach to Cosmic Ray-driven winds

In this thesis we study the problem of CR-driven Galactic winds, namely the possible generation of winds in the Galaxy as due to the combined action of thermal and CR pressure gradients between the Galactic disk and the halo and the resulting diffusive-convective transport of CRs. Such study requires to solve at the same time two different problems, namely the hydrodynamics of the wind and the CR transport in such wind. The hydrodynamic problem can be summarized as follows: we assume that the wind is launched at a specific point in the Galaxy (the wind base) and that the input quantities for our problem (density and temperature of the background plasma, Galactic magnetic field and gravitational potential, CR pressure) are know at the wind base. The evolution of the wind properties, namely of the gas velocity, density and pressure, of the magnetic field ad of the CR pressure, is governed by the mass, momentum, energy conservation equations and by the equation of state for the gas, by the equation for the flow geometry and by the equation for the CR gas. Given the input parameters at the wind base, we look for a wind solution, namely a stationary solution of the hydrodynamic equations in which the gas is smoothly accelerated from subsonic to supersonic speed while moving out of the Galaxy.
Current models of Galactic CR propagation describe the CR transport as a diffusion-convection process in which diffusion is due to scattering on plasma waves and convection is due to some large scale motion of the ISM or to the scattering waves themselves. In Sec. 1.1.1 we analyzed the CR transport equation in the assumption that both the CR diffusion coefficient and advection velocity are preassigned and do not depend on the location in the Galaxy. Here we assume that the CR diffusion coefficient is due to Alfvén waves generated by CR streaming instability, saturated through non linear Landau damping, and that the CR advection is due to the self-generated waves and to the wind. The CR density gradient between the Galactic disk

(where the CR sources are located) and the halo plays a major role in determining the CR transport properties, since it is responsible for the generation of the plasma waves that cause their scattering and helps in driving the Galactic wind, which in turn affect the CR advective transport. For this reason, the hydrodynamic wind equations and the CR transport equation are coupled to each other in a non-linear way.

2.1 The mathematical model

Here we present the first semi-analytical method to solve the CR-driven wind problem, namely to determine self-consistently both the properties of the wind and the related CR distribution function and diffusion coefficient (see Recchia et al. (2016a)).
We do so in the simplifying assumption that the wind flow and the CR transport are one-dimensional and only occur along the magnetic field lines (parallel geometry). In a full treatment of the wind problem, the magnetic field geometry, and thus the flow geometry, should be determined self-consistently with the wind properties and with the CR distribution function. However this is beyond the scope of the present work and, following most of the literature on CR-driven winds, we assume a preassigned topology for the wind flow.
The dynamics of a CR-driven wind in the stationary regime is described by the system of hydrodynamic equations for the wind (i.e the equations of mass, momentum and energy conservation) and of kinetic transport equation for CRs. Those equations are coupled to each other in different ways: 1) the CR pressure gradient exerts a force which helps the launching of the wind and contribute to determine the wind velocity and, since the wind profile is connected to the gas density profile, also the Alfvén speed. Both velocities affect the advective transport of CRs. 2) CRs generate Alfvén waves through streaming instability, which are quickly damped through NLLD and contribute to the heating of the gas. 3) The equilibrium spectrum of Alfvén waves, derived from the balance of their generation and damping mechanisms, determine the diffusion properties of CRs, which in turn affect the CR gradient and, consequently, the wind properties. These considerations highlight the non-linear nature of the CR-driven wind problem.

2.1.1 The flow geometry

We adopt a flow geometry similar to that introduced by Breitschwerdt et al. (1991) (sketched in Fig. 2.1), and used in much of the subsequent literature on CR-driven winds: we assume that the wind is launched from a surface at distance z_0 above (and below) the Galactic disc, and that it retains a roughly cylindrical geometry out to a characteristic distance Z_b. At larger distances the flow opens up as $\sim z^\alpha$. The wind area transverse to z is then assumed

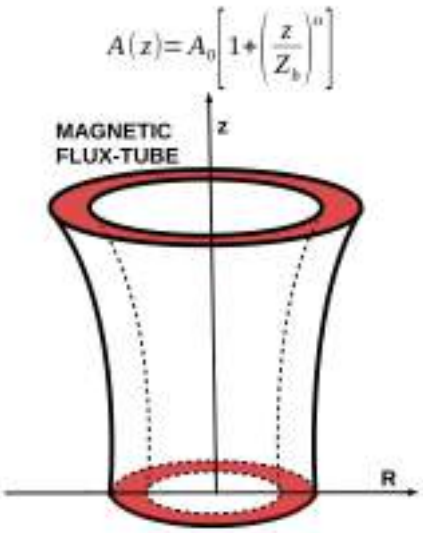

Figure 2.1: Flux-tube topology for the magnetic field lines: z is the distance from the Galactic disk, R is the Galactocentric distance. The flow geometry is roughly cylindrical up to $z \sim Z_b$. At larger distances from the Galactic disk the flow area opens up as $\sim z^{\alpha}$.

to be in the form:

$$A(z) = A_0 \left[1 + \left(\frac{z}{Z_b}\right)^{\alpha}\right], \tag{2.1}$$

which is only function of the spatial coordinate z, namely of the distance from the Galactic disk. Notice that in Breitschwerdt et al. (1991) the authors assumed $Z_b \sim 15$ kpc and $\alpha = 2$, which corresponds to spherical opening. Here, instead, we explore the effect of changing these two parameters for the wind properties (see Sec. 3.3.2).

2.1.2 Wind hydrodynamics

The hydrodynamic equations for the wind read (see Appendix A for their derivation):

$$\vec{\nabla} \cdot (\rho \vec{u}) = 0, \tag{2.2}$$

$$\rho(\vec{u} \cdot \vec{\nabla})\vec{u} = -\vec{\nabla}(P_g + P_c) - \rho\vec{\nabla}\Phi, \tag{2.3}$$

$$\vec{u} \cdot \vec{\nabla} P_g = \frac{\gamma_g P_g}{\rho} \vec{u} \cdot \vec{\nabla}\rho - (\gamma_g - 1)\vec{v_A} \cdot \vec{\nabla} P_c, \tag{2.4}$$

$$\vec{\nabla} \cdot \left[\rho\vec{u}\left(\frac{u^2}{2} + \frac{\gamma_g}{\gamma_g - 1}\frac{P_g}{\rho} + \Phi\right)\right] = -(\vec{u} + \vec{v}_A) \cdot \vec{\nabla} P_c, \tag{2.5}$$

$$\vec{\nabla} \cdot \left[(\vec{u} + \vec{v}_A)\frac{\gamma_c P_c}{\gamma_c - 1} - \frac{\overline{D}\vec{\nabla} P_c}{\gamma_c - 1}\right] = (\vec{u} + \vec{v}_A) \cdot \vec{\nabla} P_c, \tag{2.6}$$

$$\vec{\nabla} \cdot \vec{B} = 0, \tag{2.7}$$

where $\rho(\vec{r})$, $\vec{u}(\vec{r})$ and $P_g(\vec{r})$ are the gas density, velocity and pressure, $\vec{B}$ is the background magnetic field (which has a preassigned geometry, as explained above), while $P_c(\vec{r})$ is the CR pressure and $\gamma_c(\vec{r})$ is the adiabatic index of the CR gas. The average CR diffusion coefficient $\overline{D}$ is defined in Eq. 2.16. Notice that $\gamma_c(\vec{r})$ is actually calculated locally (as a function of $\vec{r}$) from the distribution function $f(p, \vec{r})$ that solves the CR transport equation. $\vec{v}_A(\vec{r}) = \vec{B}/\sqrt{4\pi\rho(\vec{r})}$ is the Alfvén velocity, while $\Phi(\vec{r})$ is the gravitational potential of the Galaxy (see Sec. 3.1 for details).
We assumed that the damping of Alfvén waves occurs on time scales much shorter than any other process involved in the wind and CR dynamics, definitely justified for NLLD (see e.g the related discussion in Everett et al. (2008)). This results in small wave pressure compared to the gas and CR pressures.

When we adopt the flow geometry of Fig. 2.1, the problem becomes effectively one-dimensional and all quantities only depend on the distance from the Galactic disk, z. This simplifies the hydrodynamic equations, which

become (see Appendix B):

$$\rho u A = \text{const}, \tag{2.8}$$

$$AB = \text{const}, \tag{2.9}$$

$$\frac{du}{dz} = u\frac{c_*^2 \frac{1}{A}\frac{dA}{dz} - \frac{d\Phi}{dz}}{u^2 - c_*^2}, \tag{2.10}$$

$$\frac{dP_g}{dz} = \gamma_g \frac{P_g}{\rho}\frac{d\rho}{dz} - (\gamma_g - 1)\frac{v_A}{u}\frac{dP_c}{dz} \tag{2.11}$$

$$\frac{dP_c}{dz} = \gamma_{eff}\frac{P_c}{\rho}\frac{2u + v_A}{2(u + v_A)}\frac{d\rho}{dz}, \tag{2.12}$$

$$c_*^2 = \gamma_g \frac{P_g}{\rho} + \gamma_{eff}\frac{P_c}{\rho}\left[1 - (\gamma_g - 1)\frac{v_A}{u}\right]\frac{2u + v_A}{2(u + v_A)}, \tag{2.13}$$

$$\frac{\gamma_{eff}}{\gamma_{eff} - 1} = \frac{\gamma_c}{\gamma_c - 1} - \frac{\overline{D}}{(\gamma_c - 1)(u + v_A)P_c}\frac{dP_c}{dz}. \tag{2.14}$$

Two important quantities appear in these equations: the generalized sound speed c_* and the the effective adiabatic index for CRs, γ_{eff}. Looking at the definition of c_*^2, Eq. 2.13, one can recognize the sum of the sound speed ($\gamma_g P_g/\rho$) and of a "CR sound speed" (notice the factor $\gamma_{eff}P_c/\rho$, which is formally identical to the sound speed). The CR sound speed also depends on the Alfvénic Mach number u/v_A. Notice that the term $-(\gamma_g - 1)v_A/u$ is due to the non adiabatic gas heating induced by wave damping in Eq. 2.11. The importance of c_* resides in the fact that $u = c_*$ is the condition for the flow to become sonic but also is a critical point for the wind equation 2.10. The effective adiabatic index for CRs, γ_{eff}, takes into account the CR diffusivity in the hydrodynamic equations (see also Zirakashvili et al. (1996)). Note that, as for the CR adiabatic index γ_c, the effective adiabatic index γ_{eff} can be calculated as a function of z from the distribution function $f(p, z)$ and diffusion coefficient $D(z, p)$ that solve the wind problem. However, as it has been verified in all cases treated so far, γ_{eff} shows a weak dependence on z and we can safely treat it as a constant (more on that in the note below). Also Breitschwerdt et al. (1991) introduced the generalized sound speed c_* but with two important differences compared to our calculation. First, they neglected the CR diffusion by assuming that $\overline{D} = 0$. For this reason, in their calculation γ_c appears instead of γ_{eff} (notice that, from Eq. 2.14, if $\overline{D} = 0$ $\gamma_{eff} = \gamma_c$). However, we checked that this assumption on $\overline{D}$ is not justified in general, so that it is necessary to take the CR diffusivity into account in order to achieve the correct solution of the problem. Second, they did not take wave damping into account and retained the wave pressure in the hydrodynamic equations. Without damping, the growth of waves due to CR streaming can in fact lead to a wave pressure which is comparable with the CR pressure. For these reasons, instead of having the term $-(\gamma_g - 1)v_A/u$ in the definition of c_*^2, they have a "wave sound speed" term which takes into

account the effect of the wave pressure.

2.1.3 Cosmic-ray transport equation

The transport of CR protons is described by the advection-diffusion equation (see also Sec. 1.1.1):

$$\vec{\nabla} \cdot \left[D \vec{\nabla} f \right] - (\vec{u} + \vec{v}_A) \cdot \vec{\nabla} f + \vec{\nabla} \cdot (\vec{u} + \vec{v}_A) \frac{1}{3} \frac{\partial f}{\partial \ln p} + Q = 0, \tag{2.15}$$

where $f(\vec{r}, p)$ and $D(\vec{r}, p)$ are the CR distribution function and diffusion coefficient as functions of position $\vec{r}$ and momentum p. The term Q represents the injection of CRs in the Galaxy, which we assume to be limited to the Galactic disc. The average diffusion coefficient of Eq. 2.6 is defined as:

$$\overline{D}(\vec{r}) = \frac{\int_0^\infty dp \; p^2 T(p) D(\vec{r}, p) \nabla f}{\int_0^\infty dp \; p^2 T(p) \nabla f}, \tag{2.16}$$

where $T(p)$ is the kinetic energy of particles with momentum p. The transport equation of CRs becomes one-dimensional with the flux geometry assumed above:

$$\frac{\partial}{\partial z} \left[A \, D \frac{\partial f}{\partial z} \right] - A \, U \frac{\partial f}{\partial z} + \frac{d(A \, U)}{dz} \frac{1}{3} \frac{\partial f}{\partial \ln p} + A \, Q = 0, \tag{2.17}$$

where we introduced the advection velocity $U(z) = u(z) + v_A(z)$. Here we assume that the diffusion coefficient $D(z, p)$ is determined by the local balance between the CR-driven growth of Alfvén waves and their damping through NLLD. Since the self-generated perturbations in the magnetic field are relatively weak, one can use the quasi-linear theory to write the diffusion coefficient as:

$$D(z, p) = \frac{1}{3} \frac{v(p) r_L(z, p)}{\mathcal{F}(z, k_{res})} \bigg|_{k_{\rm res} = 1/r_L}, \tag{2.18}$$

where $\mathcal{F}$ is the normalized energy density per unit logarithmic wavenumber k, calculated at the resonant wavenumber $k_{\rm res} = 1/r_L(p)$. In the regions where the background gas is totally ionized, waves are damped through NLLD at a rate (see Zhou & Matthaeus (1990); Ptuskin & Zirakashvili (2003)):

$$\Gamma_{\rm D} = (2 c_k)^{-3/2} k v_A \mathcal{F}^{1/2}, \tag{2.19}$$

where $c_k = 3.6$. On the other hand the CR-driven growth occurs at a rate which is given by Skilling (1971):

$$\Gamma_{\rm CR} = \frac{16 \pi^2}{3} \frac{v_A}{\mathcal{F} B^2} \left[p^4 v(p) \left| \frac{\partial f}{\partial z} \right| \right]_{p = p_{res}}. \tag{2.20}$$

Equating the two rates, $\Gamma_{\rm D} = \Gamma_{\rm CR}$, and using Eq. 2.18 one obtains:

$$\mathcal{F}(z,p) = 2c_k \left[\frac{p^4 v(p) \left| \frac{\partial f}{\partial z} \right| \frac{16\pi^2}{3} r_L(z,p)}{B^2(z)} \right]^{2/3} , \tag{2.21}$$

where $\mathcal{F}$ is expressed as a function of momentum by means of the resonant condition $p = p_{res}(k)$.

2.1.4 The iterative method

In what follows we illustrate the iterative procedure used to compute the solution of the coupled system of the hydrodynamic equations and of the CR transport equation.
We start the calculation by solving the hydrodynamic equations as described in Sec. 2.2, assuming that all quantities at the wind base z_0 are given (except the wind launching velocity u_0, which is an output of the computation) and setting $\gamma_{eff} = 4/3$ (i.e equal to the adiabatic index of ultrarelativistic gas). This first step allows to derive a guess on the wind properties, i.e the launching velocity u_0, the gas density and pressure, the CR pressure. The Alfvén speed $v_A(z) = B(z)/\sqrt{4\pi\rho(z)}$ is also computed from those outputs. The CR transport Eq. 2.17 is thus solved, as explained in Sec. 2.3, given the CR injection term and using as an input the wind velocity $u(z)$ and the Alfvén speed derived from the hydrodynamic iteration. The solution of Eq. 2.17 gives the spectrum of CRs as a function of height z and momentum p, $f(z,p)$, and the self-generated diffusion coefficient $D(z,p)$. Notice that, in general, the CR pressure obtained by integrating the distribution function $f(z,p)$ is different, also at the wind base, from the one corresponding to the wind and Alfvén speeds derived from the hydrodynamic equations. For this reason other iterations are needed: the updated CR pressure at the wind base is used, together with the updated γ_{eff} (which is calculated from the CR distribution function and diffusion coefficient), to compute the structure of the wind and the whole calculation is repeated. We recall that the effective adiabatic index γ_{eff} takes into account the fact that $\overline{D}$ cannot in general be ignored, in contrast to what has been assumed by Breitschwerdt et al. (1991). This iterative scheme is repeated until the CR spectrum and diffusion coefficient reach convergence at all distances and at all momenta, as well as the whole structure of the wind. In particular, convergence is achieved when the CR pressure calculated from the wind structure matches at all distances the CR pressures computed by integrating the CR distribution function.
Notice that, as we will see in Chapter 4, if we want to apply this procedure to winds launched at the Sun position, we have also to take into account the observed CR pressure and spectrum. In this case, the CR injection is varied, from one iteration to the other, so as to achieve a solution where either the CR pressure at the wind base is the same as observed, or the

value of the CR spectrum at one specific energy (for instance 50 GeV) is the same as observed. It is crucial to stress that neither of these two conditions is sufficient to guarantee that the CR spectrum which is solution of the wind problem is also consistent with the CR spectrum observed at Earth, as we will extensively discuss in Chapter 4.

2.1.5 Note on the CR diffusion term in the hydrodynamic equations

In Recchia et al. (2016a) the diffusion term in the hydrodynamic equations has been treated in a different way, by introducing an effective velocity term,

$$\mathcal{D} = \frac{\frac{d}{dz}\left(A\overline{D}\frac{dP_c}{dz}\right)}{A\frac{dP_c}{dz}}. \tag{2.22}$$

In that case, the equation for the CR pressure (Eq. 2.12) and for the generalized sound speed (Eq. 2.13) become

$$\frac{dP_c}{dz} = \frac{\gamma_c P_c}{\rho}\frac{2u + v_A}{2(u + v_A - \mathcal{D})}\frac{d\rho}{dz} \tag{2.23}$$

$$c_*^2 = \gamma_g \frac{P_g}{\rho} + \gamma_c \frac{P_c}{\rho}\left[1 - (\gamma_g - 1)\frac{v_A}{u}\right]\frac{2u + v_A}{2(u + v_A - \mathcal{D})}. \tag{2.24}$$

It has been checked that both methods, i.e using γ_{eff} or $\mathcal{D}$, lead to the same results. However, using γ_{eff} is easier and cleaner from the numerical point. In fact, the calculation of $\mathcal{D}$ involves the numerical derivative of $\overline{D}\frac{dP_c}{dz}$ (moreover divided by $\frac{dP_c}{dz}$). In addition, as above mentioned, γ_{eff} is a weak function of z, and can be treated as a constant without significantly affecting the result. This allows not only to neglect the derivative of γ_{eff} in Eq. 2.12, but also to use the first integral for the CR pressure, Eq. B.15, which is valid when $\overline{D} = 0$ (see Appendix B).

2.2 Hydrodynamic calculation

In this section we illustrate the method adopted in order to determine the wind profile for a given set of physical conditions at the wind base. Notice that this procedure is embedded in an iterative calculation which, as explained above, is repeated until the solution for a CR-driven wind is achieved, i.e until the convergence of the wind structure and of the CR spectrum and diffusion coefficient is reached and the CR pressure computed from the wind structure matches the one computed from the spectrum.

We look for a wind solution of Eq. 2.8-2.14, namely a solution for the flow velocity $u(z)$ that shows a smooth transition from subsonic ($u < c_*$) to

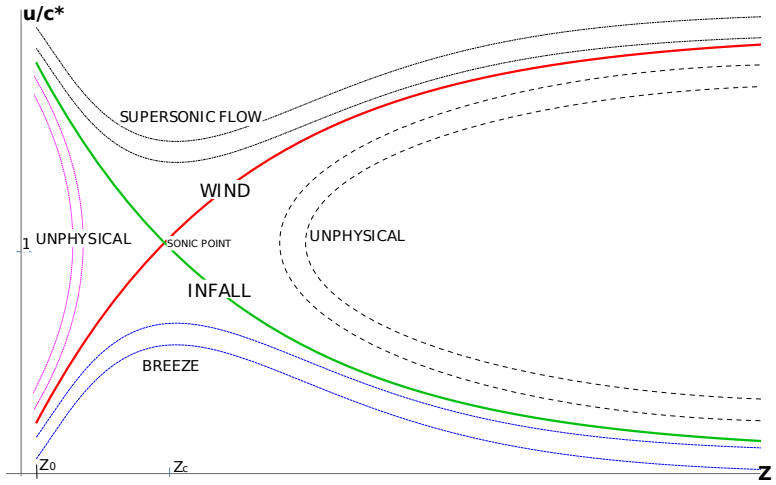

Figure 2.2: Topology of the solutions of the hydrodynamics equations: z_0 indicates the base of the wind, while z_c is the critical point, where $u(z_c) = c_*(z_c)$. The (red) solid line represents a wind solution, that starts as subsonic and becomes supersonic at the critical point. The branches of the solutions that are unphysical are labeled as such.

supersonic ($u > c_*$) motion, where $c_*(z)$ is the compound sound speed as a function of z.

The topology of the solutions (see also Breitschwerdt et al. (1991)) of Eq. 2.8-2.14 depends on the nature of the critical points of the wind equation 2.10, i.e of the points in which the velocity derivative has zero numerator ($c_*^2 = \frac{d\Phi}{dz}/\frac{1}{A}\frac{dA}{dz}$) and/or zero denominator ($u^2 = c_*^2$), and is schematically represented in Fig. 2.2. The point for which both the numerator and the denominator vanish is the critical (sonic) point, and it corresponds to the location where the flow velocity equals the compound sound speed, i.e $u = c_*$. As shown in Fig. 2.2, there are two curves passing through the critical point. The one corresponding to a subsonic flow at z_0 is the one relevant for our problem. The other one corresponds to an accretion (infall) solution. The curves in the lower branch of solutions shown in Fig. 2.2 correspond to flows that remain subsonic, and are called “breezes". The upper branch corresponds to supersonic flow and is physically irrelevant. For both families of curves, there is a point where the numerator of Eq. 2.10 vanishes. The other two branches are unphysical and for both there is a point where the denominator of Eq. 2.10 vanishes.

For given values of the magnetic field B_0, gas density ρ_0, gas pressure P_{g0} and CR pressure P_{c0} at the wind base $z = z_0$, we compute the launching velocity u_0 that corresponds to the wind solution, namely the value of u_0 for which the flow starts as subsonic and then smoothly becomes supersonic at the critical point z_c (see Fig. 2.2). Both the location of the sonic point and

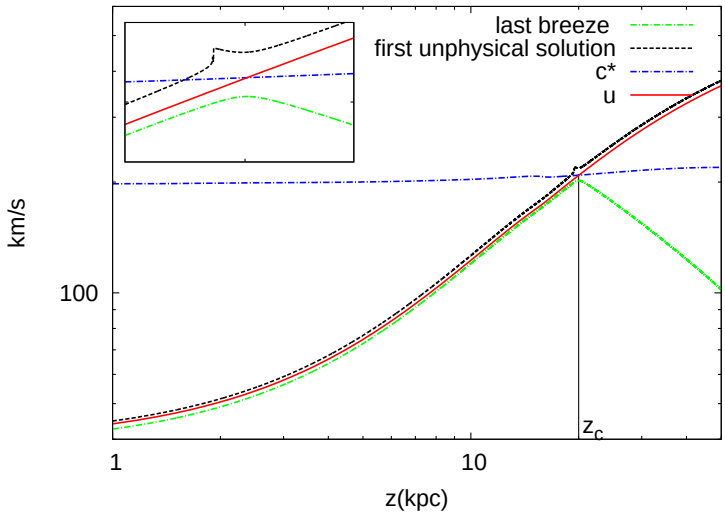

Figure 2.3: Schematic picture of the solution method for the hydrodynamic equations: the wind curve lies between a breeze, obtained by integrating with $u_0 = u_{0B}$, and an unphysical solution, obtained by integrating with $u_0 = u_{0U}$, where $u_{0B} < u_{0U}$. The location of the sonic point z_c can be estimated as the location of the maximum of the breeze. The small box shows a zoomed region around the sonic point.

the launching velocity u_0 are outputs of the calculation. For each iteration, P_{c0} and γ_{eff} in Eq. 2.14 are computed based on the solution of the transport equation in the previous iteration.

From the technical point of view, we start by searching for the wind solution by looking in a closed interval of values for the launching velocity u_0 which may potentially include the actual solution. We do so by imposing three criteria that we know the solution must fulfill: first, the flow is subsonic at the wind base ($c_{*0} > u_0$); second, the wind velocity is a growing function of z at the wind base ($\frac{du}{dz}|_{z_0} > 0$); third, the wind velocity is physical at infinity ($u_f^2 > 0$). This last point derives from imposing energy conservation between the wind base and infinity, i.e (see Appendix B for the derivation)

$$\frac{u^2}{2} + \frac{\gamma_g}{\gamma_g - 1}\frac{P_g}{\rho} + \Phi + \frac{\gamma_{eff}}{\gamma_{eff} - 1}\frac{P_c}{\rho}\frac{u + v_A}{u} = \text{const}, \tag{2.25}$$

and requiring that at spatial infinity all fluxes vanish with the exception of the kinetic flux associated to the wind bulk motion.

Once a closed interval for u_0, say $[u_{0,\min}, u_{0,\max}]$, has been identified, we numerically integrate the hydrodynamic equations starting at z_0 and for values of u_0 in this range, stepped by Δu_0. In this way we sample the topology of the solutions and we can identify the transition between the last

breeze and the first unphysical solution by gradually increasing the value of u_0. This procedure can be repeated to narrow down the region where the actual wind solution is located and return the launching velocity of the wind. In addition, it is also possible to estimate the location of the sonic point as the location of the top of the nearest breeze (with the desired accuracy), as shown in Fig. 2.3.

We can then compute both the flow speed and its derivative at the sonic point:

$$u_c^2 = c_{*c}^2 = \frac{d\Phi}{dz} \Big/ \frac{1}{A}\frac{dA}{dz}, \tag{2.26}$$

$$\left(\frac{du}{dz}\right)_{z_c} = \frac{u_c}{2}\left(\frac{1}{A}\frac{dA}{dz}\right)_{z_c} + \sqrt{\left(-\frac{u_c^2}{4}\left(\frac{1}{A}\frac{dA}{dz}\right)^2 + \frac{u_c^2}{2}\frac{1}{A}\frac{d^2A}{dz^2} - \frac{1}{2}\frac{d^2\Phi}{dz^2}\right)_{z_c}}. \tag{2.27}$$

The last expression has been obtained by Taylor expanding Eq. 2.10 around the critical point. In addition, using the conservation relations, Eq. 2.8, 2.9 and 2.25, and the fact that at the sonic point $u_c = c_*(z_c)$, we can compute the values of all physical quantities (ρ, B, P_g, P_c) at the sonic point. The wind solution is finally found by integrating the hydrodynamic Eqs. 2.8-2.14, starting at the sonic point toward $z = z_0$ and toward $z \to \infty$.

2.3 Kinetic calculation

The stationary CR transport equation is reported in Eq. 2.17. The injection of CRs is assumed to take place only from sources in the Galactic disk (considered as infinitely thin) and can be written as $Q(z,p) = Q_0(p)\delta(z)$. $Q_0(p)$ is the injection spectrum,

$$Q_0(p) = \frac{\mathcal{N}_{SN}(p)\mathcal{R}_{SN}}{\pi R_d^2}, \tag{2.28}$$

where $\mathcal{N}_{SN}(p)$ is the spectrum contributed by an individual source occurring with a rate $\mathcal{R}_{SN}$ and R_d is the Galactic disk. Here we are implicitly assuming that the sources of Galactic CRs are SNRs, although the calculations presented here do not depend crucially on such an assumption. The spectrum of each SNR can be written as:

$$\mathcal{N}_{SN}(p) = \frac{\xi_{CR}E_{SN}}{I(\gamma)c(mc)^4}\left(\frac{p}{mc}\right)^{-\gamma}, \tag{2.29}$$

where ξ_{CR} is the CR injection efficiency (typically $\sim$ 10%), E_{SN} is the energy released by a supernova explosion ($\sim 10^{51}$erg), $\mathcal{R}_{SN}$ is the rate of SN

explosions ($\sim 1/30\,\mathrm{yr}^{-1}$), and $I(\gamma)$ is a normalization factor chosen in such a way that

$$\int_0^\infty \mathcal{N}_{SN} T(p)\, d^3p = \xi_{CR} E_{SN}, \tag{2.30}$$

where $T(p)$ is the kinetic energy of particles with momentum p.

Eq. 2.17 can be recast in a simpler form by noticing that

$$UA\frac{\partial f}{\partial z} = \frac{\partial (AUf)}{\partial z} - f\frac{d(AU)}{dz}, \tag{2.31}$$

so that Eq. 2.17 becomes

$$\frac{\partial}{\partial z}\left[A\,D\frac{\partial f}{\partial z} - U\,A\,f\right] + \frac{d(A\,U)}{dz}\left[f + \frac{p}{3}\frac{\partial f}{\partial p}\right] + A\,Q_0(p)\delta(z) = 0. \tag{2.32}$$

In addition,

$$\frac{1}{3}\frac{1}{p^3}\frac{\partial (f\,p^3)}{\partial \ln p} = \frac{f}{3}\frac{\partial \ln(f\,p^3)}{\partial \ln p} = \frac{1}{3}\frac{\partial f}{\partial \ln p} + f \tag{2.33}$$

so that we can finally rewrite Eq. 2.17 as

$$\frac{\partial}{\partial z}\left[A\,D\frac{\partial f}{\partial z} - U\,A\,f\right] - \frac{d(A\,U)}{dz}\frac{f}{3}q + A\,Q_0(p)\delta(z) = 0, \tag{2.34}$$

where we introduced the slope:

$$q(z,p) \equiv -\frac{\partial \ln(f\,p^3)}{\partial \ln p}. \tag{2.35}$$

We look for an implicit solution of the transport equation 2.34 which satisfies the conditions $f(0,p) = f_0(p)$ at the disk and $f(p,H) = 0$ at some outer boundary H. Note that here H is set just for numerical purposes, and can be also located at spatial infinity. In contrast to what happens in standard CR propagation models, where the size of the halo has to be imposed by hand and plays a crucial role, first of all in guaranteeing that a stationary solution exists, the transport in a CR-driven wind does not require a preassigned halo size (see also the discussion in Sec. 1.1.2). Instead, as it has been anticipated in Sec. 1.1.2 and as it will be pointed out in Sec. 4.1, the halo size in the wind scenario becomes an output of the calculation and depends on the particle momentum. For numerical purposes we usually take H in the range 300-700 kpc.

An implicit equation for $f_0(p)$ can be obtained by integrating Eq. 2.34 around the disk, i.e between $z = 0^-$ and $z = 0^+$, and using the fact that the

problem is symmetric around the disk so that:

$$
\begin{aligned}
U(0^+) &= -U(0^-) = U_0 \\
\left.\frac{dU}{dz}\right|_0 &= 2U_0\delta(z) \\
f(0^+) &= f(0^-) = f_0(p) \\
\left.\frac{dU}{dz}\right|_{0^+} &= -\left.\frac{dU}{dz}\right|_{0^-}.
\end{aligned}
$$

Integration around the disc leads to:

$$
2A_0D_0\left.\frac{df}{dz}\right|_{0^+} - 2A_0U_0\frac{f_0}{3}\tilde{q}_0 + A_0Q_0(p) = 0, \tag{2.36}
$$

where we used Eq. 2.35 and 2.33, and we introduced

$$
\tilde{q}_0(p) \equiv -\frac{\partial \ln f_0(p)}{\partial \ln p}. \tag{2.37}
$$

Integrating Eq. 2.34 between $z = 0^+$ and a generic height z, one gets the equation:

$$
\begin{aligned}
\frac{\partial f}{\partial z}(z,p) = &\frac{U(z)}{D(z,p)}f(z,p) \\
&+ \frac{\mathcal{G}(z,p)}{A(z)D(z,p)} - \frac{A_0Q_0(p)}{2A(z)D(z,p)} - \frac{U_0A_0f_0(p)\bar{q}_0(p)}{A(z)D(z,p)},
\end{aligned} \tag{2.38}
$$

where

$$
\mathcal{G}(z,p) \equiv \int_0^z dz\, \frac{d(AU)}{dz}\frac{f}{3}q \tag{2.39}
$$

$$
\bar{q}_0(p) \equiv 1 - \frac{\tilde{q}_0}{3}. \tag{2.40}
$$

Integration of this equation between z and H with the condition $f(H,p) = 0$ leads to the following implicit solution for $f(z,p)$:

$$
f(z,p) = \int_z^H \frac{dz'}{A(z')D(z',p)} G(z',p) \exp^{-\int_z^{z'} dz'' \frac{U(z'')}{D(z'',p)}}, \tag{2.41}
$$

where

$$
G(z,p) = \frac{A_0Q_0(p)}{2} + A_0U_0f_0(p)\bar{q}_0 - \mathcal{G}(z,p). \tag{2.42}
$$

Notice that this way of handling the CR propagation equation is the same used in Sec. 1.1.1 in case of preassigned and spatially constant diffusion coefficient and advection velocity.

The formal solution 2.41 of the transport equation hides the non-linearity of the problem in the function $G(z,p)$, which depends on $f(z,p)$ and on the CR diffusion coefficient $D(z,p)$ (see Eq. 2.18). The solution of Eq. 2.41 is computed by using an iterative procedure which reaches convergence when, for a given iteration j, the spectrum $f^j(z,p)$ and $f^{j-1}(z,p)$ (as well as the diffusion coefficient $D^j(z,p)$ and $f^j(z,p)$) are close to each other within a desired accuracy. Note that the advection velocity $U(z) = u(z) + v_A(z)$ is computed from the hydrodynamic equations and is fixed while iterating upon the distribution function f^j.

Chapter 3

Dependence of the wind properties on the Galactic environment

In Chapter 2 we described the semi-analytical method used to solve the CR-driven wind problem. As illustrated so far, the method basically consists of two blocks, the hydrodynamic calculation of the wind properties and the kinetic calculation of the CR spectrum (and diffusion coefficient), linked together in an iterative procedure.
The wind launching depends on the properties of the ISM (gas density and temperature, Galactic magnetic field), on the CR pressure, on the flow geometry and on the Galactic gravitational potential. All these quantities depend on the position in the Galaxy and are constrained by observations (see e.g Ferrière (2001); Cox (2005); Wolfire et al. (2003); Miller & Bregman (2015)).
Here we present a purely hydrodynamical analysis of the possible presence and properties of Galactic winds, launched at the Sun position, focusing on how winds are affected when changing the input parameters within the observational ranges. Suitable ranges for the input parameters at the Sun location, as deduced from observations, are reported in Sec. 3.2. In particular, we considered several Dark Matter (DM) models (as described in Sec. 3.1) and showed that the effect on winds is quite important.
As illustrated in Sec. 2.2, the hydrodynamic problem consists, once specified a given set of input parameters, in the determination of the launching velocity u_0 for which the flow experiences a smooth transition from the subsonic to the supersonic regime. Known u_0, both the mass and energy flux of the wind are fixed, and it is possible to compute all the hydrodynamic magnitudes (gas density and pressure, wind velocity and CR pressure) as functions of the distance from the Galactic disk.
The wind properties which we are mainly interested in are the wind launching velocity, the wind terminal velocity and the location of the sonic point

(which gives indication on the wind evolution as a function of the distance from the Galactic disk).

3.1 The Galactic gravitational potential

The mass distribution of the Milky Way and in general of galaxies is principally determined by analyzing the dynamics of stars and gas, namely by studying kinematic data such as rotation velocities, velocity dispersions, and motions of satellite galaxies. Spiral rotation curves provide valuable information on the mass content of our Galaxy and of other spiral galaxies and also reveal the presence of a dark matter (DM) component of yet unknown nature (see e.g Bertone et al. (2005) for a review). The presence of dark matter also affects the dynamics of galaxy clusters and the large-scale structure of the Universe.
Many current models for the mass distribution of the Galaxy include a central bulge, a stellar and gas disk and a DM halo (see e.g Irrgang et al. (2013)). Several mass profiles for galactic dark matter halos have been proposed in order to explain the dynamics of galaxies and the cosmological large-scale structures. One of the most widely used models is the Navarro-Frenk-White mass profile (Navarro et al. (1996)), which was inferred from Cold Dark Matter (CDM) cosmological simulations. On large scales (galaxy clusters and superclusters, cosmological filaments) this model has proven quite successful, while on galactic scales it faces a number of problems. For instance, it predicts the presence of a central cusp in the density profile of galaxies which is not observed in many galaxies, in particular in those with low mass.
A DM density profile that appears to fit quite better the observed galactic rotation curves has been proposed by Burkert (1995). In contrast to the Navarro-Frenk-White profile, the Burkert profile has a central core and does not show a central cusp.

Following Breitschwerdt et al. (1991) and Irrgang et al. (2013), for the gravitational potential of the Galactic bulge and disk we used the model proposed by Miyamoto & Nagai (1975):

$$\Phi_{\mathrm{B,D}}(R_0, z) = -\sum_{i=1}^{2} \frac{GM_i}{\sqrt{R_0^2 + \left(a_i + \sqrt{z^2 + b_i^2}\right)^2}}, \tag{3.1}$$

where z and R_0 are the distance from the Galactic disk and the Galactocentric distance respectively. For the parameters of this model we used the values proposed by Sofue (2012), namely (M_1, a_1, b_1) =(1.652 $\times$ $10^{10} M_\odot$, 0.0 kpc, 0.522 kpc) for the bulge and (M_2, a_2, b_2) =(3.4 $\times$ $10^{10} M_\odot$, 3.19 kpc, 0.289 kpc) for the disk.

For the dark matter mass distribution we considered three models, namely the above mentioned Navarro-Frenk-White and Burkert profiles, and, following previous work on CR-driven winds by Breitschwerdt et al. (1991) and Everett et al. (2008), the Innanen profile (Innanen (1973)):

- Navarro-Frenk-White (NFW) (Navarro et al. (1996)):

  the density profile is of the form

  $$\rho_{\rm NFW} = \frac{\rho_0}{x(1+x)^2}, \tag{3.2}$$

  where $x = r/r_c$ and r_c is the scale radius of the distribution. For the two quantities ρ_0 and r_c we considered both the values given for the Milky Way by Sofue (2012) ($\rho_0 = 1.06 \times 10^7$ M$_\odot$ kpc^{-3}; $r_c = 12.0$ kpc) and by Nesti & Salucci (2013) ($\rho_0 = 1.3 \times 10^7$ M$_\odot$ kpc^{-3}; $r_c = 16.0$ kpc). We refer to the two sets of parameters as NFW-Sofue and NFW-Salucci respectively. The DM halo is assumed to extend out to a maximum distance that equals the virial radius, which corresponds to $r_{\rm vir} \approx 240$ kpc for NFW-Sofue and $r_{\rm vir} \approx 320$ kpc for NFW-Salucci. The gravitational potential corresponding to this spatial distribution reads:

  $$\begin{aligned} \Phi(x) = &- 4\pi G\rho_s r_c^2 \left[\frac{\ln(1+x)}{x} - \frac{\ln(1+x_{\rm vir})}{x_{\rm vir}}\right] - \\ &- \frac{GM_{\rm vir}}{r_c}\frac{1}{x_{\rm vir}} \qquad\qquad (r \le r_{\rm vir}) \end{aligned} \tag{3.3}$$

  $$\Phi(x) = - \frac{GM_{\rm vir}}{r_c}\frac{1}{x}. \qquad\qquad (r > r_{\rm vir}).$$

- Burkert (BUR) (Burkert (1995)):

  the density profile is of the form

  $$\rho_{\rm BUR} = \frac{\rho_0}{(1+x)(1+x^2)}, \tag{3.4}$$

  where $x = r/r_c$ and r_c is the core radius. For the two quantities ρ_0 and r_c we considered the values given for the Milky Way by Nesti & Salucci (2013) ($\rho_0 = 4.13 \times 10^7$ M$_\odot$ kpc^{-3}; $r_c = 9.3$ kpc). The virial radius for this model is $r_{\rm vir} \approx 300$ kpc.
  The gravitational potential corresponding to this spatial distribution

reads:

$$\Phi(x) = -4\pi G\rho_s r_c^2 \left[\frac{1+x}{2x}[\arctan(x) - \ln(1+x)] + \frac{x-1}{4x}\ln(1+x^2) - \right. \tag{3.5}$$
$$\left. \frac{1+x_{vir}}{2x_{vir}}[\arctan(x_{vir}) - \ln(1+x_{vir})] - \frac{x_{vir}-1}{4x_{vir}}\ln(1+x_{vir}^2)\right] - \frac{GM_{\rm vir}}{r_c}\frac{1}{x_{\rm vir}} \qquad (r \leq r_{\rm vir})$$

$$\Phi(x) = -\frac{GM_{\rm vir}}{r_c}\frac{1}{x}. \qquad (r > r_{\rm vir}).$$

- Innanen (INN) (Innanen (1973)):

  the mass profile is of the form

$$M_{\rm INN} = M_0 \frac{x^3}{(1+x)^2}, \tag{3.6}$$

  where $x = r/r_c$. For the two quantities M_0 and r_c we considered the values given for the Milky Way by Breitschwerdt et al. (1991) ($M_0 = 1.35 \times 10^{11}$ M$_\odot$; $r_c = 13.0$ kpc). The virial radius of the model is $r_{\rm vir} \approx 100$ kpc.
  The gravitational potential corresponding to this mass distribution is:

$$\Phi(x) = \frac{GM_0}{r_c}\left[\ln(1+x) + \frac{1}{1+x} - \ln(1+x_{vir}) - \frac{1}{1+x_{vir}}\right] - \tag{3.7}$$
$$- \frac{GM_{\rm vir}}{r_c}\frac{1}{x_{\rm vir}} \qquad (r \leq r_{\rm vir})$$

$$\Phi(x) = -\frac{GM_{\rm vir}}{r_c}\frac{1}{x}. \qquad (r > r_{\rm vir}).$$

These halo models predict a DM density at the Sun position in the range $0.2 - 0.4$ GeV/cm^3, in agreement with most of the current literature (see Salucci et al. (2010) for a discussion on the local DM density).
A plot of the gravitational acceleration as a function of the height z from the disc associated with the Galactic bulge and disk and with the considered DM halos at the position of the Sun ($R_\odot = 8.5$ kpc) is shown in Fig. 3.1(a). One can see that the various DM models show large differences in magnitude below $z \sim 30 - 40$ kpc. Since these profiles predict a similar DM density at the Sun, this is due to the different functional dependence on $x = r/r_c$ and to the different values of the scale radius r_c. The BUR and INN profiles give

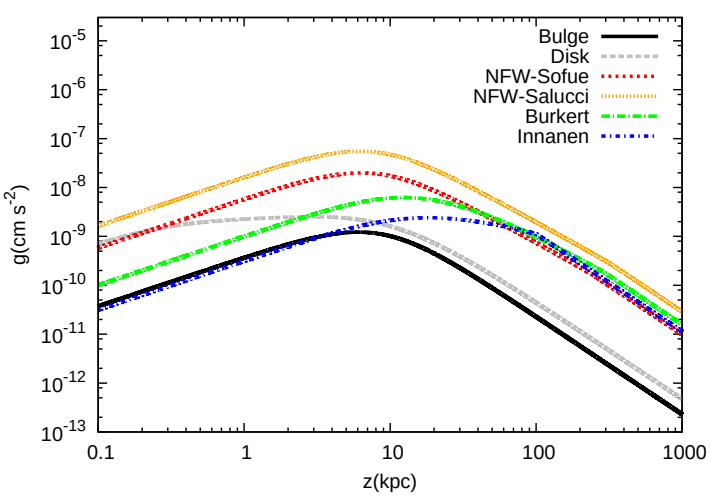

(a) Galactic gravitational acceleration as function of z at $R_\odot$.

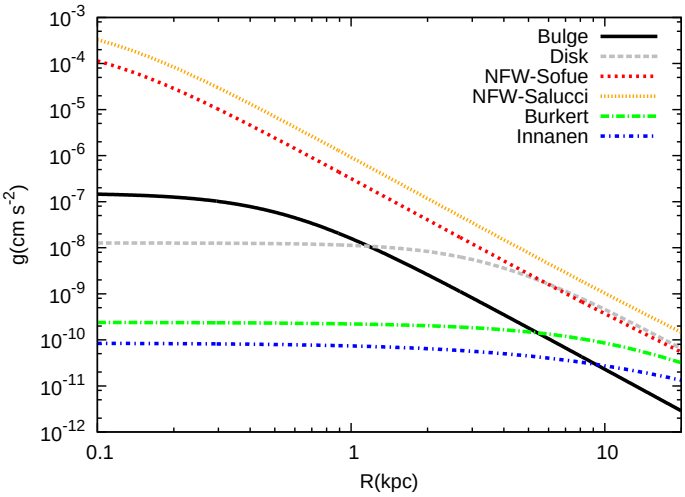

(b) Galactic gravitational acceleration as function of R at $z = 100$ pc.

Figure 3.1: Galactic gravitational acceleration as due to the Galactic bulge and disk, and to different Dark Matter halo models: a) all curves are computed at the Sun position ($R_\odot = 8.5$ kpc) and are functions of the height from the Galactic disk; b) All curves are computed at $z = 100$ pc and are functions of the Galactocentric distance.

a smaller contribution compared to the disk component below $z \lesssim 10$ kpc, while the two NFW models dominate over the bulge and disk components practically at all z.

The gravitational components as functions of the Galactocentric distance R at $z = 100$ pc are shown in Fig. 3.1(b). One can see that the INN and BUR DM profiles are largely dominated by the bulge and disk components up to R $\sim$ 9-10 kpc, and their acceleration is nearly independent on R. The NFW-Salucci profile dominates all other components at all R, while the NFW-Sofue dominates up to $R \sim 5 - 6$ kpc and at larger R becomes comparable with the disk component. Notice also that the acceleration for the NFW model largely increases toward the Galactic center, due to the cuspy density profile.

3.2 Fiducial values for the environmental parameters

The ISM is a rich environment in which several components, distinguished by the level of ionization and temperature, coexist and interact: molecular and atomic neutral gas, warm and hot ionized gas, interstellar magnetic field and CRs. The most abundant element in the ISM is hydrogen followed by

helium, carbon, oxygen, nitrogen etc. The various components are roughly in equilibrium and play an important dynamical role in the Galaxy. In the cooler, dense regions of the ISM, matter is primarily in molecular form and can reach densities as high as 10^6 cm^{-3}. On the other hand, in the diffuse regions of the ISM, matter is mainly ionized and can reach densities as low as 10^{-4} cm^{-3}. In addition, the colder and denser phases of the ISM are mainly confined in the Galactic disk and have filling factor of order $\sim 1-5\%$, much smaller than the dilute hot gas filling factor, which is of order $30-70\%$. A detailed study of the gas components of the ISM has been carried out by several authors (see e.g Cox (2005); Wolfire et al. (2003)) while a comprehensive review of the actual knowledge of the ISM can be found in Ferrière (2001). In Table 3.1 we summarize the main properties of the gas components of the ISM in the vicinity of the Sun as reported in Ferrière (2001).

Table 3.1: Components of the ISM and their properties in the vicinity of the Sun (see Ferrière (2001)).

Component	Temperature (K)	Density (cm^{-3})	Scale Height (kpc)
Molecular	10-20	$10^2 - 10^6$	~ 0.1
Cold Atomic	50-100	20-50	$\sim 0.1 - 0.4$
Warm Atomic	6000-10000	0.2-0.5	$\sim 0.1 - 0.4$
Warm Ionized	8000	0.2-0.5	~ 1
Hot Ionized	$\sim 10^6$	~ 0.006	> 1

The Galactic magnetic field shows a rich structure in which at least a disk component, which follows the spiral arms, and an out of disk component can be found (see Jansson & Farrar (2012)). The regular field strength changes with the Galactocentric distance. While there is a general consensus that in the so-called "molecular ring", between 3 and 5 kpc (see Jansson & Farrar (2012); Stanev (1997)), the magnetic field strength is nearly constant, much less is known about the trend in the Galactic center region and at R $>$ 5 kpc. Jansson & Farrar (2012) and Stanev (1997) suggest the following prescription for the radial dependence of the regular magnetic field strength:

$$\begin{aligned} B_0(R < 5\,\mathrm{kpc}) &= B_\odot R_\odot / 5\,\mathrm{kpc} \\ B_0(R > 5\,\mathrm{kpc}) &= B_\odot R_\odot / R. \end{aligned} \tag{3.8}$$

The regular field strength in the vicinity of the Sun quoted in Jansson & Farrar (2012) is $\sim 1-2\mu$G for the disk component and $\sim 1\mu$G for the out

of disk component. In Ferrière (2001) $B_\odot \sim 1.5\mu$G is reported, while in Cox (2005) the authors suggest a value of $\sim 3-5\,\mu$G (which includes all field components).

To conclude this overview, we mention the recent work by Miller & Bregman (2015), in which the authors analyze the Oxygen O_{VII} and O_{VIII} absorption lines in Quasar spectra and the emission from the ISM and infer the presence of a large Galactic corona, composed by hot dilute gas which reaches height larger than $\sim 50-100$ kpc. For the corona the authors deduce a temperature of 2×10^6K and a density distribution

$$n(r) \approx \frac{n_0 r_c^{3\beta}}{r^{3\beta}}, \tag{3.9}$$

where $r=\sqrt{R^2+z^2}$, $\beta = 0.5\pm0.3$ and $n_0 r_c^{3\beta} = 1.35\pm0.24$ cm^{-3}kpc$^{3\beta}$. Those values correspond to a gas density of $3-6\times10^{-3}$ cm^{-3} in the vicinity of the Sun. Notice that this coronal gas could be in fact the result of a Galactic wind.

All these pieces of information give us the possibility to define reasonable fiducial intervals for the input parameters of our wind problem (see Table 3.2 for a summary): we are interested in the hot dilute phase of the ISM and in the out of disk regular magnetic field, for which we retain a density $3-6\times10^{-3}$ cm^{-3}, a temperature $1-3\times10^6$K and a field strength $1-2\mu$G in the vicinity of the Sun.
The pressure of the proton component of CRs measured at Earth is $\sim 4\times10^{-13}$ erg/cm^{-3}.
Finally, Breitschwerdt et al. (1991) and Everett et al. (2008) assumed that the flux-tube area index (α in Fig. 2.1) equals 2 (spherical opening), while the results of Miller & Bregman (2015) suggest $\alpha\sim1.5$. As for the area length scale (Z_b in Fig. 2.1), in Breitschwerdt et al. (1991) the value 15 kpc was used (which roughly corresponds to the Galactic disk radius) while in Everett et al. (2008) Z_b was treated as a fitting parameter and allowed to vary around ~5 kpc. Here we retain $\alpha\sim1.5-2$ and $Z_b\sim5-15$ kpc.

Table 3.2: Fiducial values for the wind input parameters at the Sun position.

parameter	fiducial range
area-α	1.5-2.0
are-Z_b	5-15 kpc
gas density	$3 - 6 \times 10^{-3}$ cm^{-3}
gas temperature	$1 - 3 \times 10^{6}$K
regular B	$1 - 2\mu$G
CR pressure	4×10^{-13} erg/cm^{-3}

3.3 Parameters study

The hydrodynamic wind equations discussed in Chapter 2, and in particular the mass and energy conservation equations and the wind equation,

$$\rho u A = \text{const} \tag{3.10}$$

$$\frac{u^2}{2} + \frac{\gamma_g}{\gamma_g - 1}\frac{P_g}{\rho} + \Phi + \frac{\gamma_{eff}}{\gamma_{eff} - 1}\frac{P_c}{\rho}\frac{u + v_A}{u} = \text{const} \tag{3.11}$$

$$\frac{du}{dz} = u\frac{c_*^2\, a(z) - g(z)}{u^2 - c_*^2}, \tag{3.12}$$

(referring to Eq. 2.10 we define $a(z) \equiv \frac{1}{A}\frac{dA}{dz}$ and $g(z) \equiv \frac{d\Phi}{dz}$), present many similarities with the Solar wind and the De Laval nozzle problem.
In analogy with the Solar wind, we define a wind ("coronal") base where the boundary conditions for the problem are assigned, and we look for a solution in which the flow experiences a smooth transition from subsonic to supersonic regime, as in the De Laval nozzle problem. As in the Parker model for the Solar wind (see Parker (1965)) the only possible transonic solution is the one which passes through the critical point, as described in Sec. 2.2.
The similarity with the De Laval nozzle is even more evident if we compare the formal expression for the wind equation reported above:

$$\frac{1}{u}\frac{du}{dz} = \frac{a(z) - \frac{g(z)}{c^{*2}}}{M^2 - 1} \quad \text{(Wind equation)} \tag{3.13}$$

$$\tag{3.14}$$

$$\frac{1}{u}\frac{du}{dz} = \frac{\mathfrak{a}(z)}{M^2 - 1} \quad \text{(De Laval nozzle equation)}$$

where $M = u/c^*$ is the Mach number and $\mathfrak{a}(z) \equiv \frac{1}{A}\frac{dA}{dz}$ for the De Laval nozzle. In Fig. 3.3 the scheme of a De Laval nozzle is shown. Notice that the

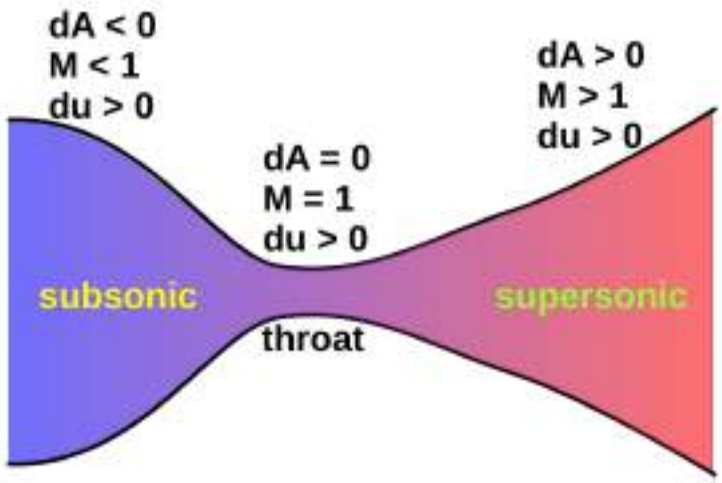

Figure 3.2: Scheme of a De Laval nozzle: the flow is smoothly accelerated (du/dz $>$ 0 in all the duct) from the subsonic (M $<$ 1) to the supersonic regime (M $>$ 1). The flow is subsonic in the converging section (dA/dz $<$ 0), becomes sonic at the throat (dA/dz=0, M=1) and continues to accelerate to supersonic speed in the diverging section (dA/dz $>$ 0).

nozzle has a converging and a diverging section. If we look at Eq. 3.15, we see that this converging-diverging duct makes a smooth subsonic-supersonic transition possible: the flow starts subsonic in the converging duct ($\mathfrak{a}(z) < 0$ and $M < 1$), becomes sonic at the throat ($\mathfrak{a}(z) = 0$ and $M = 1$) and is accelerated to supersonic speed in the diverging duct ($\mathfrak{a}(z) > 0$ and $M > 1$). In such configuration it is possible to constantly accelerate the flow along the nozzle (du/dz remains positive). The sonic transition is only possible at the nozzle throat (choking), where $\mathfrak{a} = 0$.
The numerator of the CR-driven wind equation 3.13 presents an "effective area" term given by $a(z) - \frac{g(z)}{c^{*2}}$, which plays the same role of $\mathfrak{a}(z)$ in the De Laval equation. Thus, in order to have a smooth subsonic-supersonic transition, the effective area must have the same convergent-divergent behavior of the De Laval nozzle:

- $\mathbf{u^2 < c^{*2}}$ (subsonic regime)

  the gravitational term $g(z)$ must dominate in the numerator in order to have $du/dz > 0$. Thus, $g(z)$ is a "converging duct" term,

- $\mathbf{u^2 > c^{*2}}$ (supersonic regime)

  the area term $a(z)$ must dominate in the numerator in order to have $du/dz > 0$. Thus, $a(z)$ is a "diverging duct" term.

It is clear from this analysis that if $a(z) = 0$, i.e if the flux-tube area is constant, a wind solution cannot be achieved.
Finally, the passage through the critical point (choking condition for the De Laval nozzle), fixes the wind launching velocity u_0. Because all other magnitudes in Eq. 3.10 and 3.11 are assigned at the wind base, this also fixes the mass and energy flux of the wind.

In order to carry out an analysis of the effects of the input parameters on the flow, it is helpful to define a reference model to which all other cases can be compared. Because we are considering winds launched at the Sun position, we define our reference case starting from observations, reported in Sec. 3.2 and we choose: $z_0 = 100$ pc for the wind base (winds launched near the Galactic disk), $n_0 = 6 \times 10^{-3}$ cm^{-3} for the gas density, $T_0 = 2 \times 10^6$ K for the gas temperature, $P_{c0} = 4 \times 10^{-13}$ erg/cm^3 for the CR pressure, $B_0 = 1\,\mu$G for the magnetic field, $Z_b = 15$ kpc and $\alpha = 2.0$ for the area parameters and NFW-Sofue for the DM profile (see Sec. 3.1). The latter choice is motivated by the fact that the NFW profile is one of the most commonly used models for dark matter halos.
In Fig. 3.3(a)-3.3(c) we reported the wind profiles for the reference case, while in Fig. 3.1(a) the various Galactic gravitational components are shown. Notice that, unlike the bulge and disk components, which die off at ~ 10 kpc, the DM component keeps up the gravitational acceleration up to the virial radius (~ 240 kpc for the NFW-Sofue).
For the reference case, at the wind base the flow is subsonic and sub-Alfvénic and most of the work on the gas is due to the thermal pressure, which is four times larger than the CR pressure. Also CRs contribute to push the gas, however a considerable fraction of their energy is used to generate Alfvén waves, which are quickly damped and heat the gas. This can be seen in Fig. 3.3(b), where it is shown that the gas temperature increases up to ~ 10 kpc and then decreases in z much slower than the gas density. Because of the CR-induced gas heating, also the gas pressure falls off in z slower than it would in the absence of wave damping. Nevertheless the gas pressure decreases with height much faster than the CR pressure, and at ~ 20 kpc CR pressure starts to dominate over the gas pressure. This is due to the fact that CRs have a smaller adiabatic index compared to the gas, which has important consequences on the relative contribution of the thermal and CR pressure to the wind launching. For instance, while the thermal pressure is more efficient in accelerating the gas near the wind base, the CR pressure is able to push the gas also at large z, often making an outflow possible where the thermal pressure alone would have failed (see Ipavich (1975); Breitschwerdt et al. (1991); Everett et al. (2008)). We will discuss this point in detail in Sec. 3.3.1.

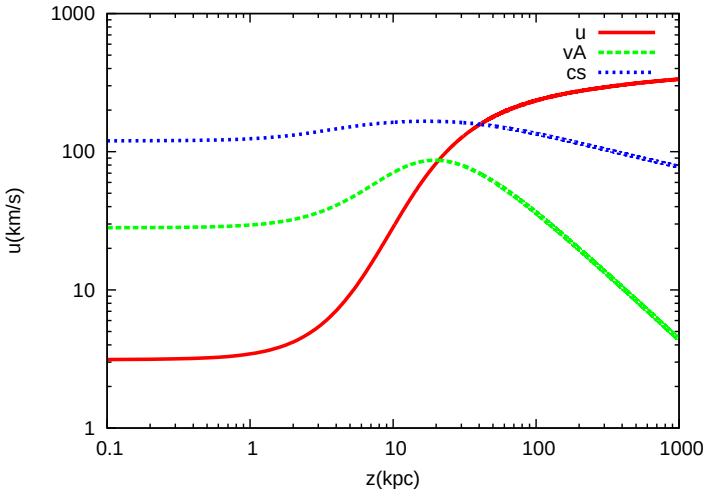

(a) Reference case: velocities.

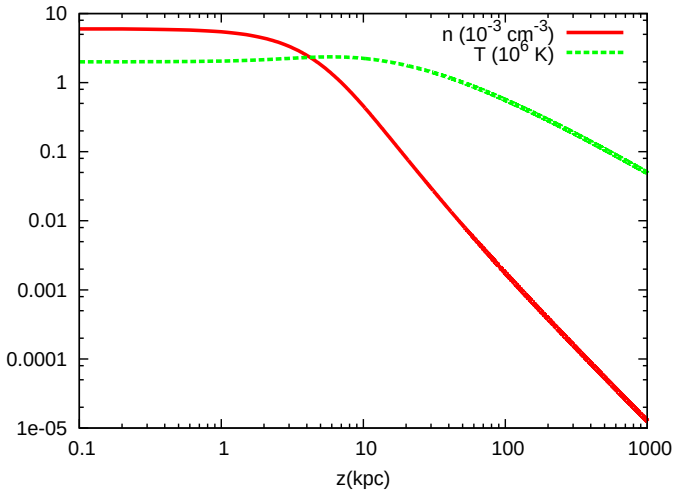

(b) Reference case: gas density and temperature.

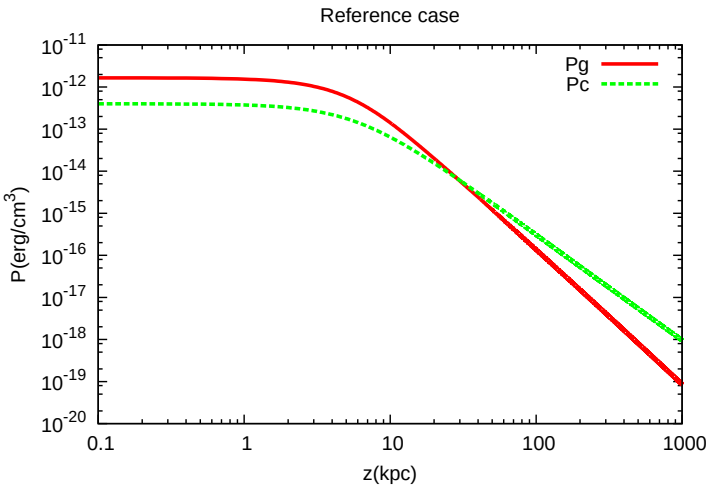

(c) Reference case: pressures.

Figure 3.3: Reference case: a) wind, Alfvén and compound sound speed; b) gas density and temperature; c) gas and CR pressures. The input parameters are: $z_0 = 100$ pc, $n_0 = 6 \times 10^{-3}$ cm^{-3}, $T_0 = 2 \times 10^6$ K, $P_{c0} = 4 \times 10^{-13}$ erg/cm^3, $B_0 = 1\,\mu$G, $Z_b = 15$ kpc, $\alpha = 2.0$ and the NFW-Sofue dark matter profile.

3.3.1 Effect of the gas density and temperature and of the Cosmic Ray pressure

Having defined a reference set of parameters, we study the dependence of the outflow properties on the input parameters at the wind base. Here we focus on the effect of changes of the gas density, gas temperature and CR pressure. An analysis of the dependence on the area parameters and on the DM profile will be presented in Sec. 3.3.2 and Sec. 3.3.3 respectively.
In order to better highlight the dependence on the input parameters, we consider larger intervals compared to those compatible with observations (discussed in Sec. 3.2).

Table 3.3: Dependence of the wind properties on the gas density. The gas temperature (2×10^6 K) and CR pressure (4×10^{-13}erg/cm^3) are fixed. $\dot{m}$ is the mass loss rate of the wind.

Gas density ($n_0^R = 6 \times 10^{-3}$ cm^{-3})	u_0 (km/s)	z_c (kpc)	u_f (km/s)	$\dot{m}$ (4.7×10^{-4}M$_\odot$kpc^{-2}yr^{-1})
0.2	39.7	18.9	595	2.5
0.5	10.7	30.9	428	1.7
1.0	3.1	40.6	403.7	1.0
3.0	0.8	72.2	296	0.73
6.0	0.3	96.5	269	0.53

Table 3.4: Dependence of the wind properties on the gas temperature. The gas density (6×10^{-3}cm^{-3}) and CR pressure (4×10^{-13}erg/cm^3) are fixed.

Gas temperature ($T_0^R = 2 \times 10^6$ K)	u_0 (km/s)	z_c (kpc)	u_f (km/s)
0.5	3.09	34.3	419
1.0	3.1	40.6	403.7
2.0	6.9	104.9	243
3.0	17.5	367.6	152.4
4.0	182	13.32	263
5.0	280	7.8	441.3
6.0	362	4.8	573.5

Table 3.5: Dependence of the wind properties on the CR pressure. The gas density (6×10^{-3}cm^{-3}) and temperature (2×10^6 K) are fixed.

CR pressure ($P_{c0}^R = 4 \times 10^{-13}$erg/cm^3)	u_0 (km/s)	z_c (kpc)	u_f (km/s)
0.2	0.72	64.1	339
0.5	1.84	51.2	351
1.0	3.1	40.6	403.7
2.0	8.6	36.9	376.5
3.0	14.5	32.6	394
4.0	21.8	29.2	415
5.0	30.7	26.2	439.6
6.0	41.1	23.6	573.5

In Table 3.3-3.5 we report the variation of the launching velocity u_0, of the location of the sonic point z_c and of the terminal velocity u_f, when the gas density (Table 3.3), the gas temperature (Table 3.4) and the CR pressure (Table 3.5) are varied compared to the reference case of Fig. 3.3 (indicated by the superscript "R").
The first basic considerations on the possibility for the gas to escape from the Galaxy are based on energetic grounds. Consider for instance what happens at fixed gas density and CR pressure (Table 3.4): for temperatures below $\sim 0.4\, T_0^R$ it is impossible to launch a wind simply because the energy available is too low. In the opposite limit, i.e for temperatures $\sim 7\, T_0^R$, the gas is simply too hot and the outflow is more an evaporation. This case cannot be accounted for in our stationary approach.
At fixed gas temperature and CR pressure, an increase in the gas density leads to a decrease of both the launching and terminal velocities (see Table 3.3). This is not surprising, since a larger mass load makes more difficult for the pressure forces to launch a wind. Notice that the decrease of u_0 with increasing density is fast enough to drive down the mass loss of the wind (which is proportional to $n_0\, u_0$) despite the increasing density (see Table 3.3).
As shown in Table 3.4 and Table 3.5, increasing the temperature or the CR pressure at fixed gas density leads to an increase in the launching velocity (and because n_0 is fixed, also in the mass loss rate). Notice however that multiplying by factor of 6 the temperature and the CR pressure results in an increase of factor $\sim$ 100 and $\sim$14 in u_0 respectively. This fact can be explained keeping in mind that momentum and energy depositions before or after the sonic point affect the wind in different ways (see e.g Lamers &

Cassinelli (1999)): momentum and energy added before the critical point can increase both the mass loss and the terminal velocity, while momentum and energy input after the critical point can only affect the terminal velocity, since the mass loss is determined by the passage through the critical point. The gas adiabatic index (5/3) is larger than the CR adiabatic index ($\sim$ 4/3), implying a larger gas pressure gradient compared to the CR pressure gradient. Thus the thermal pressure is more efficient than the CR pressure at increasing the mass loss. In addition, notice that the z evolution of the CR pressure also depends on whether the flow is sub-Alfvénic or super-Alfvénic. In fact, referring to Eq. 2.12, we have the following limits for the CR pressure gradient (see Everett et al. (2008)):

$$\lim_{u<<v_A} = \gamma_{eff} \frac{P_c}{2\rho} \frac{dP_c}{dz} \tag{3.15}$$

$$\lim_{u>>v_A} = \gamma_{eff} \frac{P_c}{\rho} \frac{dP_c}{dz}. \tag{3.16}$$

The effective CR adiabatic index is $\gamma_{eff}/2$ in the sub-Alfvénic regime and γ_{eff} in the super-Alfvénic regime. For what we said above, CRs are less efficient at driving the wind in the sub-Alfvénic regime than in the super-Alfvénic.
The behavior of the terminal velocity with the gas temperature and the CR pressure is a bit more complicated to explain. In Table 3.4 and Table 3.5 we can see that, when increasing both magnitudes, the terminal velocity in general does not increase. Keeping the gas density and the CR pressure at the reference values and increasing the temperature from $0.5\,T_0^R$ to $3\,T_0^R$, u_f decreases by a factor ~ 3, while from $3\,T_0^R$ to $6\,T_0^R$ it increases by factor of ~ 4. Similarly, keeping the gas density and temperature atthe reference values and increasing the CR pressure from $0.2\,P_{c0}^R$ to P_{c0}^R, u_f increases, then decreases when passing from P_{c0}^R to $2\,P_{c0}^R$, and finally increases when passing from $2\,P_{c0}^R$ to $6\,P_{c0}^R$.
In order to understand this behavior, notice that the terminal velocity is computed from the energy conservation equation 3.11. At large z, where all other quantities drop to zero, all the energy density of the wind goes into kinetic energy of the gas, thus u_f is related to the magnitudes at the wind base through

$$\frac{u_f^2}{2} = \frac{u_0^2}{2} + \frac{\gamma_g}{\gamma_g - 1}\frac{P_{g0}}{\rho_0} + \Phi(z_0) + \frac{\gamma_{eff}}{\gamma_{eff} - 1}\frac{P_{c0}}{\rho_0}\frac{u_0 + v_{A0}}{u_0}. \tag{3.17}$$

Unlike the gas pressure term, which does not depend on u_0, the CR term depends on the Alfvénic Mach number $M_{A0} = u_0/v_{A0}$ through the factor $(1 + M_{A0})/M_{A0}$. This factor becomes large when M_{A0} is small ($\ll 1$) and

approaches unity when M_{A0} gets large ($\gg 1$). Considering the results of Table 3.4, we have that, starting from $0.5\,T_0^R$ and increasing the temperature, the launching velocity and the gas pressure increase, together with the kinetic and gas terms in Eq. 3.17. However, the CR term decreases, due to the factor $(1 + M_{A0})/M_{A0}$. In the range $0.5\,T_0^R - 3\,T_0^R$ the decrease of the CR term dominates over the increase of the kinetic and gas terms, thus leading to a decrease of the terminal velocity with increasing temperature. At larger gas temperature the gas term finally starts to dominate over the CR term and the terminal velocity increases with the gas temperature. Notice that at large temperatures the wind il launched super-Alfvénic ($v_{A0} = 28$ km/s) and the CR term becomes practically independent on M_{A0}. The results of Table 3.5 can be explained with similar considerations.
The location of the sonic point is nearer to the Galactic disk for smaller gas density and for larger gas temperature and CR pressures. This is due to the fact that in all three cases the gas is accelerated more easily and in general reach the sonic point at smaller z.

We conclude this overview with a discussion on the role played by wave damping. In Breitschwerdt et al. (1991) wave damping was considered marginally and the paper mainly analyzed a model where Alfvén waves, produced through CR streaming instability, are not damped and can grow indefinitely. In such model the parameter space for the wind launching was much larger than in the case of wave damping, resulting in the possibility to easily launch winds also at relatively low temperatures and high gas densities. In the presence of wave damping the parameter space is reduced, mainly due to two factors. First, if waves are not damped, their pressure contribution, which grows up to reach more or less the same magnitude as the CR pressure, can significantly help in pushing the gas. Moreover when the waves are damped, the heat input from wave damping increases the temperature (and thus the gas pressure) along z, which results in a smaller gas pressure gradient, i.e a smaller force imparted to the wind. If the contribution of wave damping is too intense, the gas heating can be so important as to make the gas pressure increase with z, thus creating a stall in the outflow. In this situation the wind formation is prevented (see Everett et al. (2008)).

3.3.2 Effect of the flux-tube geometry

In Chapter 2 we have seen that it is possible to solve the wind problem under the assumption that the flow geometry is preassigned and the flow area is given by

$$A(z) = A_0 \left[1 + \left(\frac{z}{Z_b}\right)^{\alpha}\right], \tag{3.18}$$

where z is the distance from the Galactic disk. We have also shown that with such an assumption the wind equations become effectively one-dimensional

(only depend on z) while the gas expansion is accounted for with the increase of the flux area with z. Here we analyze the impact of the flux-tube geometry (i.e of the area parameters α and Z_b) on the wind launching, keeping the gas density, temperature and CR pressure to the reference values of Fig. 3.3 and using the NFW-Sofue DM profile (see Sec. 3.1). The "mushroom" type geometry of Fig. 2.1 has been widely used in the literature of CR-driven winds (see e.g Breitschwerdt et al. (1991); Everett et al. (2008)) and reflects what we would intuitively expect for outflows from disk galaxies: the flow proceeds in nearly cylindrical form up to a certain distance Z_b from the galactic disk and then opens up in a nearly spherical way ($\alpha = 2$ corresponds to spherical opening). Of course, in a full treatment of the CR-driven wind problem, the flow geometry should be calculated self-consistently by accounting for the large-scale magnetic field. However, such study is beyond the scope of the present work, thus we retain the well established geometry of Fig. 2.1 and we study how the wind properties get modified when Z_b and α are changed.

The flux-tube geometry influences directly the flow acceleration, but also the gas density (see Eq. 3.10 and 3.12) and consequently the pressure gradients (see Eq. 2.11 and 2.12). Thus, it is not surprising that the shape of $A(z)$ has an important effect on the wind properties. In what follows we first discuss the effect produced by changing the length scale, Z_b, and then the effect of the exponent α:

- **effect of changing the length scale Z_b**

  We fix $\alpha = 2.0$ and we change Z_b in the range 5-20 kpc, stepped by 2.5 kpc. In Table 3.6 we show the wind launching velocity u_0, the wind terminal velocity u_f and the location of the sonic point z_c as functions of Z_b, while in Fig. 3.4 we report the wind profile for only two cases, $Z_b = 5$ kpc and $Z_b = 20$ kpc.
  It is clear from these plots that at smaller Z_b correspond larger u_0 and z_c and smaller u_f. These results can be explained as follows: at smaller Z_b, the adiabatic expansion of the gas begins at smaller z, resulting in a larger density gradient, as shown in Fig. 3.4(b). Larger density gradients also correspond to larger pressure gradients (see Eq. 2.11 and 2.12) at smaller z. Because of what we said in Sec. 3.3.1, this results in an increase of the wind launching velocity (and, because the gas density is fixed, also in the mass loss rate).
  Notice that, because $v_A = B/\sqrt{4\pi\rho}$ and $BA = const$ (see Eq. 2.9), a steeper density profile also corresponds to a faster fall-off of the Alfvén velocity (see Fig. 3.4(a)). This leads, at smaller Z_b, to a flow which is typically "more super-Alfvénic" along z, causing a more efficient CR wind driving (see the discussion in Sec. 3.3.1), i.e an extra contribution to the increase of u_0.

Table 3.6: Dependence of the wind properties on the area length scale Z_b. The gas density (3×10^{-3}cm^{-3}), gas temperature (2×10^6 K) and CR pressure (4×10^{-13}erg/cm^3) are fixed. $\alpha = 2.0$.

Z_b (kpc)	u_0 (km/s)	z_c (kpc)	u_f (km/s)
5.0	4.3	189.9	218.4
7.5	4.0	89.7	266.0
10.0	3.7	56.4	315.7
12.5	3.4	44.9	362.6
15.0	3.1	40.6	403.7
17.5	2.9	39.0	439.0
20.0	2.8	38.6	469.1

Being all parameters at the wind base fixed, the increase of the wind launching velocity with decreasing Z_b results in a decrease of the CR term and in an increase in the kinetic term in the energy conservation equation 3.11. However, in the case considered, the first effect is dominant, and the terminal velocity decreases with decreasing Z_b.

In the subsonic regime, the numerator of the wind equation 3.12 is dominated by the gravitational term (see discussion at the beginning of this chapter). A smaller Z_b makes the term $a(z)$ become important at smaller z (the area starts to open up at smaller z), while, as it can be seen in Fig. 3.4(a), c^* depends weakly on Z_b. This results in a flatter velocity profile at smaller Z_b. The larger launching velocity at smaller Z_b does not compensate the decrease in acceleration, leading to a sonic point located at larger z.

- **Effect of changing the expansion index α**

Now we fix $Z_b = 15$ kpc and we vary α in the range 1.2-2.2, stepped by 0.2. In Table 3.7 we show the wind launching velocity u_0, the wind terminal velocity u_f and the location of the sonic point z_c as functions of α. In Fig. 3.5 we report the wind properties only for the two extreme cases $\alpha = 1.2$ and $\alpha = 2.2$.

Table 3.7: Dependence of the wind properties on the expansion index α. The gas density (3×10^{-3}cm^{-3}), gas temperature (2×10^6 K) and CR pressure (4×10^{-13}erg/cm^3) are fixed. $Z_b = 15$ kpc.

α	u_0 (km/s)	z_c (kpc)	u_f (km/s)
1.2	2.5	73.0	513.6
1.4	2.7	61.2	482.0
1.6	2.9	52.6	453.5
1.8	3.0	45.9	427.6
2.0	3.1	40.6	403.7
2.2	3.3	36.2	382.0

As it can be inferred from these plots, larger value of α corresponds to smaller z_c, larger u_0 and smaller u_f. This behavior can be explained with considerations analogous to those for the area scale height Z_b. At $z > Z_b$, an increase in α corresponds to steeper density profiles (see Fig. 3.5(b)), i.e to larger pressure gradients, which act both in the subsonic and in the supersonic region (notice that in all cases $z_c > Z_b$). For this reason, when α increases the launching velocity increases (and consequently also the mass loss rate increases), while the terminal velocity decreases. Notice also that, as it can be seen in Fig. 3.5(a), the compound sound speed c^* does not change much when changing α, especially in the subsonic regime, and that, since Z_b is fixed, the flux tube area $A(z)$ does not change much for $z < Z_b$ for the analyzed cases. This leads to velocity profiles which are practically parallel up to $\sim Z_b$ at all α (see Eq. 3.12 and Fig. 3.5(a)), and to a decrease of z_c when α increases. In fact, because the velocity profiles are nearly parallel within $\sim Z_b$ and c^* is weakly dependent on α in the subsonic regime, at larger u_0 correspond smaller z_c.
Finally, notice the steeper c^* profile at $z > Z_b$ corresponding to larger α. This is due to a more rapid fall off in z of the density and pressures.

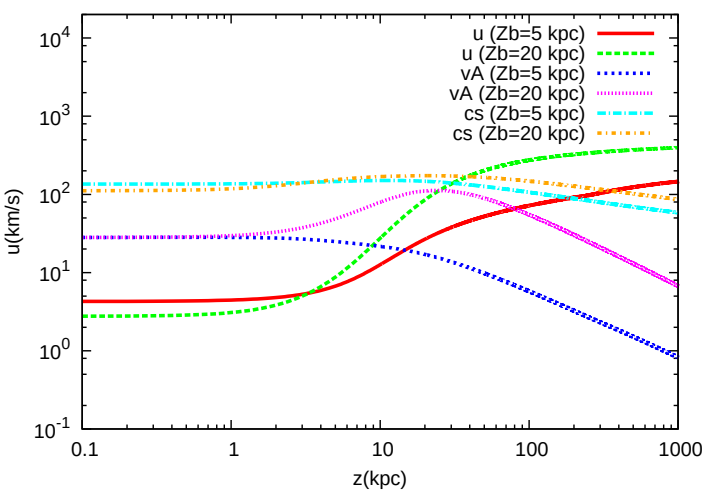

(a) Changing Z_b: velocities.

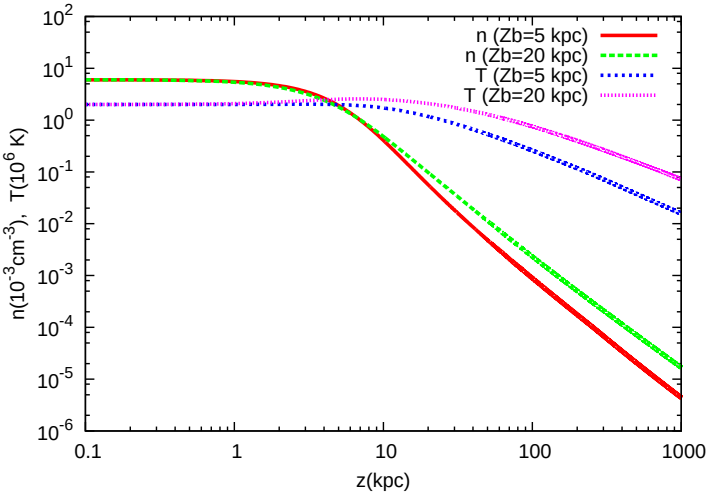

(b) Changing Z_b: gas density and temperature.

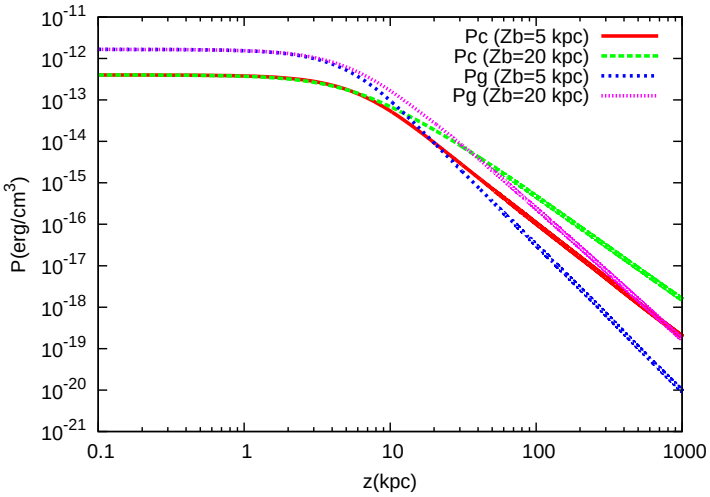

(c) Changing Z_b: pressures.

Figure 3.4: Comparison of wind profiles in case of changing the flux tube geometry. Two cases are shown, $Z_b = 5$ kpc and $Z_b = 20$ kpc, while the value of α is fixed to 2. The different plots are: a) wind, Alfvén and compound sound speed; b) gas density and temperature; c) gas and CR pressure.

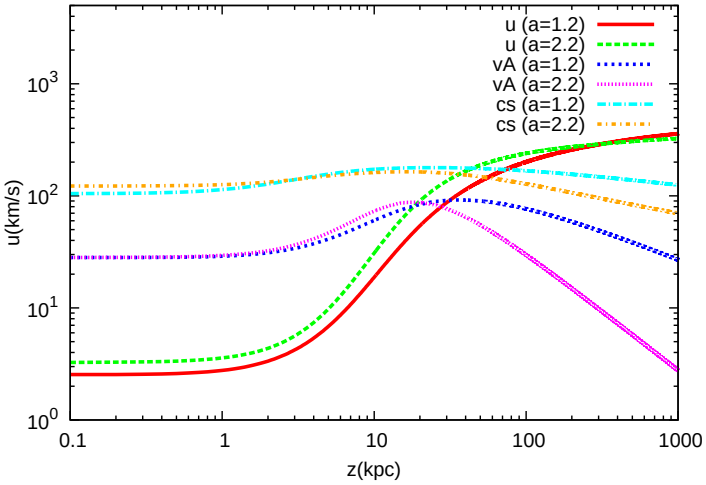

(a) Changing α: velocities.

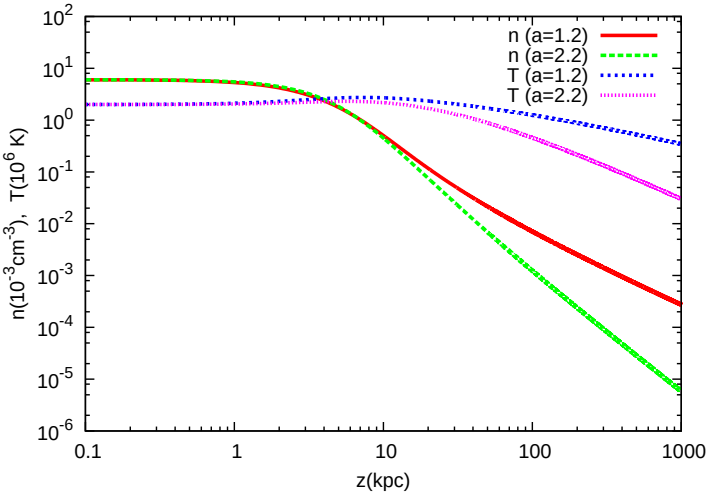

(b) Changing α: gas density and temperature.

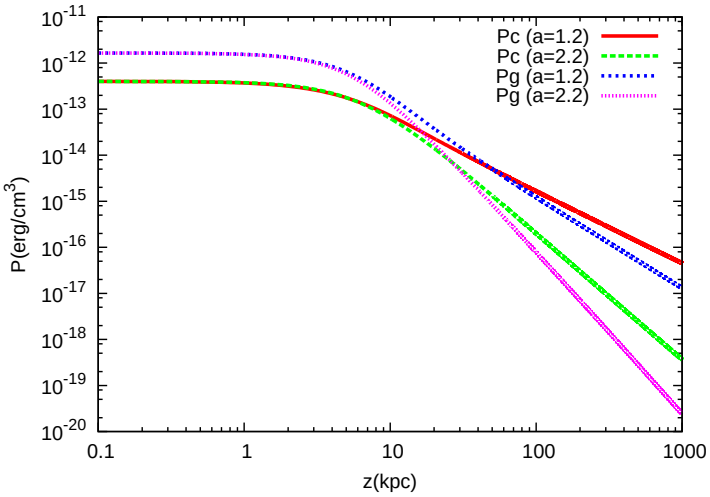

(c) Changing α: pressures.

Figure 3.5: Comparison of wind profiles in case of changing the flux tube geometry. Two cases are shown, $\alpha = 1.2$ and $\alpha = 2.2$, while the value of Z_b is fixed to 15 kpc. The different plots are: a) wind, Alfvén and compound sound speed; b) gas density and temperature; c) gas and CR pressures.

3.3.3 Effect of the Dark Matter profile

In Sec. 3.1, we described the DM profiles which we consider in our analysis. The corresponding gravitational accelerations at the Sun Galactocentric

distance are shown in Fig. 3.1(a). Notice that the four profiles are quite different below $\sim 30-50$ kpc, with NFW-Salucci showing the larger acceleration and the INN the smaller. In addition, the two NFW profiles dominate over the bulge and disk components practically at all z.

Table 3.8: Dependence of the wind properties on the dark matter profile. The gas density (3×10^{-3}cm^{-3}), gas temperature (2×10^6 K) and CR pressure (4×10^{-13}erg/cm^3) are fixed. $Z_b = 15$ kpc and $\alpha = 1.5$.

DM halo	u_0 (km/s)	z_c (kpc)	u_f (km/s)
NFW-Sofue	2.78	56.6	467.4
BUR	5.0	241.8	304.5
INN	8.9	298.1	243.0

Here we fix the gas density, gas temperature and the CR pressure to the reference values (see Fig. 3.3), $\alpha = 1.5$ and $Z_b = 15$ kpc, and we solve the hydrodynamic wind problem for the different DM profiles. In Fig. 3.6 we show the wind profiles obtained for different DM models. The NFW-Salucci model is missing since, with the chosen input parameters, a wind solution was not found, while it was found for the other three DM models. This is a typical example of how, fixed any other parameter, an increase of the gravitational pull (the NFW-Salucci has the largest force among the proposed models) could prevent the wind launching.
At larger gravitational acceleration, i.e for the NFW-Sofue profile, we get a smaller launching velocity u_0, a smaller z_c and a larger terminal velocity u_f. The u_0 trend can be accounted for if we consider the fact that the wind has to be launched against the gravitational force, and given all other parameters, an increase in the gravitational acceleration causes a decrease of the mass loss. As explained in Sec. 3.3.1, a decrease in u_0 causes an increase of the CR energy density (see Eq. 3.11). For the cases shown in this analysis, the increase of the CR energy term dominates over the decrease of the kinetic energy density ($u_0^2/2$), leading to an increase of the terminal velocity (see Table 3.8).
Finally, notice that in the subsonic regime the gravitational term dominates the numerator of the wind equation 3.12, while c^* is weakly dependent on the DM profile (see Fig. 3.6(a)). Thus a larger gravitational force leads to a larger gas acceleration in the subsonic region, large enough to give a smaller z_c despite the smaller launching velocity, as it can be seen in Fig. 3.6(a).

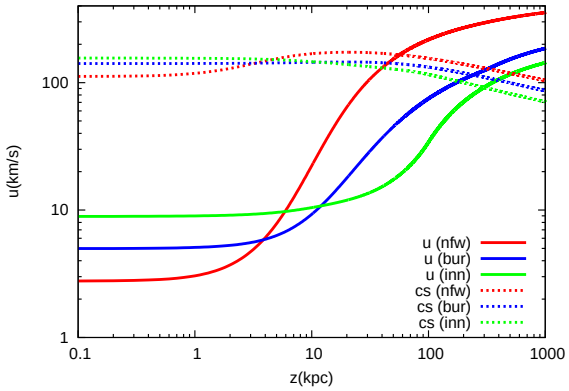

(a) Wind and compound sound speed.

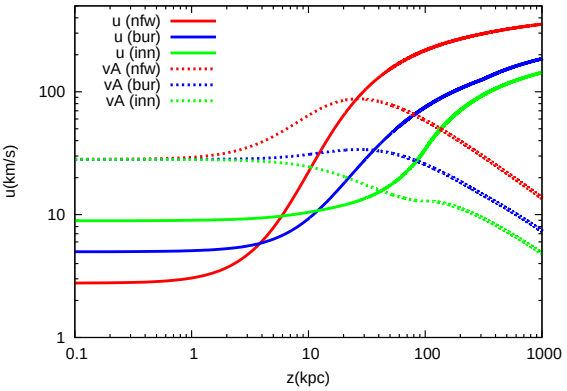

(b) Wind and Alfvén speed.

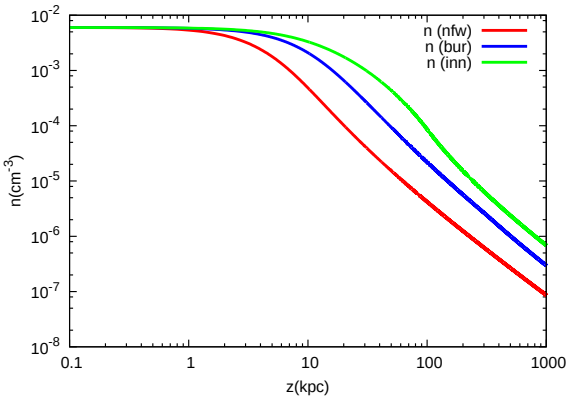

(c) Gas density.

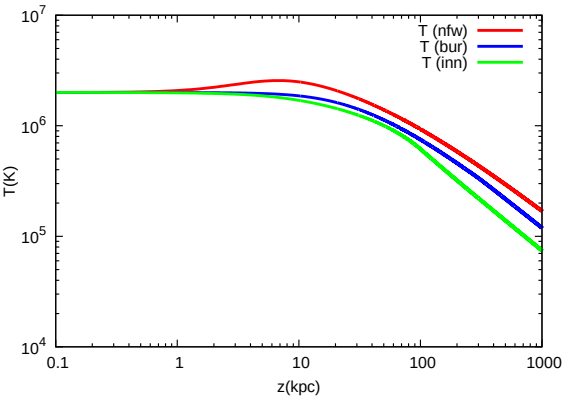

(d) Gas temperature.

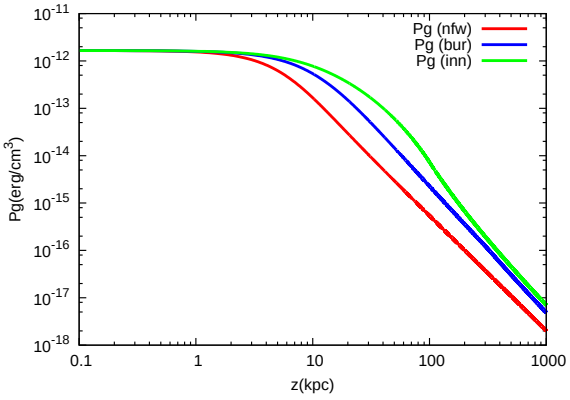

(e) Gas pressure.

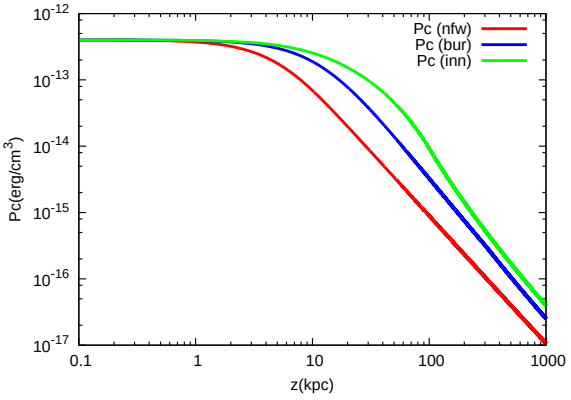

(f) CR pressure.

Figure 3.6: Comparison of wind profiles in case of changing the dark matter halo model. Three cases are shown, the NFW-Sofue, the Burkert and the Innanen profiles. The different plots are: a) wind and compound sound speed; b) wind and Alfvén speed; c) gas density; d) gas temperature; e) gas pressure; f) CR pressure.

3.3.4 Comments on the radiative cooling

We conclude this Chapter discussing the role of radiative cooling of the gas, a process that we have neglected so far.
For temperatures of the ISM of order $\sim 10^6$ K the radiative cooling may be important. As shown by Dalgarno & McCray (1972), at these temperatures the ISM is cooled by the emission of forbidden lines and soft X-rays, at a rate

$$\frac{1}{T}\frac{dT}{dt} \sim \Lambda(T) n^2. \tag{3.19}$$

The cooling function is $\Lambda(\mathrm{T} \sim 10^6) \sim 2 \times 10^{-23}$ erg cm^3/s. Notice the strong dependence on the gas density.

From the formal point of view, radiative cooling can be easily included in the wind hydrodynamic equations: Eq. 2.11 for the gas pressure becomes

$$\frac{dP_g}{dz} = \gamma_g \frac{P_g}{\rho}\frac{d\rho}{dz} - (\gamma_g - 1)\frac{v_A}{u}\frac{dP_c}{dz} - (\gamma_g - 1)\Lambda(T)\frac{n^2}{u}, \tag{3.20}$$

while the wind equation 2.10 gets modified as

$$\frac{1}{u}\frac{du}{dz} = \frac{c_*^2\, a(z) - g(z) + (\gamma_g - 1)\Lambda(T)\frac{n}{u}}{u^2 - c_*^2}. \tag{3.21}$$

These expressions have been derived also byDougherty et al. (1990), where it was also shown that the solution topology illustrated in Sec. 2.2 holds also with the addition of radiative cooling. Notice that the cooling term appears in the numerator of the wind equation 3.21 with the same sign of the area term, i.e as a "diverging duct" term in the De Laval nozzle picture.
Confronting the radiative cooling time and the wave heating time for the reference case of Fig. 3.3, we have $\tau_{cool} \sim 10^7$ yr and $\tau_{heat} \sim 10^8$ yr. This example shows that, in the absence of additional heating terms, the radiative cooling can be a quite fast process near the Galactic disk (where the gas density is larger) and can in principle prevent the wind launching. From the formal point of view, a large cooling term would result in a positive numerator at the wind base in Eq. 3.21, making a wind solution impossible (see the discussion of Sec. 3.3).
On the other hand, the ISM is also heated by SN explosions through the injection of hot gas and magnetic turbulence that will eventually decay into thermal energy. Recently it was suggested that also Coulomb losses of CRs themselves might be a substantial source of heating (Walker, 2016).
The relevance of cooling was already recognized by Breitschwerdt et al. (1991) which, nevertheless, assumed that energy balance exist between heating and cooling processes. Which process dominates the heating is at the moment unclear but observations reveal that the temperature in the halo reaches $\sim 10^5 - 10^6$ K (see for instance Miller & Bregman (2015)), hence

supporting the idea that either the cooling is negligible or it is balanced by heating processes. It is worth to remark that the expression (3.19) is valid assuming solar metallicity. In case of smaller metallicity, as it is expected for the gas in the halo, the cooling rate is somewhat reduced.
In this thesis we decided, in line with Breitschwerdt et al. (1991), to assume that radiative cooling is balanced by some heating processes, and not to include it in our analysis.

Chapter 4

Cosmic Ray spectrum

In Chapter 3 we illustrated how the wind properties depend on the input parameters. We carried out our analysis only considering winds launched at the Galactocentric distance of the Sun ($R_\odot \sim 8.5$ kpc) and near the Galactic disk ($z_0 \sim 100$ pc). This information is important since, not only the Galactic gravitational potential depends on the position in the Galaxy, but also the CR spectrum and pressure at the Sun position are measured ($P_{CR\odot} \sim 4 \times 10^{-13}$ erg/cm^3), providing a strong constraint on our wind model. As it has been pointed out in Chapter 2, the CR spectrum depends in a non-linear way from the transport properties (advection and diffusion) and from the injection spectrum (see Eq. 2.17). However, the injection spectrum can be normalized either to obtain the observed CR pressure, either to match the computed spectrum with the observed spectrum at one specific energy (for instance 50 GeV). This can be done both by changing the injection efficiency or the source rate in Eq. 2.28. In Chapter 3 we fixed the CR pressure, here we use both approaches. Notice that neither normalization of the injection spectrum guarantees that the CR spectrum, computed self consistently with the wind properties (as illustrated in Chapter 2) matches observations. And in fact usually it is not the case, and often happens that reasonable values for the input parameters lead to a spectrum totally different from the one observed.
In Sec. 4.1 we address this issue (see Recchia et al. (2016a)) by presenting some selected cases in which we solve the wind problem for input parameters suitable for the Sun position (see Sec. 3.2) and we check the computed spectrum versus observations. As we will show, a discrepancy at low CR energies ($\lesssim 50GeV$) is usually caused by a too large advection velocity at the wind base (in most cases dominated by the Alfvén speed near the launching point), which flattens the low energy CR spectrum. In some cases, the advection velocity can be so large as to dominate the CR transport up to energies of hundreds of GeV. A smaller Alfvén speed (and possibly a smaller wind speed) is obtained by launching the wind with larger gas density (and/or at smaller

magnetic field). However, for density values large enough to match the low energy CR spectrum, it can happen that the wind is not launched. In these borderline cases, once fixed all other parameters, the DM halo gravitational potential can determines whether the wind is launched and the quality of the agreement with the observed spectrum. At higher CR energies (above $\gtrsim 200$ GeV) the opening of the flux-tube area (see Fig. 2.1) together with the energy dependence of the self-generated diffusion coefficient (see Eq. 2.18) makes the CR spectrum steeper than the observed one.

In all these considerations, similarly to what we did in Chapter 3, we assume that the wind is launched near the Galactic disk. In doing so, we implicitly assume that the ionized part of the ISM, where the coupling of CRs and plasma is strong and the wind launching can take place, is physically separated from the neutral component even in the near disk region. This picture could be realistic if the neutral component of the ISM is mainly clumped in clouds with a small filling factor (see e.g Ferrière (2001)). However, other scenarios are possible. For instance, in case the neutral and ionized components are not separated enough, ion-neutral damping is expected to damp self-generated Alfvén waves within $\sim 0.5 - 1$ kpc from the Galactic disc (see also Sec. 1.1.3). In this region the coupling between CRs and gas would be too weak and the wind quenched. The wind can however be launched above this region, where the neutral component becomes negligible. Breitschwerdt et al. (1991) considered such scenario and took $z_0 = 1$ kpc as the wind launching point. In Sec. 4.2 we examine a similar situation by assuming that winds are launched at some distance from the Galactic disc, while the CR transport in the near-disc region is assigned by speculating that some type of turbulence may be maintained in the near-disc region, due for instance to SN explosions, though the waves will be assumed to be isotropic, so that the effective Alfvén speed is zero (see Recchia et al. (2016a)). We will show that such setup has prominent consequences on the CR spectrum.

Finally, in Sec. 4.3, we discuss the impact of the DM halo profile on the CR spectrum, and we show that it is possible to find a wind model which is consistent both with the recent observations discussed in Miller & Bregman (2015) and with the observed CR spectrum.

4.1 Reference models

The wind solution depends on several parameters, hence, in order to make the discussion more fluent we decided to present three different scenarios, named Model-A, Model-B and Model-C. In all three cases we solve the wind problem (as described in Chapter 2) in the assumption that the wind is launched at the Sun position (Galactocentric distance $R_\odot = 8.5$ kpc, $z_0 = 100$ pc), and

by fixing the gas temperature to $T_0 = 2 \times 10^6$ K, the slope of the injection spectrum to $\gamma = 4.3$, the parameters of the flux-tube geometry to $Z_b = 15$ kpc and $\alpha = 1.5$ and by using the NFW-Sofue dark matter profile. The three scenarios differ in the values of the gas density n_0 and magnetic field B_0 at the wind base and in the normalization of the CR injection spectrum (which is normalized either to obtain the observed CR pressure, either to match the computed spectrum with the observed spectrum at 50 GeV):

- **Model-A:**

  we assume the gas density $n_0 = 0.003$ cm^{-3} and the magnetic field $B_0 = 2\,\mu$G at the wind launching point z_0. In addition, we normalize the injection spectrum in order to get the observed CR pressure $P_{c0} = 4 \times 10^{-13}$ erg/cm^3 at z_0. For this reason, we are bound to take

  $$\frac{\xi_{CR}}{0.1} \frac{\mathcal{R}_{SN}}{1/30\,\mathrm{yr}^{-1}} \approx 1.1$$

  in the injection spectrum (see Eq. 2.28). The results are summarized in the plots of Fig. 4.1 and 4.2, that we comment in what follows. The solution for the wind density and temperature are shown in Fig. 4.1(b), while Fig. 4.1(a) shows the wind velocity, the Alfvén speed and the compound sound speed. The wind is launched sub-Alfvénic with $u_0 = 14$ km/s and becomes sonic at $z_c = 35$ kpc, while the Alfvén speed at z_0 is 79 km/s. The CR pressure is shown in Fig. 4.1(c), together with the gas pressure and the CR pressure as derived from the kinetic calculation: the fact that the latter is basically overlapped to the CR pressure as derived from the hydrodynamic calculations shows that the method of solution described in Chapter 2 reached convergence. This is true for all the cases presented in this work. The wave pressure shown in Fig. 4.1(c) is computed from the equilibrium wave spectrum, obtained by equating the growth rate of waves due to CR streaming instability and the damping rate due to NLLD (see Eq. 2.21). Notice that the wave pressure is much smaller than the gas and CR pressure, thereby justifying a posteriori the fact that it is neglected in the hydrodynamic equations. In Fig. 4.1(d) we report the CR spectrum at z_0 together with the VOYAGER and AMS-02 data. The red curve also includes the effect of the solar modulation (see e.g Bernardo et al. (2010)). Finally, in Fig. 4.2(a) and 4.2(b) we show the CR distribution function and diffusion coefficient respectively at different heights from the Galactic disk, while in Fig. 4.2(c) we show the effective boundary, $s_*(p)$, between the wind regions where the CR transport is dominated by diffusion or by advection. Notice that, as anticipated in Sec. 1.1.2, $s_*(p)$ is a growing function of momentum.

- **Model-B:**

  as for model-A, we assume the gas density $n_0 = 0.003$ cm^{-3} and the magnetic field $B_0 = 2\,\mu$G at the wind launching point z_0. However, we normalize the injection spectrum in order to reproduce the observed CR spectrum at 50 GeV. For this reason, we are bound to take

  $$\frac{\xi_{CR}}{0.1}\frac{\mathcal{R}_{SN}}{1/30\,\mathrm{yr}^{-1}} \approx 0.75.$$

  The results for the wind density and temperature are shown in Fig. 4.3(b), while the wind velocity, the Alfvén speed and the compound sound speed are shown in Fig. 4.3(a). The wind is launched sub-Alfvénic with $u_0 = 9$ km/s and becomes sonic at $z_c = 39$ kpc, while the Alfvén speed at z_0 is 79 km/s. The CR pressure is shown in Fig. 4.3(c), together with the gas pressure and wave pressure (also in this case the wave pressure is small compared to the gas and CR pressure). Notice that, because we are not imposing the CR pressure at z_0, the latter is an output of the calculation, with value $P_{c0} = 2.6 \times 10^{-13}$ erg/cm^3. This explains the difference in wind velocity between model-A and model-B. Finally, in Fig. 4.3(d) we compare the CR spectrum at z_0 with the VOYAGER and AMS-02 data.

- **Model-C:**

  We assume the gas density $n_0 = 0.006$ cm^{-3} and the magnetic field $B_0 = 1\,\mu$G at the wind launching point z_0. As for model-B, we normalize the injection spectrum in order to reproduce the observed CR spectrum at 50 GeV. For this reason, we are bound to take

  $$\frac{\xi_{CR}}{0.1}\frac{\mathcal{R}_{SN}}{1/30\,\mathrm{yr}^{-1}} \approx 0.32.$$

  The wind density and temperature are shown in Fig. 4.4(b). In Fig. 4.4(a), we show the wind velocity, the Alfvén speed and the compound sound speed. The wind is launched sub-Alfvénic with $u_0 = 2$ km/s and becomes sonic at $z_c = 60$ kpc, while the Alfvén speed at z_0 is 28 km/s. The CR pressure is shown in Fig. 4.4(c), together with the gas and the wave pressure. As for model-B, because we are not imposing the CR pressure at z_0, the latter is an output of the calculation, with value $P_{c0} = 3.2 \times 10^{-13}$ erg/cm^3. Finally, in Fig. 4.4(d) we compare the CR spectrum at z_0 with the VOYAGER and AMS-02 data.

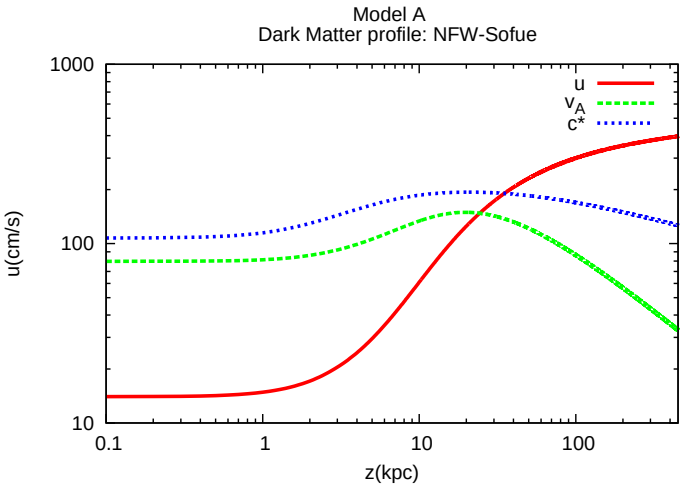

(a) Wind velocity, Alfvén velocity and sound speed.

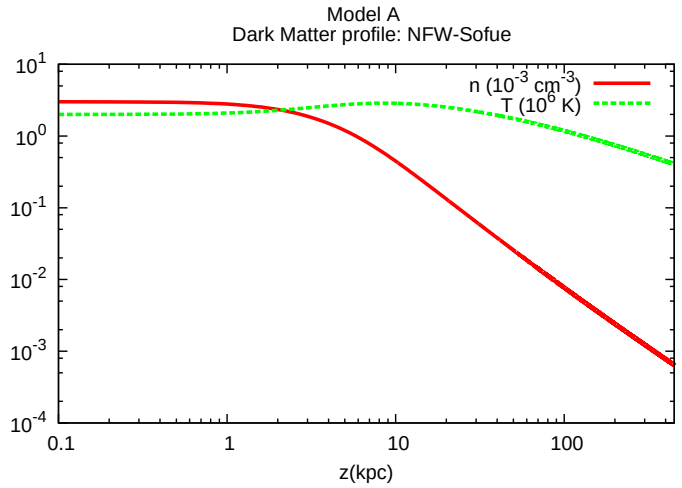

(b) Density in units of $10^{-3}\mathrm{cm}^{-3}$ and temperature in units of 10^6 K.

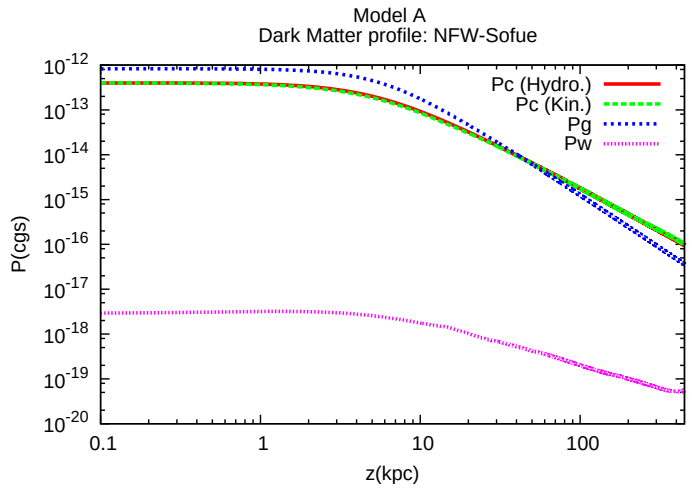

(c) Gas pressure, CR pressure obtained from the hydrodynamic and kinetic calculations, wave pressure obtained from the CR transport equation.

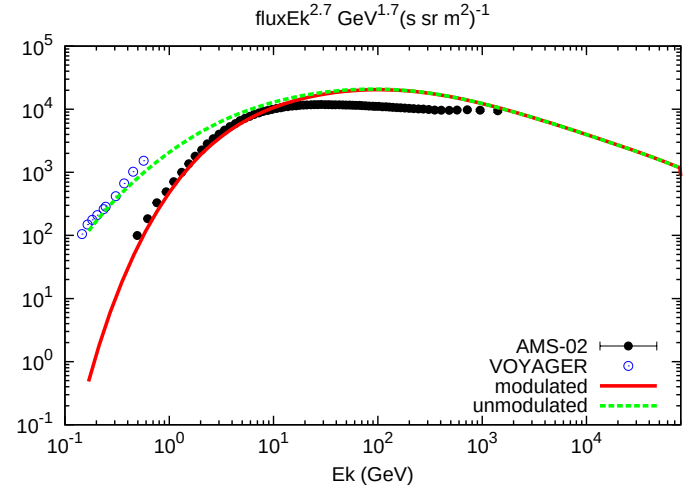

(d) CR spectrum compared to the VOYAGER and AMS-02 data. Solar modulation has been applied with Φ =500 MV.

Figure 4.1: Results for Model-A: at the wind base, z_0, the gas density is $n_0 = 3 \times 10^{-3}\mathrm{cm}^{-3}$ and the magnetic field is $B_0 = 2\mu$G. The CR injection spectrum has been normalized in order to get the observed CR pressure $P_{c0} = 4 \times 10^{-13}$ erg/cm^3 at z_0.

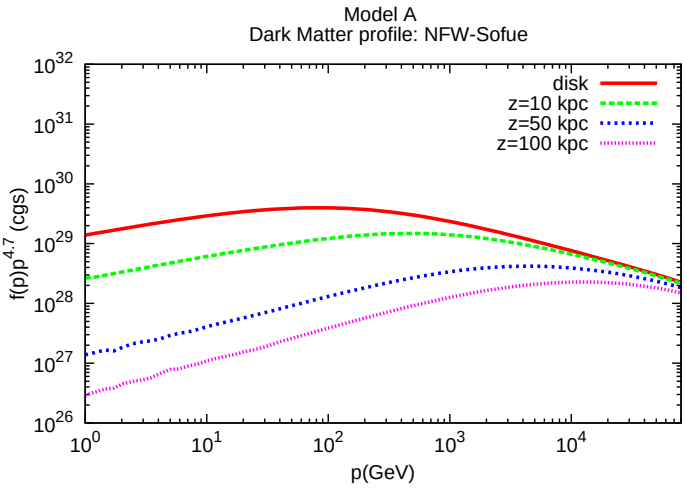

(a) CR spectrum, $f(p) \times p^{4.7}$, at different locations in the wind: wind base, z = 10 kpc, z = 50 kpc and z = 100 kpc.

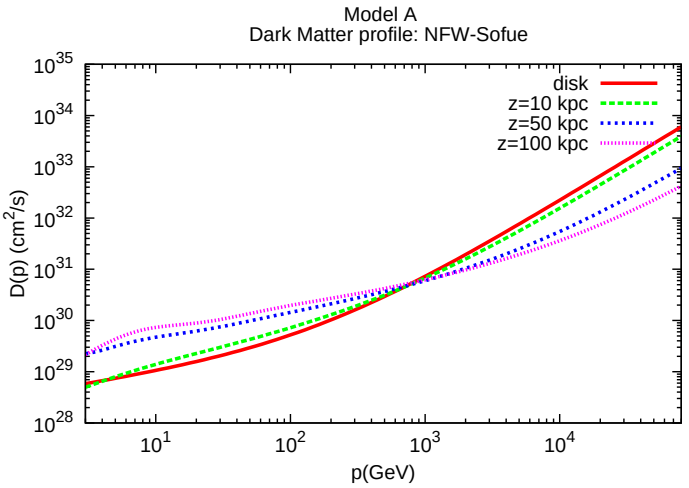

(b) Self-generated diffusion coefficient, D(p), at different locations in the wind: wind base, z = 10 kpc, z = 50 kpc and z = 100 kpc. The transition from the cylindrical to the spherical geometry of the wind flow is clearly visible in the momentum dependence of D(p)

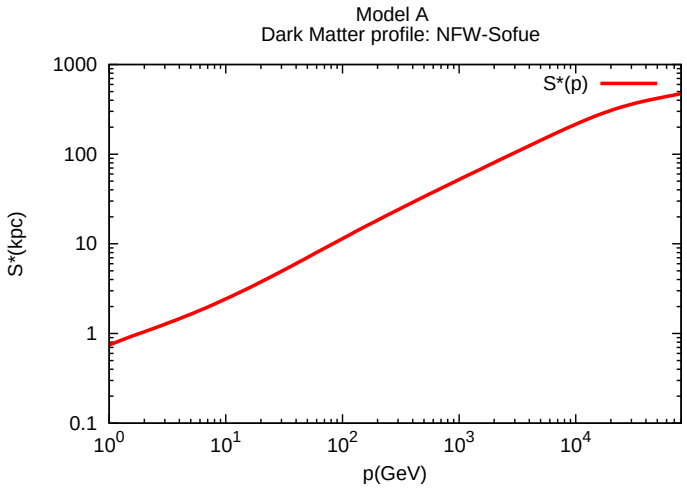

(c) Effective boundary, $s_*(p)$, between the diffusion dominated and the advection dominated region of the wind.

Figure 4.2: Results for Model-A (continued): at the wind base, z_0, the gas density is $n_0 = 3 \times 10^{-3}\mathrm{cm}^{-3}$ and the magnetic field is $B_0 = 2\mu\mathrm{G}$. The CR injection spectrum has been normalized in order to get the observed CR pressure $P_{c0} = 4 \times 10^{-13}$ erg/cm^3 at z_0.

In all the three cases the CR advection velocity near the wind base is dominated by the Alfvén speed, which is non-zero at the base of the wind, because of a non zero strength of the magnetic field orthogonal to the galactic plane. The advection velocity at the wind base is $u_0 + v_{A0} \sim 93$ km/s, ~ 88 km/s and ~ 30 km/s for model-A, B and C respectively. An important feature of the spectra at the disk, shown for the three models in Fig. 4.5(a), is the spectral hardening with increasing advection velocity. In fact, as it can be seen from Fig. 4.5(b), where the slope of the three spectra as a function of momentum is reported, the spectrum for Model-A is systematically flatter than that for Model-B, which in turn is flatter than the spectrum for Model-C. This is due to the fact that, the larger the CR advection velocity, the higher the CR energy at which advection dominates the CR transport, thus producing a spectrum with spectral index near the injection spectral index (see Sec. 1.1.1).
From Fig. 4.4(d), we can see that below ~ 200 GeV Model-C reproduces well the observed CR spectrum, while the larger spectral hardness of Model-A and Model-B leads to spectra which do not resemble the observed spectrum. This is a crucial point, since for all the three models we adopted environmental parameter values which are compatible with observations (see Sec. 3.2). Exploiting the results of Chapter 3 on the dependence of the wind properties on the launching parameters, we can infer what would happen by changing the gas density and temperature and the magnetic field at the wind base (always within the observational constraints). By increasing the magnetic field and/or decreasing the gas density we would obtain an increase in the Alfvén speed and, consequently, harder spectra. In addition, a decrease of the gas density, as well as an increase of the gas temperature, leads to an increase of the wind launching velocity, with a similar result on the CR spectrum.
On the other hand, an increase in the gas density would lead to smaller advection velocities (both decreasing the Alfvén and the wind speed), i.e to a generally steeper spectrum. However, when the density is above a certain threshold it may become impossible to launch winds. The same consideration holds when decreasing the gas temperature: the Alfvén speed is not affected but the wind velocity decreases. This situation is particularly important for winds in which the launching velocity is comparable or larger than the Alfvén speed. Also in this case at smaller temperatures the wind launching may be prevented.

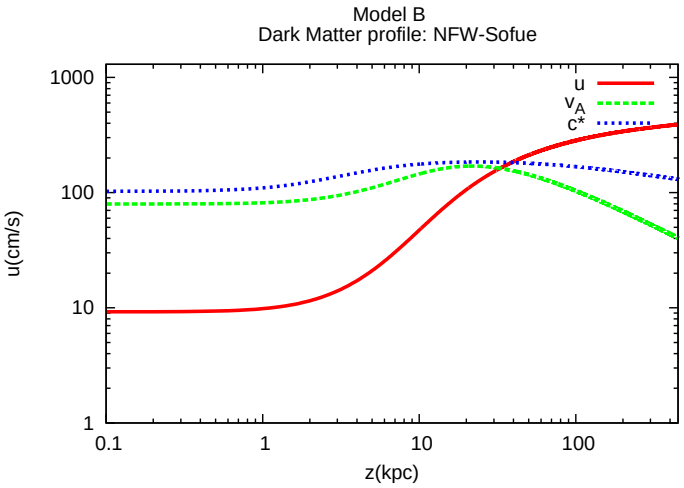

(a) Wind velocity, Alfvén velocity and sound speed.

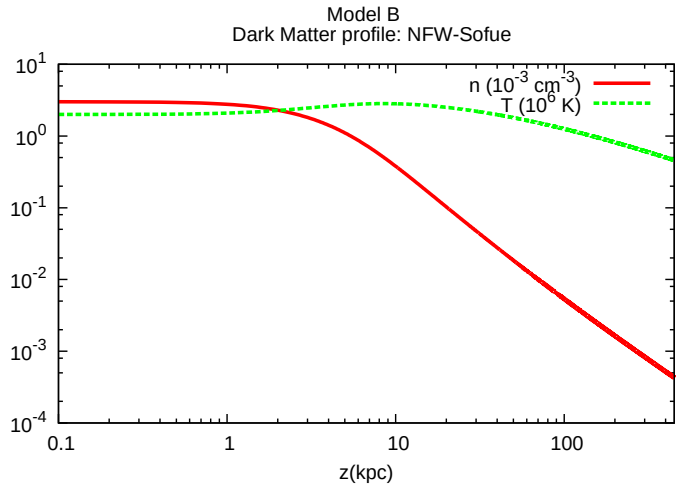

(b) Density in units of 10^{-3}cm^{-3} and temperature in units of 10^6 K.

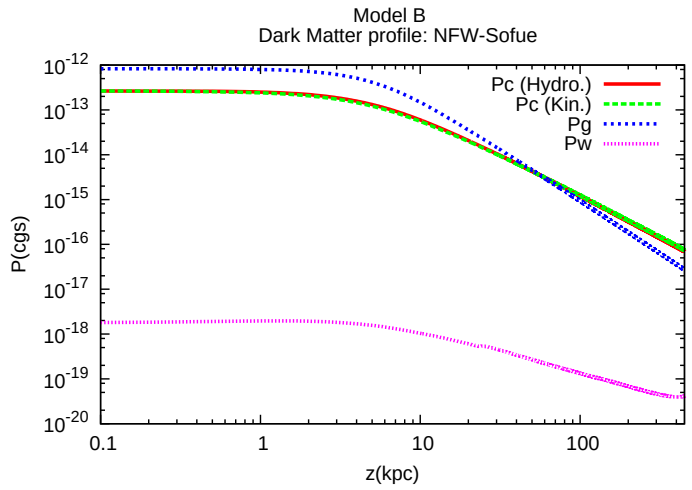

(c) Gas pressure, CR pressure obtained from the hydrodynamic and kinetic calculations, wave pressure obtained from the CR transport equation.

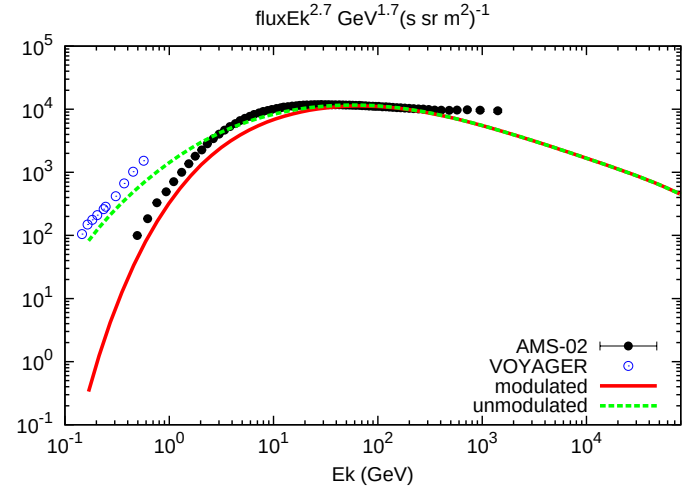

(d) CR spectrum compared to the VOYAGER and AMS-02 data. Solar modulation has been applied with Φ =500 MV.

Figure 4.3: Results for Model-B: at the wind base, z_0, the gas density is $n_0 = 3\times10^{-3}$cm^{-3} and the magnetic field is $B_0 = 2\mu$G. The CR injection spectrum has been normalized in order to reproduce the observed CR spectrum at 50 GeV.

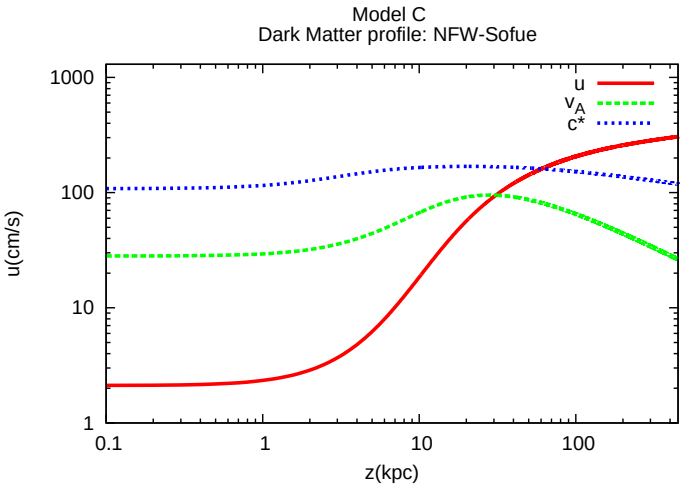

(a) Wind velocity, Alfvén velocity and sound speed.

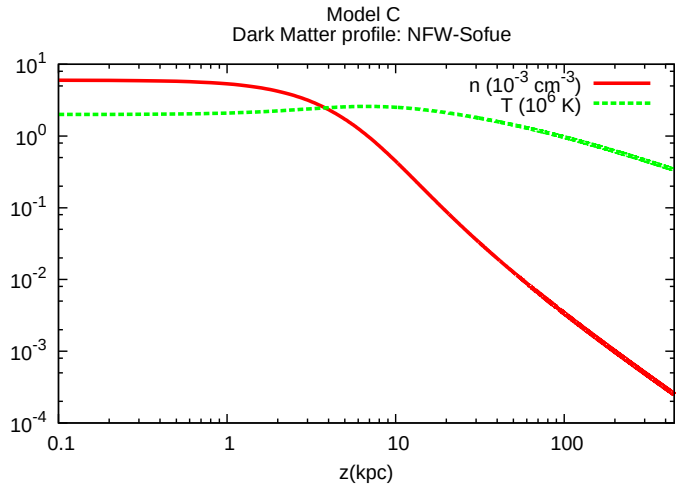

(b) Density in units of 10^{-3}cm^{-3} and temperature in units of 10^6 K.

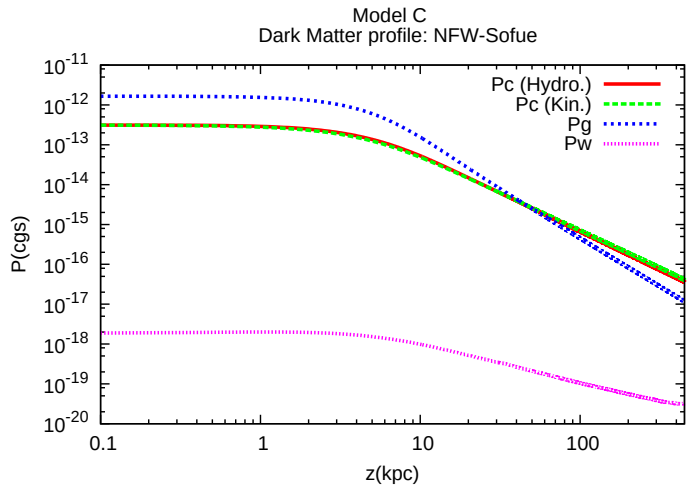

(c) Gas pressure, CR pressure obtained from the hydrodynamic and kinetic calculations, wave pressure obtained from the CR transport equation.

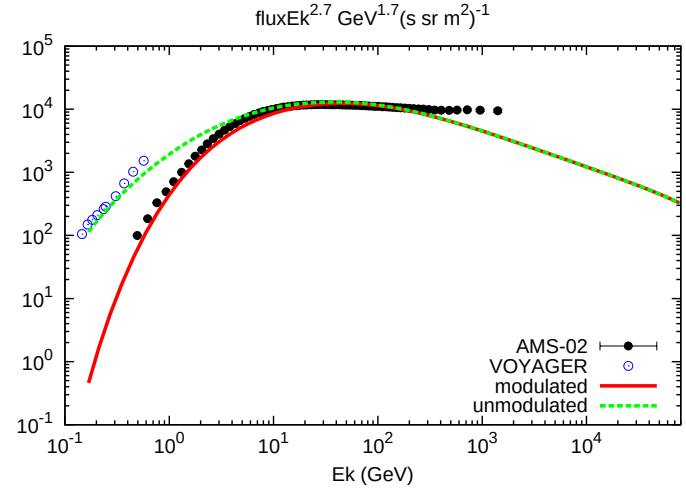

(d) CR spectrum compared to the VOYAGER and AMS-02 data. Solar modulation has been applied with Φ =500 MV.

Figure 4.4: Results for Model-C: at the wind base, z_0, the gas density is $n_0 = 6{\times}10^{-3}$cm^{-3} and the magnetic field is $B_0 = 1\mu$G. The CR injection spectrum has been normalized in order to reproduce the observed CR spectrum at 50 GeV.

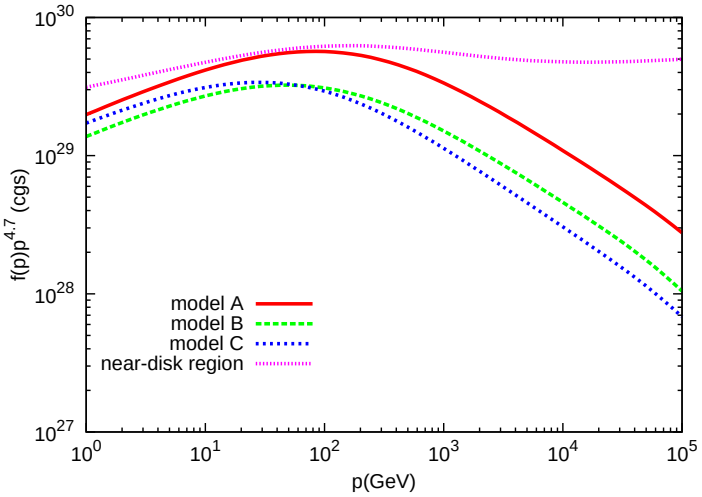

(a) CR spectrum for Model-A, Model-B, Model-C and for the model with the near-disk region.

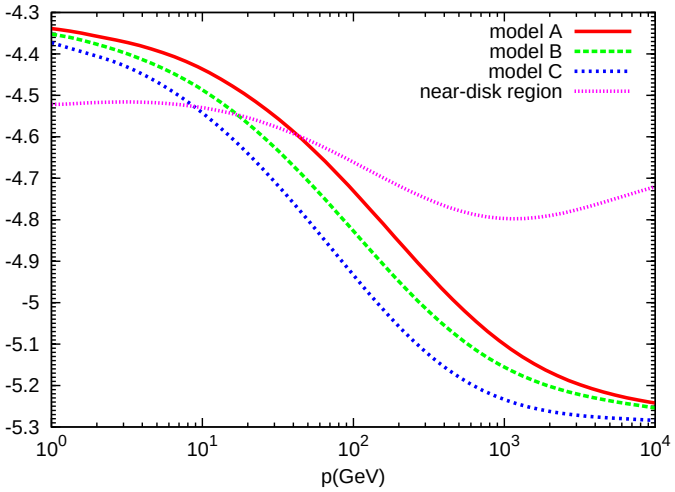

(b) Slope of the CR spectrum for Model-A, Model-B, Model-C and the model with the near-disk region.

Figure 4.5: Comparison of CR spectra and slope for models A, B and C and for the model which includes the near-disk region.

To summarize, we found that the CR spectral features in a CR-driven wind depend strongly on the wind parameters, and that imposing the observed CR pressure at z_0 (or imposing the matching with the observed spectrum at a specific energy) does not guarantee at all that the CR spectrum which solves the wind problem matches the observed one. For this reason it is frequent, in the CR-driven wind problem, to find winds which are compatible with the observational constraints on the input parameters but which lead to a spectrum totally different from the one observed.

The strong dependence of the CR spectrum on the wind parameters found in this work seems to conflict with previous results by Ptuskin et al. (1997), and deserves a deeper discussion. In their approach the authors considered the CR transport in a simplified wind model in which the CR advection velocity (dominated by the Alfvén speed) was assumed to scale linearly in z up to the area scale height $Z_b \sim 15$ kpc, and to be constant for $z > Z_b$. Because the advection velocity grows linearly in z, it will eventually reach a critical distance, $s_*(p)$, at which advection starts to dominate over diffusion (see Sec. 1.1.2). At this critical distance the CR advection time equals the diffusion time

$$\frac{s_*^2}{D(p)} \approx \frac{s_*}{U\,(s_*)} \;\Rightarrow\; s_*(p) \propto D(p)^{1/2}, \tag{4.1}$$

where we used the assumption of linear relation $U \sim \eta z$. Notice that, because the CR diffusion coefficient is a growing function of momentum, also $s_*(p)$ grows with momentum.

In the diffusion-dominated regime, namely when $z \lesssim s_*(p)$, the CR spectrum is expected to be approximately the one obtained in the standard diffusion model (see Sec. 1.1.1). Thus, we can approximate the CR diffusion flux at the disk as

$$D(p)\frac{\partial f}{\partial z}|_{z=0} \approx -Q_0(p)/2 \propto p^{-\gamma}, \tag{4.2}$$

and the equilibrium spectrum as

$$f(p) \sim \frac{Q_0(p)}{s_*(p)}\frac{s_*^2}{D(p)} \sim Q_0(p)\, D(p)^{-1/2}, \tag{4.3}$$

where we used Eq. 4.1.
Notice that Eq. 4.2 and 4.3 are similar to those in a leaky-box model, in which $f_0(p) \sim Q_0(p)H/D(p)$, but with a momentum dependent halo size $s_*(p)$, which replaces the preassigned halo size H.
Note that a momentum dependent halo size appears naturally in our CR-driven wind model as an output of the calculation. In contrast to what happens in standard CR propagation models, where the size of the halo has to be imposed by hand in order to guarantee the stationarity of the problem, the transport in a CR-driven wind does not require a preassigned halo size (see also Sec. 2.3).
Using Eq. 2.21 and 2.18 for the CR diffusion coefficient one can show that

$$\begin{aligned} D(p) &\propto p^{2\gamma-7} \\ f(p) &\sim p^{-2\gamma+7/2}. \end{aligned} \tag{4.4}$$

Hence, for injection $Q_0(p) \sim p^{-4.3}$ one infers an equilibrium spectrum $f_0(p) \sim p^{-5.1}$.

The problem with this argument put forward by Ptuskin et al. (1997), is that it is strictly valid only when the advection velocity vanishes at the base of the wind. In fact, Eq. 2.36 shows that Eq. 4.2, which holds in the diffusion dominated regime, is strictly valid only if the advection velocity is zero at the disk ($U(z_0) = 0$). In a real wind problem, as it as been shown in Chapter 3 and in the present chapter, this is evidently not the case. This is evident by looking for instance at Model-A: in Fig. 4.2(c) and 4.2(b) we show the critical distance $s_*(p)$ and the diffusion coefficient. One can see that the simple scaling $s_*(p) \propto D(p)^{1/2}$ is not satisfied. In addition, if the simple scalings of Eq. 4.4 were satisfied, we would have obtained a spectral slope of ~ 5.1 at CR momenta such that $s_*(p) < Z_b$. In Model-A $s_* \sim Z_b = 15$ kpc occurs at $p \sim 150$ GeV. However, as we can infer from Fig. 4.5(b), the spectral slope of Model-A is well below 5.1 at momenta below ~ 150 GeV.
At momenta larger than that for which $s_* = Z_b$, the authors assume the advection velocity to be constant. In this case the equilibrium spectrum is expected to be as $f_0(p) \sim Q_0(p)\pi R_d^2/(u_f s_*^2)$, while $s_* \propto D(p)$. Thus the

equilibrium spectrum would have a slope $-3\gamma+7$. This effect corresponds to a steepening of the spectrum at the transition momentum for which $s_* = Z_b$. This spectral softening is typical in the CR-driven wind model presented in this thesis, as it can be seen also for Model-A, Model-B and Model-C. For such reason it is not possible to reproduce the spectral hardening measured by PAMELA Adriani et al. (2011) and AMS-02 Aguilar et al. (2015). In Sec. 4.2 below we discuss a modified version of our wind model in which it is possible to account for this spectral hardening.

4.2 The importance of the near-disk region

In Sec. 4.1 we reported our analysis of the CR spectrum in a CR-driven wind by assuming that the wind is launched at the edge of the Galactic disk ($z_0 = 100$ pc). As discussed in the introduction to this chapter, this picture is justified by assuming that the neutral hydrogen in the ISM is mostly clumped in clouds with small filling factor, so that the generation of Alfvén waves is not strongly suppressed by ion-neutral damping (Kulsrud & Cesarsky (1971)). Is is worth recalling that, since plasma waves provide the coupling between CRs and background plasma, a strong wave damping would lead to a quenching of the wind.
However, as pointed out by Breitschwerdt et al. (1991), the picture could be different from the one proposed in Sec. 4.1, and the near-disk region may be plagued by severe ion-neutral damping (see Sec. 1.1.3). In this scenario, the wind is suppressed in this region, but may still be launched farther from the Galactic disk, where the density of the neutral component of the ISM is expected to largely decrease and the ion-neutral damping to become unimportant. For this reason Breitschwerdt et al. (1991) considered $z_0 = 1$ kpc as the wind base.
Notice that ion-neutral damping prevents CR diffusion even in the absence of winds. This was recognized in pioneering works on CR propagation (see e.g Skilling (1971); Holmes (1975)), where the near-disk region was assumed to be wave-free and the CR propagation in this region to be ballistic, while the ionized outer halo was considered as the actual diffusion region.
However, some type of turbulence may still be maintained in the near-disc region, perhaps due to SN explosions themselves. One could speculate that the waves may be considered to be isotropic there, so that the effective Alfvén speed vanishes.

Keeping in mind these considerations (see Recchia et al. (2016a)), here we illustrate a scenario for the wind launching that is different from the one presented in Sec. 4.1 and constructed as follows: the wind is assumed to be launched at a distance $z_0 = 1$ kpc from the disc and the near-disc region ($|z| < z_0$) is assumed to be characterized by a preassigned diffusion

coefficient, in the following form:

$$D(p) = 3 \times 10^{28} \left(\frac{p}{3 m_p c} \right)^{1/3} \ \mathrm{cm^2\,s^{-1}}, \tag{4.5}$$

and by an effective Alfvén velocity $v_A = 0$. At $z \geq z_0$, namely in the wind region, the diffusion coefficient is assumed to be purely self-generated as illustrated in Chapter 2.
From a technical point of view, the method of solution is the same described in Chapter 2, with the only difference that now, since the wind base is quite far from the Galactic disk, the CR pressure at the base of the wind differs from the one at the Sun location, which is imposed to equal the observed one as in Model-A of Sec. 4.1.
Notice that if U_0 is non-zero, there is always a particle momentum below which advection is more important than diffusion and the CR spectrum turns out to have roughly the same slope as the injection spectrum.
As we pointed out, here we assume the advection velocity to vanish in the near-disk region. However, in order to avoid discontinuities in the advection velocity at the boundary between the near-disk region and the wind region, we instead allow for both the wind velocity $u(z)$ and the Alfvén speed $v_A(z)$ to have a low z cutoff at $z < z_0$, so that both velocities drop to zero in a continuous manner in the near disc region. We checked that the details of such assumption do not have serious implications for the solution of the problem, provided that the velocity drops to zero fast enough inside the near-disc region. In order to appreciate the effect of the "near-disk" region, we consider a wind launched with the same parameters as Model-A of Sec. 4.1 at the wind base. In Fig. 4.6(b) and Fig. 4.6(a), we show the wind density and temperature and the wind velocity (together with the Alfvén and sound speed) respectively. Of course, those profiles are limited to the wind region $z \geq z_0 = 1$ kpc. As for Model-A, B and C of Sec. 4.1, the advection velocity is dominated by the Alfvén speed at the wind base. The wind is launched with $u_0 = 15$ km/s and becomes sonic at $z_c \sim 40$ kpc. The Alfvén speed at the wind base is $v_{A0} = 79$ km/s.
In Fig. 4.6(c), we show the CR and gas pressures. The gas pressure is limited to the wind region while the CR pressure extends down to the disk region. Here we also plotted the CR pressure as derived from the hydrodynamic calculation in the wind region, which, with good accuracy, overlaps with the one derived from the kinetic calculation. In the same plot we also show the wave pressure as derived from the kinetic calculation.
The injection spectrum has been normalized in order to get the observed CR pressure at the disk. For these reason we are bound to take

$$\frac{\xi_{CR}}{0.1} \frac{\mathcal{R}_{SN}}{1/30\,\mathrm{yr^{-1}}} \approx 0.8. \tag{4.6}$$

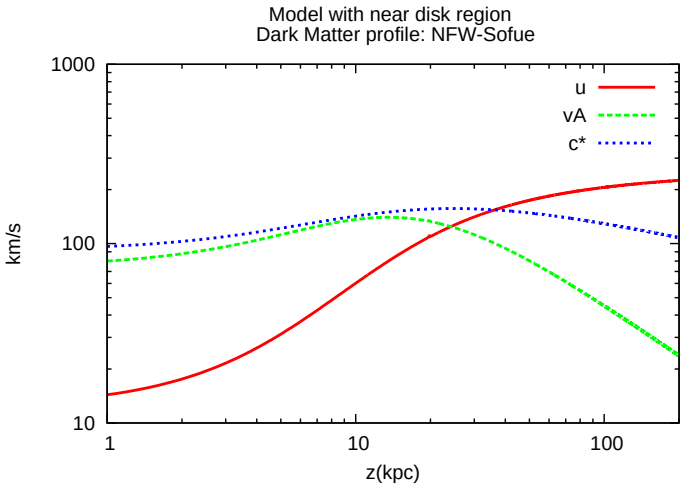

(a) Wind velocity, Alfvén velocity and sound speed.

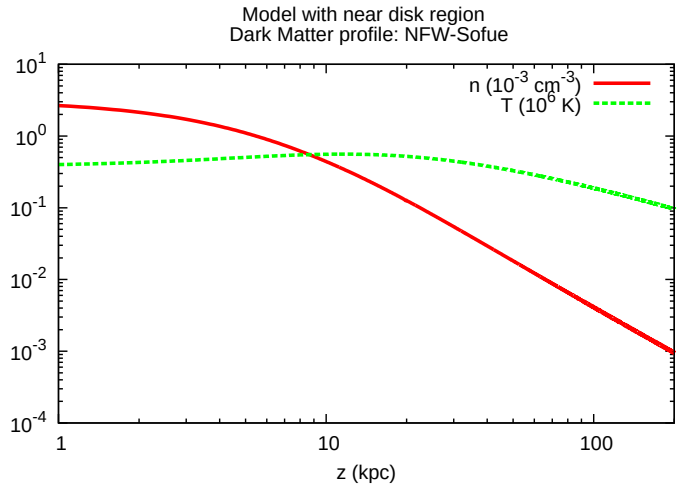

(b) Density in units of 10^{-3}cm^{-3} and temperature in units of 10^6 K.

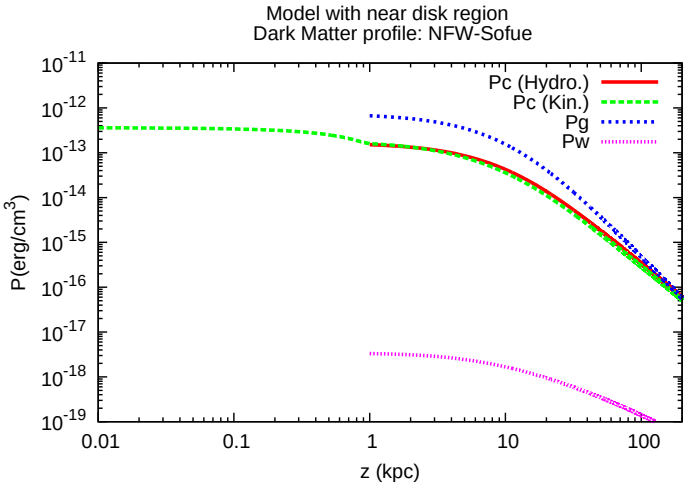

(c) Gas pressure, CR pressure obtained from the hydrodynamic and kinetic calculations, wave pressure obtained from the CR transport equation.

Figure 4.6: Results for the model which includes a near-disk region. Different panels show: a) wind, Alfvén and compound sound speed; b) gas density and temperature; c) gas and CR pressure.

In Fig. 4.5(a) and 4.5(b), we compare the CR spectrum at the disk and the corresponding spectral slope as obtained for this wind model, together with those of Model-A, B and C. One can immediately see the huge effect of the near-disk region on the CR spectrum at Earth: at low energies (below ~ 10 GeV) the CR spectrum is mainly affected by advection, while in the range $10\,\mathrm{GeV} \lesssim \mathrm{E} \lesssim 1000$ GeV it is mainly affected by the self-generation of waves in the wind region. At energies higher than ~ 1 TeV the spectrum hardens. The flat spectrum at low energies and the progressive steepening up to ~ 1 TeV is typical of non-linear CR propagation models (see e.g Aloisio et al. (2015)), and was also found in our wind model (see Sec. 4.1). This spectral behavior is due to the effect of advection (at low energies) and to the fast energy dependence of the self-generated diffusion coefficient. The spectral hardening at ~ 1 TeV is due to the Kolmogorov turbulence (Eq. 4.5) assumed in the near disc region. And in fact, the spectral slope becomes 4.3(injection) + 1/3(Kolmogorov) $\simeq 4.63$ at $E \gtrsim 1$ TeV. This hardening is qualitatively similar to the one found by Tomassetti (2012) in a simple two zone model of the Galactic halo.
The important point to remark here is that the CR spectrum above ~ 1 TeV is mainly affected by the nar-disk region, while below ~ 1 TeV, it is mainly affected by what happens in the wind region, i.e is determined by the interplay between the advection with the self-generated Alfvén waves and with the wind and the diffusion on the self-generated turbulence, as illustrated in this thesis. Thus, the transport properties of the bulk of CRs are not preassigned in this approach.
To conclude, notice that the qualitative behavior at high energy of the spectrum presented here resembles the spectral hardening measured by PAMELA (Adriani et al. (2011)) and AMS-02 (Aguilar et al. (2015)). We did not try to fit the data because our main goal is to show the qualitative effect of diffusion in the near-disk region.

4.3 Comparing the model with observations: the effect of the Dark Matter halo

In the present chapter and in Chapter 3 we illustrated how, in a CR-driven wind model, both the wind properties and the CR spectrum depend on the launching parameters. We performed our analysis by taking into account the observational constraints on the parameters at the Sun position, as described in Sec. 3.2. In Sec. 3.3 we also considered the effect of the DM halo (see Sec. 3.1) on the wind profile.

Here we present a wind model whose parameters are compatible with properties of the Galactic halo derived in Miller & Bregman (2015), i.e Model-C of Sec. 4.1, and to study how the CR spectrum depends on the

DM halo profile. In particular, we show that it is possible to have a good agreement with the observed CR spectrum, depending on the choice of the DM halo potential.

We already mentioned the work of Miller & Bregman (2015) in Sec. 3.2. Here we report a more detailed description of their results. A hot gaseous halo has been detected in the Milky Way through Oxygen absorption lines in quasar spectra and emission lines from blank-sky, measured by XMM-Newton/EPIC-MOS. Constraints on the structure of the hot gas halo are given by fitting a radial model,

$$n(r) \approx \frac{n_0 r_c^{3\beta}}{r^{3\beta}}, \tag{4.7}$$

for the halo density distribution and a constant-density model for the Local Bubble, from which the expected emission, to compare with observations, is computed.

Here $r = \sqrt{R^2 + z^2}$, where R is the Galactocentric distance and z the distance from the Galactic disk. The best fit parameters for the halo density given in Miller & Bregman (2015) are $\beta = 0.5 \pm 0.3$ and $n_0 r_c^{3\beta} = 1.35 \pm 0.24$ $\mathrm{cm}^{-3}\mathrm{kpc}^{3\beta}$. The authors also infer a nearly constant halo temperature of $\sim 2 \times 10^6$ K and a sub-solar gas metallicity that decreases with r, but that also must be $\gtrsim 0.3 Z_\odot$ to be consistent with the pulsar dispersion measure toward the Large Magellanic Cloud.

This halo model implies a gas density of $3 - 6 \times 10^{-3}$ cm^{-3} in the vicinity of the Sun, a density scaling with z that reads $n(z) \sim z^{-1.5}$, and a halo mass of $M(< 50\mathrm{kpc}) = (3.8 \pm 0.3) \times 10^9\,\mathrm{M}_\odot$ and $M(< 250\mathrm{kpc}) = (4.3 \pm 0.8) \times 10^{10}\,\mathrm{M}_\odot$. Notice that this coronal gas could be in fact the result of Galactic winds and that such halo mass accounts for $\lesssim 50\%$ of the Milky Way missing baryons.

The Model-C wind, which we considered in Sec. 4.1 and we use also in the present analysis, has the following parameter values: gas density $n_0 = 0.006$ cm^{-3}, gas temperature $T_0 = 2 \times 10^6$ K, expansion index of the area $\alpha = 1.5$, area scale height $Z_b = 15$ kpc, magnetic field $B_0 = 1\,\mu$G and wind base close to the Galactic disk, at $z_0 = 100$ pc. The CR injection is normalized in order to match the observed CR spectrum at 50 GeV. In Fig. 4.7(c) we show the wind density and temperature obtained with these input parameters and for the three DM halos NFW-Sofue, BUR and INN (see Sec. 3.1). The NFW-Salucci model is missing since with such halo no wind was launched. In Fig. 4.7(a) and 4.7(b) we show the corresponding wind speed, sound speed and Alfvén velocity, while in Fig. 4.7(d) we show the gas and CR pressures.

For all the three DM models, the wind is launched as sub-Alfvénic with: ($u_0 = 2\,\mathrm{km/s}$, $\mathrm{z_c} = 60\mathrm{kpc}$, $\mathrm{u_f} = 450\mathrm{km/s}$) for the NFW-Sofue profile, ($u_0 = 3\,\mathrm{km/s}$, $\mathrm{z_c} = 285\mathrm{kpc}$, $\mathrm{u_f} = 273\mathrm{km/s}$) for the BUR profile and ($u_0 = 5\,\mathrm{km/s}$, $\mathrm{z_c} = 339\mathrm{kpc}$, $\mathrm{u_f} = 209\mathrm{km/s}$) for the INN profile.

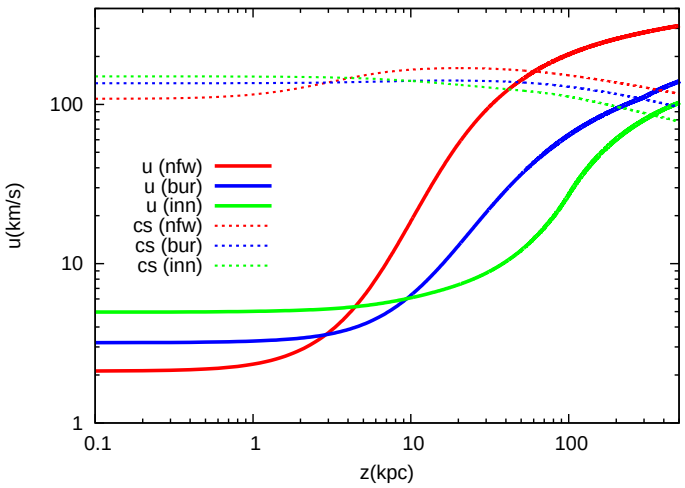

(a) Wind and compound sound speed.

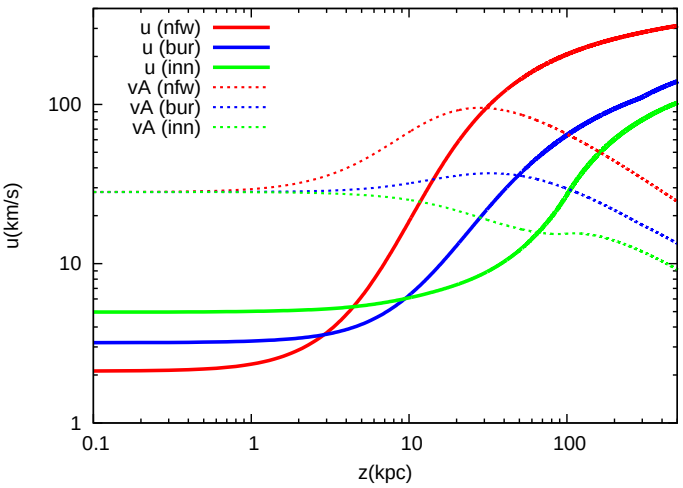

(b) Wind and Alfvén speed.

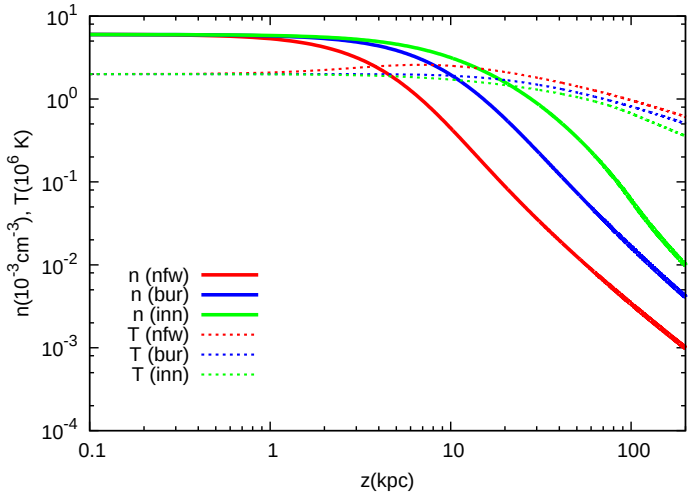

(c) Gas density and temperature.

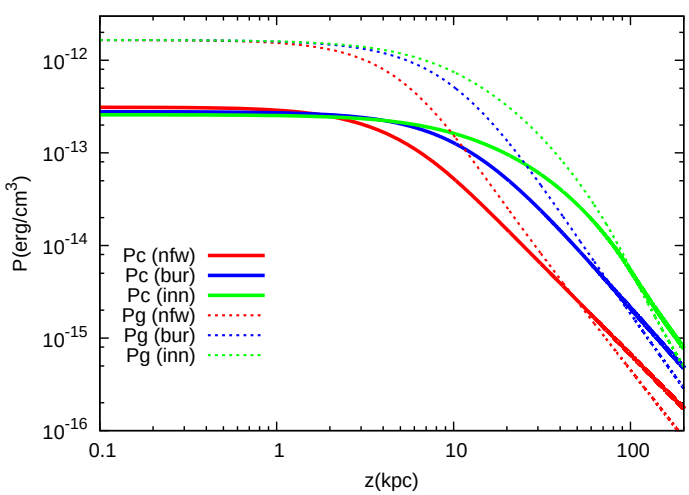

(d) Gas and CR pressure.

Figure 4.7: Dependence of the CR spectrum on the DM halo: a) wind and compound sound speed; b) wind and Alfvén speed; c) gas density and temperature; d) gas and CR pressure.

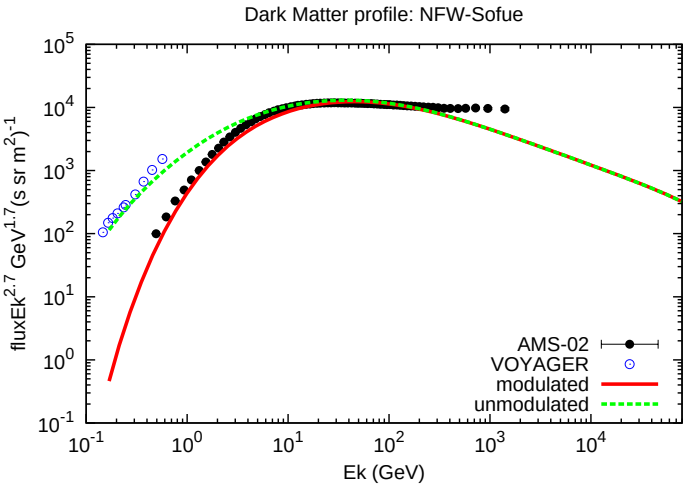

(a) CR spectrum with the NFW halo.

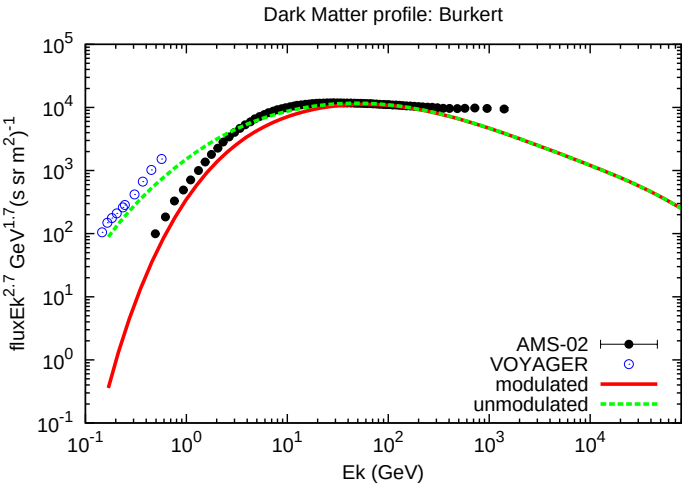

(b) CR spectrum with the BUR halo.

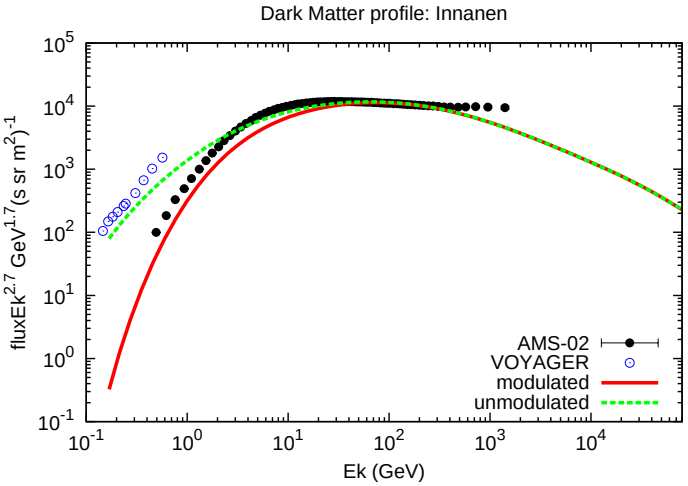

(c) CR spectrum with the INN halo.

Figure 4.8: Dependence of the CR spectrum on the DM halo: a) CR spectrum with the NFW halo; b) CR spectrum with the BUR halo; c) CR spectrum with the INN halo.

The effect of the DM halo model on the wind properties has been discussed in Sec. 3.3.3 and those considerations are still valid: the NFW-Sofue profile, having a larger gravitational force compared to the other two models, shows the smallest launching velocity, the larger terminal velocity and the steepest velocity profile (as it can be seen in Fig. 4.7(a)). Due to the mass and momentum conservation, the rapid increase of the wind velocity, which starts at smaller z and with a steeper profile for the NFW-Sofue, corresponds to the rapid decrease of the gas density and of the CR and gas pressure (see Fig. 4.7(c) and Fig. 4.7(d)). In the range $z \sim 1 - 100$ kpc, the NFW-Sofue profile shows the largest Alfvén speed (due to the smaller gas density), and the smallest CR pressure. However the first is still dominant, leading to a larger heating due to wave damping (recall that the heating term is $\sim v_A \nabla P_c$), and hence to a slightly larger temperature (see Fig. 4.7(c)) compared to the BUR and INN halos.
Notice that the effect of wave damping is in fact to keep the gas temperature around 2×10^6 K up to ~ 100 kpc (this is especially true for the NFW-Sofue profile), in line with the results of Miller & Bregman (2015) on the galactic halo.
In Fig. 4.8, we show the CR spectrum for the NFW-Sofue, BUR and INN profile respectively. Below ~ 200 GeV, the best matching with the observed spectrum is achieved with the NFW-Sofue model. The larger wind velocity of the BUR and INN models leads to a low energy spectrum harder than the observed one. As we illustrated in Sec. 4.2, the spectral hardening at ~ 200 GeV cannot be obtained in our wind model, unless we include, for instance, some preexisting turbulence.

Chapter 5

The radial distribution of Galactic Cosmic Rays

In this thesis we have shown that CR propagation is strongly influenced by the properties of the ISM and by the action that CRs themselves exert on the environment. This surely happens in a CR-driven wind problem, but it remains true also in the absence of winds. For instance, the Alfvén speed depends on both the magnetic field and the density of the background plasma. The properties of the ISM and the CR source distribution depend on the location in the Galaxy, in particular on the Galactocentric distance. Thus it is not surprising that the CR distribution in the Galaxy also exhibits a radial dependence.
The CR distribution in the Galaxy can be tracked using the diffuse γ-ray emission from the Galactic disc and shows interesting features. At Galactocentric distances $R \gtrsim 10$ kpc (i.e in the outer region of the Galaxy) the CR distribution is flatter than the radial distribution of the supernova remnants, the alleged sources of the bulk of CRs. The latter is modeled using the pulsar and SN catalogs. This result, known as the "radial gradient problem", was obtained for the first time from the analysis of the γ-ray emissivity in the Galactic disk derived from the SAS-2 data by Stecker & Jones (1977) and later from the analysis of the COS-B data by Bhat et al. (1986) and Bloemen et al. (1986), then confirmed by work based on EGRET data (Hunter et al. (1997); Strong & Mattox (1996)) and, more recently by data collected by *Fermi*-LAT (Ackermann et al. (2011); Ackermann et al. (2012)).
However, a recent analysis, published in two independent papers by Acero et al. (2016) and Yang et al. (2016), of *Fermi*-LAT data accumulated over seven years, including also the inner part of the Galaxy, shows a more complex situation: while in the outer Galaxy the flatness of the CR gradient has been confirmed, the density of CR protons in the inner Galaxy turns out to be appreciably higher than in the outer regions of the disk, showing a peak in the region $\sim 2 - 5$ kpc. In addition, the decrease in the CR density with

increasing Galactocentric distance seems to be accompanied by a softening of the CR spectrum, with a slope ranging from 2.5-2.6, at a distance of ~ 3 kpc, to 2.8-2.9 in the external regions. These results concern CRs that are responsible for the production of γ-rays of energy ~ 2 GeV, namely protons with energy of order ~ 20 GeV.
These are very interesting results, however it is worth keeping in mind that the spatial distribution of CRs in the Galaxy is not the result of a direct measurement, since it can only be inferred from the observed γ-ray emission through a careful modeling of the spatial distribution of the gas that acts as target for nuclear collisions and by separating the γ-ray contribution due to hadrons from that due to leptonic interactions (bremsstrahalung and inverse Compton scattering).

It is difficult to account for this scenario in the framework of the standard approach to CR propagation, in which the CR propagation properties are assumed to be the same in the whole Galaxy (see e.g Berezinskii et al. (1990)). Several ideas have been explored within this approach in order to solve the radial gradient problem. To mention few of them: a) assuming a larger halo size or b) a flatter distribution of sources in the outer Galaxy Ackermann et al. (2011); c) take into account advection effects due to the presence of Galactic winds Bloemen et al. (1986); d) assuming a sharp rise of the CO-to-H_2 ratio in the external Galaxy Strong et al. (2004); e) speculating on a possible radial dependence of the injected spectrum Erlykin et al. (2016).
None of these proposals, taken individually, can simultaneously account for both the spatial gradient and the spectral behavior of CR protons. Moreover, many of them have issues in accounting for other observables (see for instance the discussion in Evoli et al. (2012)).

A different approach is to relax the hypothesis of a spatially constant diffusion coefficient. This was done for instance in Gaggero et al. (2015a) and Gaggero et al. (2015b), where it was shown that a phenomenological scenario in which both the CR advection and diffusion depend on the position in the Galaxy can explain the CR radial gradient. Similarly, Evoli et al. (2012) proposed a correlation between the diffusion coefficient parallel to the Galactic plane and the source density in order to account for both the CR density gradient and the small observed CR anisotropy. The problem of these approaches is the lack of a physical motivation to justify the assumed spatial dependence of the CR transport properties.

Here we try to explain the CR radial distribution considering two possible scenarios.

In the first one (see also Recchia et al. (2016b)), we examine a simplified version of the propagation model explored so far in the thesis, where Galactic winds are not taken into account and the Alfvén velocity is considered independent on z. The CR propagation is assumed to take place due to scattering on the self-generated Alfvén waves and due to advection with these waves. Recall that, as we have seen in Chapter 4, the observed CR spectrum below $\sim$ 200 GeV may be dominated by the effects of self generation, and by advection near the disk which is mostly due to Alfvén waves. In fact, it has been shown that the CR spectrum below $\sim$ 200 GeV can be explained in a scenario in which both diffusion and advection are due to self-generated waves (see Aloisio & Blasi (2013); Blasi et al. (2012)).
In the second approach we consider also the possible presence of Galactic winds and we use the model presented in the thesis.

We apply both these propagation models everywhere in the Galaxy, in the assumption that the spatial distribution of SNRs traces the Galactic CR sources and we compare our results with the two analyses of Acero et al. (2016) and Yang et al. (2016). Notice however that, as we will show in what follows, the two analyses give somewhat different results: in Acero et al. (2016), the CR distribution is peaked at $\sim$ 3 kpc, while in Yang et al. (2016) the it is peaked at $\sim$ 5 kpc and the peak is less pronounced. Moreover, in Yang et al. (2016) the CR spectrum is harder, with a slope of 0.1-0.2 smaller than in Acero et al. (2016). In spite of the differences, the qualitative behavior of the two analyses is very similar.
With the first scenario (see Sec. 5.1) we find that, for a realistic distribution of CR sources and for reasonable assumptions on the spatial dependence of the magnetic field on the Galactocentric distance, both the observed spatial profile of the CR density and the spectral behavior are well reproduced, in particular those reported in Acero et al. (2016). The second scenario (see Sec. 5.2) is more complicated because we find that in the outer Galaxy ($R \gtrsim 10$ kpc) the wind is not launched, hence it is difficult to explain the data in a fully consistent picture. For $R \lesssim 10$ kpc, the possibility to launch winds and the wind properties strongly depends on the DM halo model. In addition, the presence of winds leads to a less peaked CR in the inner Galaxy (compared to the model without winds), and, in general, to a better agreement with the analysis of Yang et al. (2016) than with that of Acero et al. (2016).

5.1 The CR transport model without winds

The first scenario we want to explore is a simplified version of the transport model presented in this thesis, in which the CR diffusion and advection are both due only to self-generated Alfvén waves without the presence of

any wind. Also in this case, we adopt a one-dimensional transport model, in which, at every Galactocentric distance R, the CR particles advect and diffuse only along z, i.e there is no diffusion along the Galactic plane. In addition, we assume that the Alfvén speed is constant in z and directed out of the Galactic disk.
With these assumptions, the CR transport equation 2.17 becomes

$$-\frac{\partial}{\partial z}\left[D(z,p)\frac{\partial f}{\partial z}\right]+w\frac{\partial f}{\partial z}-\frac{p}{3}\frac{\partial w}{\partial z}\frac{\partial f}{\partial p}=Q_0(p)\delta(z)\,, \tag{5.1}$$

where the advection velocity is

$$w(z)=\mathrm{sign}(z)\,v_A. \tag{5.2}$$

As in Sec. 2.3, the injection of particles occurs only in the Galactic disk (at $z=0$) and is a power law in momentum (see Eq. 2.28 and Eq. 2.29):

$$Q_0(p)=\frac{\xi_{\rm inj}E_{\rm SN}\mathcal{R}_{\rm SN}(R)}{4\pi\Lambda c(m_pc)^4}\left(\frac{p}{m_pc}\right)^{-\gamma}. \tag{5.3}$$

Notice that the SN rate, $\mathcal{R}_{\rm SN}$, is a function of the Galactocentric distance.

The self-generated wave spectrum, as in our wind model, is determined by equating the growth rate of waves due to CR streaming instability, Eq. 2.20, and the damping rate due to NLLD, Eq. 2.19. The resulting equilibrium wave spectrum reads

$$\mathcal{F}(k)=(2c_k)^3\left[\frac{16\pi^2p^4}{B_0^2}\,D\frac{\partial f}{\partial z}\right]^2. \tag{5.4}$$

This expression holds since damping is much faster than wave advection at the Alfvén speed.
The diffusion coefficient is thus calculated, using the quasi-linear theory (valid for weak magnetic perturbations $\delta B \ll B_0$), Eq. 2.18.

A technique to solve the transport equation 5.1 is the same used in Sec. 2.3, i.e to integrate between 0^- and 0^+ (around the disk) and between 0^+ and z, with the boundary conditions $f(0,p)=f_0(p)$ and $f(H,z)=0$.
Notice however that, in contrast to what happens in the wind model, in which H is only set for numerical purposes and can in principle be located at spatial infinity, here the halo size has to be imposed by hand, in order to guarantee the stationarity of the transport problem. The halo size plays a crucial role in standard CR propagation model (see Sec. 1.1.1), while it becomes an output of the calculation in the wind problem.

With the simplifying assumption on the advection velocity, Eq. 2.41 for the CR distribution function $f(z,p)$ becomes (see also Sec. 1.1.1):

$$f(z,p) = f_0(p)\,\frac{1-e^{-\xi(z,p)}}{1-e^{-\xi(0,p)}}\,, \tag{5.5}$$

where $\xi(z,p) = \int_z^H v_A/D(z',p)dz'$ and the distribution function at the disk is:

$$f_0(p) = \int_p^{p_{\rm max}} \frac{dp'}{p'}\,\frac{3Q_0(p')}{2v_A}\,\exp\left[-\int_p^{p'}\left(\frac{d\hat{p}}{\hat{p}}\frac{3}{e^{\xi(0,\hat{p})}-1}\right)\right]\,. \tag{5.6}$$

Interestingly, the diffusion coefficient can be expressed in a compact form using the diffusive flux, $D\partial f/\partial z$, computed from Eq. 5.5 into Eq. 5.4. The expression for the CR diffusion coefficient becomes:

$$D(z,p) = D_{\rm H}(p) + 2v_A\,(H-z)\,, \tag{5.7}$$

where $D_{\rm H}(p)$ is the diffusion coefficient at $z=H$ and reads:

$$D_{\rm H}(p) = \frac{D_B}{(2c_k)^3}\left[\frac{B_0^2}{16\pi^2p^4}\frac{1-e^{-\xi(0,p)}}{v_A f_0(p)}\right]^2\,. \tag{5.8}$$

It follows that the diffusion coefficient is maximum at $z=0$ and decreases linearly with z.

Eq. 5.5-5.6 and Eq. 5.7-5.8, can be recast in an explicit form in the two opposite limits of diffusion-dominated and advection-dominated transport. In the diffusion dominated regime (i.e. when $v_A H \ll D_{\rm H}$) the diffusive solution is recovered. In fact, in this limit $e^{-\xi(0,p)} \approx 1 - v_A H/D_H$ and we get the well known expressions (see Sec. 1.1.1)

$$\begin{aligned} f(z,p) &= f_0(p)\left[1-\frac{z}{H}\right] \\ f_0(p) &= Q_0\frac{H}{2\,D_H}. \end{aligned} \tag{5.9}$$

In addition, the diffusion coefficient becomes constant in z, i.e

$$D(z,p) \to D_{\rm H}(p) \to D_B^{\frac{1}{3}}\frac{1}{2c_k}\left[\frac{B_0^2 H}{16\pi^2p^4 f_0(p)}\right]^{\frac{2}{3}}\,. \tag{5.10}$$

Replacing f_0 (Eq. 5.9) into Eq. 5.10, we finally obtain

$$D_{\rm H}(p) = D_B\frac{1}{(2c_k)^3}\left[\frac{2B_0^2}{16\pi^2p^4Q_0}\right]^2 \propto p^{2\gamma-7} \tag{5.11}$$

$$f_0(p) = \frac{Q_0}{2}\frac{H}{D_H} = \frac{3c_k^3}{r_L v}\left(\frac{16\pi^2p^4}{B_0^2}\right)^2 HQ_0(p)^3 \propto p^{7-3\gamma}. \tag{5.12}$$

In the opposite regime, i.e when $v_A H \gg D_{\rm H}$, we have that $e^{-\xi} \approx 0$, so that $f(z,p) \to f_0(p)$ and from Eq. 5.6 we recover:

$$f_0(p) = \frac{3Q_0(p)}{2v_A\,\gamma}. \tag{5.13}$$

On the other hand, we see from Eq. 5.7 that the diffusion coefficient in the disk behaves like a constant in momentum, namely $D(z=0,p) \to 2v_A H$. This happen because at small p, $\mathcal{F} \to D_B/(2v_A H)$, so that $D = D_B/\mathcal{F} \to 2v_A H$. Clearly this dependence is restricted to the momenta for which diffusion becomes slower than advection, typically below ~ 10 GeV/c (see below). We refer to this regime as advection dominated regime, although particles never reach a fully advection dominated transport because diffusion and advection times are of the same order.

The numerical solution to the transport problem illustrated so far can be obtained with the same technique described in Sec. 2.3: we start by choosing a guess function for $D_H(p)$ (for instance the expression (Eq. 5.12) obtained without advection) and then we iterate until convergence is reached, a procedure which usually requires only few iterations.

Here we are interested in exploring the dependence of the CR spectrum on the Galactocentric distance, which enters the calculation through the SN rate in the injection spectrum and through the magnetic field strength and the gas density (which determine v_A). In order to minimize the number of parameters that enter the calculation, we assume that the gas density is constant in the whole propagation volume, while the magnetic field strength depends on R but not on z, so that v_A is independent from z.
Notice that, comparing Eq. 5.12 and 5.13, we see that the CR spectrum has the following scalings with the two quantities depending on R:

$$\begin{aligned} &f_0(p) \propto (Q_0/B_0)^3 \qquad \text{(diffusive regime)} \\ &f_0(p) \propto Q_0/B_0 \qquad \text{(advective regime).} \end{aligned} \tag{5.14}$$

This dependence is the key feature of this scenario that allows one to get the spatial dependence of CRs similar to the observed one.

5.1.1 Fitting the CR spectrum at the solar position

Here, we analyze the radial dependence of the magnetic field and of SNRs and we illustrate our results on the corresponding radial dependence of the CR spectrum. Following most of the current literature, we assumed a halo size of $H = 4$ kpc.
The gas density, magnetic field and SN rate can be chosen in order to reproduce the proton CR spectrum observed at Earth. Here we consider two

different sets of parameters, named Model-1 and Model-2, in which we fix the gas density to two different values, corresponding to the density of the warm ionized and hot ionized gas components of the ISM respectively (see Ferrière (2001)). In addition, the CR injection slope has been chosen in order achieve a good agreement with the observed CR spectrum below ~ 100 GeV and it is different for the two models.
In Model-1, following Blasi et al. (2012) and Aloisio & Blasi (2013), we fix the gas density to $n = 0.02$ cm^{-3} (a value consistent with the density of the warm ionized gas component (Ferrière (2001))) and we adopt an injection slope $\gamma = 4.2$ in the whole propagation volume, while we assume $B_0 = 1\,\mu$G at the Sun position (see Sec. 3.2). The same set of parameters was also used by Recchia et al. (2016b). Notice that these two parameters also fix the value of the Alfvén speed (~ 15 km/s) at the Sun location. This is very important since, as we have shown also in the wind model (see Chapter 4), the interplay between advection and diffusion determines the CR distribution function, once given the injection spectrum and the product of injection efficiency times the local SN explosion rate, $\xi_{\rm inj} \times \mathcal{R}_{\rm SN}(R_\odot)$. By requiring that the local CR spectrum at ~ 50 GeV is equal to the observed one, we get $\xi_{\rm inj}/0.1 \times \mathcal{R}_{\rm SN}/(1/30\,{\rm yr}) = 0.29$. Notice that these values lead to a good agreement with the observed CR spectrum below ~ 100 GeV (see e.g Aloisio & Blasi (2013).
In Model-2 we fix the gas density to $n = 0.006$ cm^{-3} and we adopt an injection slope $\gamma = 4.3$, while we assume $B_0 = 1\,\mu$G at the Sun position (so $v_A \sim 28$ km/s). By requiring that the local CR spectrum at ~ 50 GeV is equal to the observed one, we get $\xi_{\rm inj}/0.1 \times \mathcal{R}_{\rm SN}/(1/30\,{\rm yr}) = 0.36$, and also in this case we obtain a quite good agreement with the observed CR spectrum below ~ 100 GeV.

Since here we are interested only to CRs that are responsible for the production of γ-rays of energy ~ 2 GeV, as observed by *Fermi*-LAT , namely protons with energy of order ~ 20 GeV, we can safely ignore the issues related to the CR spectral hardening at ~ 200 GeV (see Sec. 4.2; Blasi et al. (2012); Aloisio & Blasi (2013); Aloisio et al. (2015); Tomassetti (2012)).

Notice that in Model-C, proposed in Chapter 4, where we assumed the same gas density, magnetic field and injection slope of Model-2, we also achieved a good agreement with the observed spectrum by taking $\xi_{\rm inj} \times \mathcal{R}_{\rm SN}(R_\odot) = 0.32$. The difference in $\xi_{\rm inj} \times \mathcal{R}_{\rm SN}(R_\odot)$ compared to Model-2 is due to the presence of the wind.

5.1.2 The radial dependence of the CR spectrum

The SNR distribution is usually inferred based on two possible tracers: radio SNRs and pulsars. Here we adopt the distribution of SNRs recently obtained

by Green (2015) from the analysis of bright radio SNRs. The author used a cylindrical model for the Galactic surface density of SNRs as a function of the Galactocentric radius, in the form:

$$f_{\rm SNR} \propto \left(\frac{R}{R_\odot}\right)^{\alpha} \exp\left(-\beta \frac{R - R_\odot}{R_\odot}\right) , \tag{5.15}$$

where the position of the Sun is assumed to be at $R_\odot = 8.5$ kpc. For the best fit Green (2015) obtained $\alpha = 1.09$ and $\beta = 3.87$, so that the distribution is peaked at $R = 2.4$ kpc. However, as noted by Green (2015), it is worth keeping in mind that the best-fitting model is not very well defined, since there is some level of degeneracy between the parameters α and β.

Case & Bhattacharya (1998) also adopted the fitting function Eq. 5.15 but obtained their best fit for $\alpha = 2.0$ and $\beta = 3.53$, resulting in a distribution peaked at $R = 4.8$ kpc and broader for larger values of R with respect to the one of Green (2015). Case & Bhattacharya (1998) estimated the source distances using the so called 'Σ–D' relation, that is well known to be affected by large uncertainties. Moreover Green (2015) argued that the Σ–D used by Case & Bhattacharya (1998) appears to have been derived incorrectly.

An important caveat is that the SNR distribution derived in the literature is poorly constrained for large galactocentric radii. For instance Green (2015) used a sample of 69 bright SNRs but only two of them are located at galactic latitude $l > 160°$. Similarly, Case & Bhattacharya (1998) used a larger sample with 198 SNRs, but only 7 of them are located at $R > 13$ kpc and there are no sources beyond 16 kpc.

The distribution of pulsars is also expected to trace that of SNRs after taking into account the effect of the birth kick velocity, that can reach ~ 500 km/s. These corrections are all but trivial (see e.g Faucher-Giguère & Kaspi (2006)), hence in what follows we adopt the spatial distribution as inferred by Green (2015).

The other magnitude needed for our calculation is the radial dependence of the magnetic field strength, $B_0(R)$. Here we assume the model described in Sec. 3.2, i.e

$$\begin{aligned} B_0(R < 5\,{\rm kpc}) &= B_\odot R_\odot / 5\,{\rm kpc} \\ B_0(R > 5\,{\rm kpc}) &= B_\odot R_\odot / R\,, \end{aligned} \tag{5.16}$$

where the normalization is fixed at the Sun position with $B_\odot = 1\mu$G. Using this prescription we calculate the CR spectrum as a function of the Galactocentric distance, as discussed in Sec. 5.1. In Fig. 5.1 we show the density of CRs with energy $\gtrsim 20$ GeV, for Model-1 and Model-2, compared to the same quantity as derived from *Fermi*-LAT data. In both cases our results are in remarkably good agreement with data, at least out to a distance of ~ 10 kpc.

Notice also that Model-1 reproduces well the peak in the CR distribution function of Acero et al. (2016), while Model-2 is in better agreement with Yang et al. (2016).
At larger distances, our predicted CR density drops faster than the one inferred from data, thereby flagging again the well known CR gradient problem. In fact, the non-linear theory of CR propagation, in its most basic form (in Fig. 5.1, the curves related to B $\sim$ 1/R) makes the problem even more severe: where there are more CR sources, the diffusion coefficient is reduced and CRs are trapped more easily, but where the density of sources is smaller the corresponding diffusion coefficient is larger and the CR density drops. A similar situation can be seen in the trend of the spectral slope as a function of R, plotted in Fig. 5.2. In both Model-1 and Model-2 with B $\sim$ 1/R, our predicted line reproduces well the slope reported in Acero et al. (2016) out to a distance of $\sim$ 10 kpc. Notice that the slopes of Model-1 and Model-2 are practically overlapped below $\sim 5-6$ kpc, despite the different v_A and injection slope of the two models. This is the result of the non-linearity of the problem: from the one hand we expect that for Model-2, which has the largest v_A, advection dominates over diffusion up to larger momenta compared to Model-1, leading to generally harder spectra. On the other hand, the importance of this effect is reduced due to the fact that the smaller CR density in the inner Galaxy of Model-2 (see Fig. 5.1) leads to larger diffusion coefficients (see Fig. 5.3 and Fig. 5.4) compared to Model-1. Moreover, it has to be taken into account the different injection slope of the two models. In the region R $\sim$ 6-10 kpc, the CR density is practically the same for both models. Here the larger advection in Model-2 makes the spectrum slightly harder than in Model-1, despite the steeper injection of Model-2.

In the outer region the predicted spectrum is steeper than observed. It is important to understand the physical motivation for such trend: at intermediate values of R, where there is a peak in the source density, the diffusion coefficient is smaller and the momenta for which advection dominates on diffusion is higher. This implies that the equilibrium CR spectrum is closer to the injection spectrum, $Q(p)$ (harder spectrum). On the other hand, for very small and for large values of R, the smaller source density implies a larger diffusion coefficient and a correspondingly lower momentum where advection dominates on diffusion. As a consequence the spectrum is steeper, namely closer to $Q(p)/D(p)$. In fact, at distances $R \gtrsim 15$ kpc, the spectrum reaches the full diffusive regime, i.e $f_0 \sim p^{7-3\gamma}$, which gives $f_0 \sim p^{-5.6}$ for Model-1 and $f_0 \sim p^{-5.9}$ for Model-2 (meaning that the slope in Fig. 5.2 is 3.6 for Model-1 and 3.9 for Model-2).

As pointed out in Sec. 5.1, the non-linear propagation is quite sensitive to the radial dependence of the magnetic field on R.

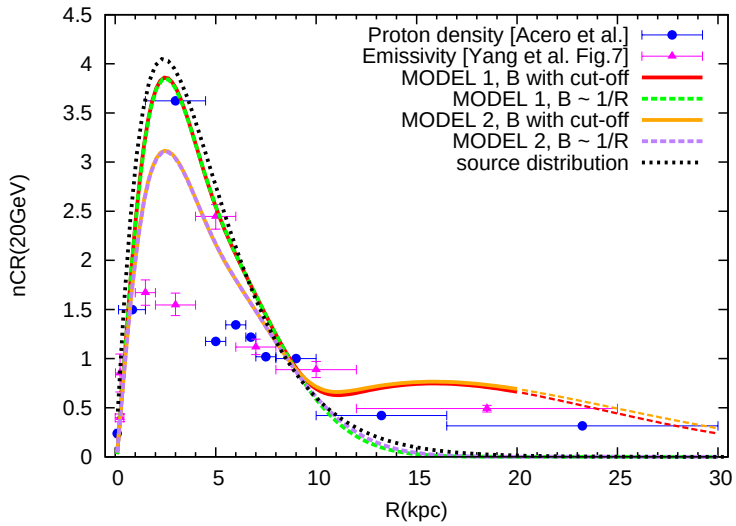

Figure 5.1: CR density at $E > 20$ GeV from Acero et al. (2016) and Yang et al. (2016) as a function of the Galactocentric distance, as labelled. Our predicted CR density at $E > 20$ GeV for Model-1 and Model-2 are shown. The cases of exponentially suppressed magnetic field are shown as a solid lines (red for Model-1 and orange for Model-2). The black dotted line shows the distribution of sources of Green (2015).

Since both the distribution of sources and the magnetic field strength in the outer regions of the Galaxy are poorly known, we decided to explore the possibility that the strength of the magnetic field may drop faster than $1/R$ at large galactocentric distances. As a working hypothesis, we assumed the following form for the dependence of B_0 on R, at $R \gtrsim 10$ kpc:

$$B_0(R > 10\,\mathrm{kpc}) = \frac{B_\odot R_\odot}{R}\ \exp\left[-\frac{R - 10\,\mathrm{kpc}}{d}\right] \tag{5.17}$$

where the scale length d, is left as a free parameter. We found that using $d = 3.1$ kpc in Model-1 and Model-2, both the resulting CR density and spectral slope reproduce very well the results of Acero et al. (2016) in the outer Galaxy. The predictions of our calculations for this case are shown in Fig. 5.1 and Fig. 5.2.

The diffusion coefficient resulting from the non-linear CR transport in the Galaxy for Model-1 and Model-2, is shown in Fig. 5.3 and in Fig. 5.4 respectively, for different Galactocentric distances. It is interesting to notice that in both cases, at all values of R (and especially at the Sun position) $D(p)$ is almost momentum independent at $p \lesssim 10$ GeV/c. This reflects the fact that at those energies the transport is equally contributed by both advection and diffusion, as discussed above. This trend, that comes out as a

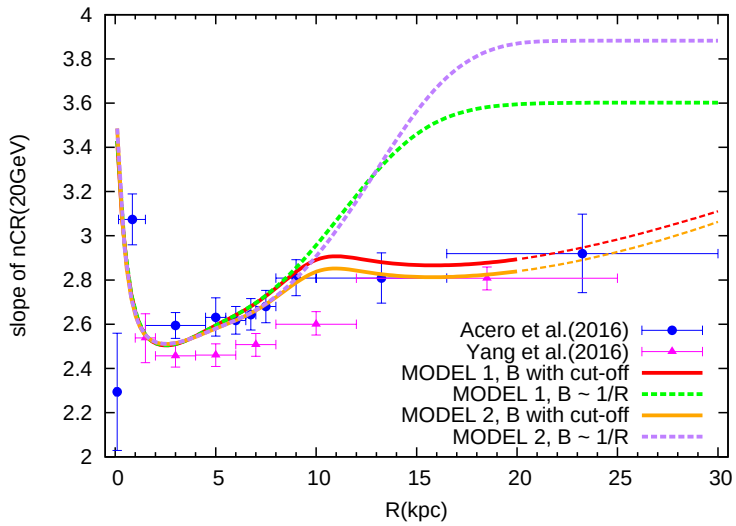

Figure 5.2: Radial dependence of the power-law index of the proton spectrum as inferred by Acero et al. (2016) and Yang et al. (2016). Our predicted slopes for Model-1 and Model-2 are shown. The cases of exponentially suppressed magnetic field are shown as a solid lines (red for Model-1 and orange for Model-2).

natural consequence of the calculations, is remarkably similar to the one that in numerical approaches to CR transport is imposed by hand in order to fit observations.
Contrary to a naive expectation, in the case in which $B_0(R)$ drops exponentially, the diffusion coefficient becomes smaller in the external part of the Galaxy than in the inner part, in spite of the smaller number of sources in the outer Galaxy. This counterintuitive result is due to the fact that $D_{\rm H}(p) \propto B_0^4/Q_0^2$ (see Eq. 5.12) and that both B_0 and Q_0 are assumed to drop exponentially at large R. Clearly, this result loses validity when $\delta B/B_0$ approaches unity and the amplification enters the non linear regime. Using Eq. 5.7, such condition in the disk can be written as $\mathcal{F}(z=0,k) \approx D_B/(2v_A H) \gtrsim 1$ which, for 1 GeV particles occurs at $R \gtrsim 20$ kpc (red-dashed and orange-dashed lines in Fig. 5.1 and Fig. 5.2). In any case, the density of CRs at large Galactocentric distances drops down, as visible in Fig. 5.1.

It is worth recalling that the model presented here has been applied to CR protons responsible for the production of γ-rays of energy ~ 2 GeV, as observed by *Fermi*-LAT , namely protons with energy of order ~ 20 GeV. Nevertheless, this model can also be tested by applying it to the study of the

CR density gradient and slope for CR protons of higher energies ($\gtrsim$ 20 GeV). In particular, we expect that, since the effect of advection is less prominent at higher energies, the spectral slope shows a weaker dependence on the Galactocentric distance.

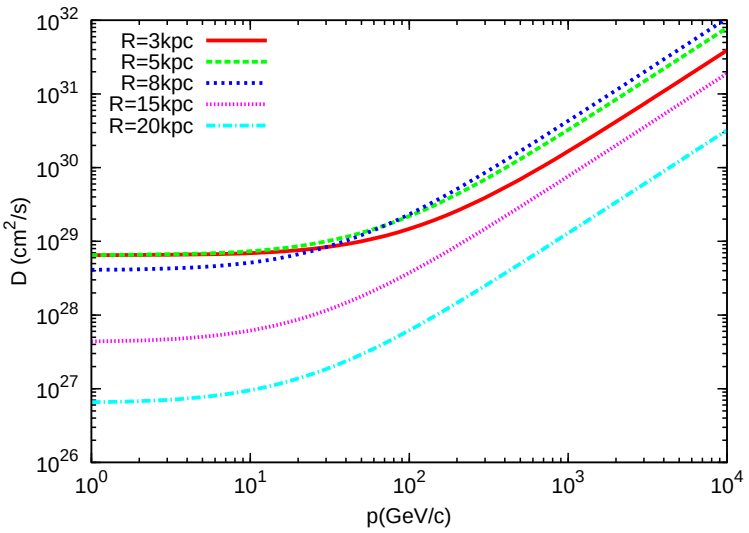

Figure 5.3: Model-1: diffusion coefficient $D(z = 0, p)$ as a function of momentum in GeV/c for different Galactocentric distances as labelled.

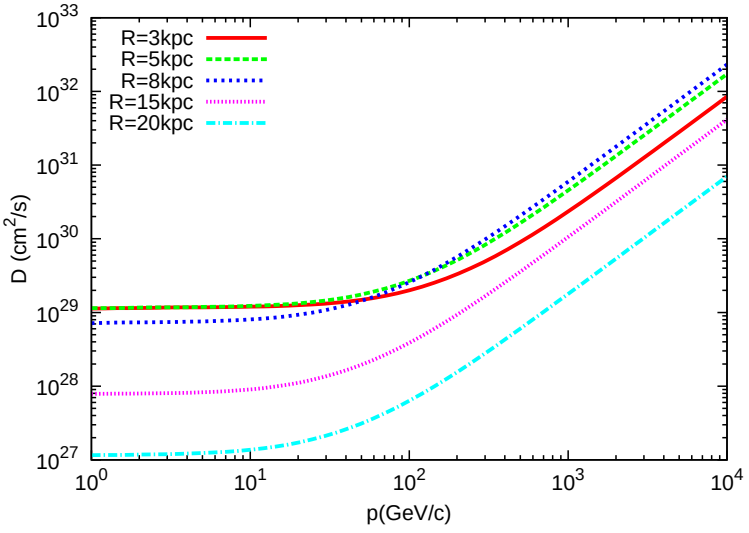

Figure 5.4: Model-2: diffusion coefficient $D(z = 0, p)$ as a function of momentum in GeV/c for different Galactocentric distances as labelled.

5.2 The effect of Galactic winds

In this section we consider the effect of the possible presence of CR-driven winds on the radial distribution of CRs. In order to better highlight such effect, we considered the same parameters of Model-2, namely we assumed the gas density $n_0 = 6 \times 10^{-3}\text{cm}^{-3}$, the magnetic field orthogonal to the Galactic plane at the Sun position $B_{0\odot} = 1\mu\text{G}$ and the CR injection slope $\gamma = 4.3$. In addition, we fixed the gas temperature to $T_0 = 2 \times 10^6$ K. With such assumptions, we study how the CR radial distribution and spectral slope change compared to the case without winds. We carried out such study by considering all the three DM halo profiles (NFW-Sofue, Burkert and Innanen) used in this thesis. The parameters of Model-1 were not used in this analysis because the gas density corresponding to the warm ionized gas component of the ISM is quite large and for such density it was not possible to launch winds anywhere in Galaxy. Notice that the parameters of Model-2 at the Sun position have also been used in the wind models illustrated in Sec. 4.3 and are inferred from observations (see Sec. 3.2). The spectrum obtained with such parameters and for the NFW-Sofue, Burkert and Innanen DM profiles are shown in Fig. 4.8(a), 4.8(b) and 4.8(c) respectively.
Similarly to what we did for the scenario without winds, we normalize the CR injection spectrum at the Sun position in order to reproduce the observed CR spectrum at 50 GeV and we consider the same radial dependence of the CR source distribution and of the Galactic magnetic field, while we assume that both the gas density and temperature along the Galactic plane do not depend on the Galactocentric distance.

For the chosen parameters the wind is not launched at $\text{R} \gtrsim 10$ kpc, for all three DM halo profiles, irrespective of the magnetic field radial dependence in such region. This means that with the present scenario it is not possible to explain the observed CR radial distribution and slope in a consistent picture.
Of course this result depends on the choice of the parameters, in particular on the assumption that the gas density and temperature be independent on R. The situation may substantially change if, for instance, we consider a more complicated scenario in which also the gas density and temperature depend on R, in agreement with observations (see e.g Miller & Bregman (2015)).
However, since here we want to illustrate the qualitative effect of winds compared to the scenario without winds, we decided to leave such dependence of the gas density and temperature out of the analysis.

For $\text{R} \lesssim 10$ kpc the possibility to launch a wind and the wind properties strongly depend on the structure of the DM halo. Looking for instance at

Fig. 5.5, we can see that for the NFW-Sofue profile the wind is launched only in the ring 5-10 kpc, while for the BUR and INN profiles winds are launched up to the very inner Galaxy, R $\sim$ 0.1-0.7 kpc. This is due to the fact that, as shown in Fig. 3.1(b), the NFW-Sofue profile shows a much larger acceleration than the Burkert and Innanen profiles at low R.

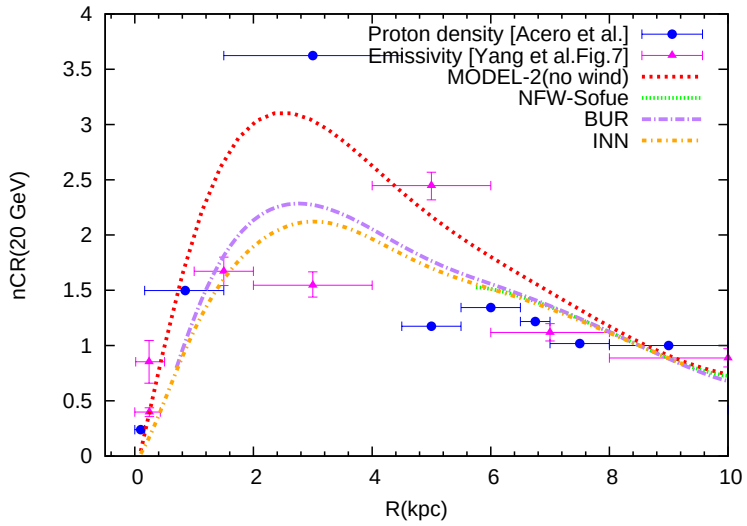

Figure 5.5: CR density at $E > 20$ GeV from Acero et al. (2016) and Yang et al. (2016) as a function of the Galactocentric distance, as labelled. Our predicted CR density at $E > 20$ GeV for Model-2, NFW-Sofue, BUR and INN are shown.

In Fig. 5.7 we show the Alfvén speed for Model-1 and Model-2, and the total advection velocity at the wind base for the NFW-Sofue, BUR and INN halo profiles. The Alfvén speed at the wind base for these three cases is the same as in Model-2: for all the three DM halo models the Alfvén speed is dominant at the wind base. The INN profile, for which the gravitational acceleration is smaller compared to the NFW-Sofue and BUR, shows a larger launching velocity at all R (see Sec. 3.3). For both BUR and INN profiles, u_0 is peaked around $\sim 2-4$ kpc. In fact, the role of the wind is mostly important in this region and results in a CR distribution generally flatter in R compared to the cases without winds, due to a larger CR advection velocity.

This is clearly visible in Fig. 5.5, where we see also that, with the addition of winds to Model-2, the peak in the CR distribution (at R $\sim$ 3 kpc in Acero et al. (2016), at R $\sim$ 5 kpc in Yang et al. (2016)) is not well reproduced, although the agreement with the other data points remains good.
In Fig. 5.6 we also show the slope of the CR spectrum as a function of R. The trend of such slope with the Galactocentric distance can be explained

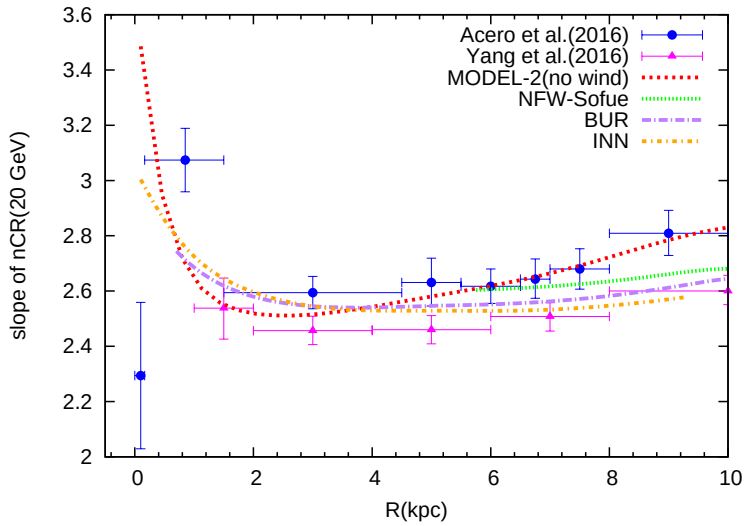

Figure 5.6: Radial dependence of the power-law index of the proton spectrum as inferred by Acero et al. (2016) and Yang et al. (2016). Our predicted slopes for Model-2, NFW-Sofue, BUR and INN are shown.

by considering the relative importance of advection and diffusion, similarly to the scenario without winds. Notice that, in general, an increase of the advection velocity results in a decrease on the CR density, which in turn causes an increase of the self-generated diffusion coefficient. For this reason, in the presence of self-generated turbulence, an increase of the CR advection velocity does not necessarily lead to an increase of the transition energy between advection and diffusion dominated CR transport. In such scenario, a larger advection velocity may not result in a flattening of the spectrum.
This can be seen in the plot of the spectral slope as a function of R, Fig. 5.6, when comparing such slope for Model-2 (no winds) and for the models with winds. In fact, the CR density in the presence of winds is smaller compared to Model-2, especially in the region R $\lesssim$ 6 kpc, and the self-generated diffusion coefficient is larger. Below R $\sim$ 4 kpc, such increase of the diffusion coefficient in the presence of winds dominated over the larger advection due to winds, leading to a spectrum steeper than in Model-2. The trend is reversed between R $\sim$ 4-7 kpc, where the larger advection velocity dominates over the increase of the diffusion coefficient and the CR spectrum is systematically harder than in Model-2.
For this reason, in the region R $\sim$ 6-10 kpc, Model-2 predicts slopes which are in remarkably good agreement with Acero et al. (2016), while the BUR and INN models predict slopes which are in good agreement with Yang et al. (2016), that report a harder CR spectrum compared to Acero et al. (2016).

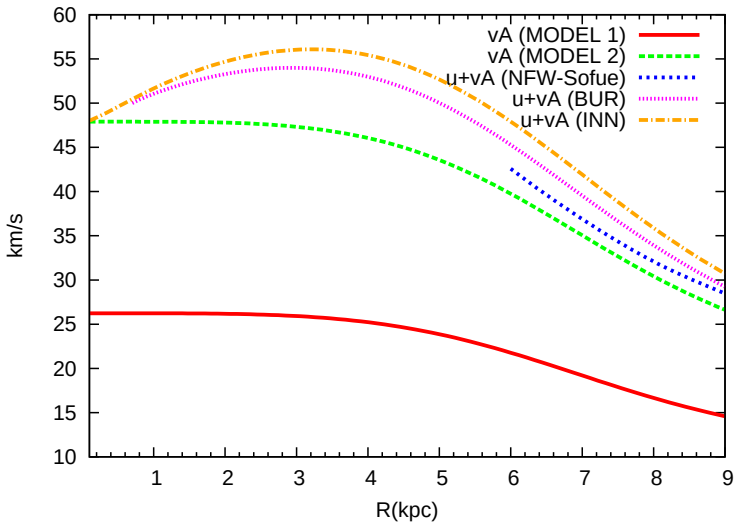

Figure 5.7: Alfvén speed for Model-1 and Model-2. Total advection velocity at the wind base for NFW-Sofue, BUR and INN. The Alfvén speed at the wind base for these three cases is the same of Model-2.

In summary, we studied the radial distribution and the spectral slope of CRs in the Galaxy as inferred from the observed diffuse $\gamma-$ray emission from the Galactic disk. In particular, we considered CRs of energy $\sim$ 20 GeV, responsible for the production of photons of $\sim$ 2 GeV, detected by *Fermi*-LAT and analyzed by Acero et al. (2016) and Yang et al. (2016). The qualitative behavior inferred for the CR density and slope is similar for the two analysis: the CR density shows a peak in the inner Galaxy (in the region $R \sim$ 3-5 kpc) and becomes practically flat in R in the outer Galaxy ($R \gtrsim 10$ kpc), while the spectrum shows a gradual steepening when moving from the inner to the outer Galactic region. Such CR gradient is hard to explain in standard Galactic CR transport models.
Here we showed that both the CR density and spectral slope can be explained in the framework of a nonlinear CR propagation model in which the CR transport is due to diffusion on self-generated waves and to advection with the same waves. In this scenario, the diffusion coefficient is smaller where the source density is larger, thus enhancing the CR density in the inner Galaxy. In the outer Galaxy, the data can be well explained only by assuming that the background magnetic field drops exponentially at R $\gtrsim$ 10 kpc with a suppression scale of $\sim$ 3 kpc. The data on the spectral slope can be explained as a result of the fact that at different R the spectrum at a given energy ($\sim$ 20 GeV in the present case) may be dominated by advection (harder spectrum) or diffusion (softer spectrum). With the addition of CR-driven winds, the

scenario is more complex because we find that in the outer Galaxy (R $\gtrsim$ 10 kpc) the wind is not launched, while in the inner Galaxy the possibility to launch winds and the wind properties strongly depends on the assumption on the DM halo model. Thus, in the presence of winds it is more difficult to accommodate the data in a consistent picture. The effect of the larger advection velocity in the presence of winds compared to the model without winds is to reduce the peak of the CR density in the inner Galaxy and leads to a spectrum which is systematically flatter compared to the case without winds at R $\gtrsim$ 4 kpc.

Is is worth to stress that the wind properties, and in particular the fact that the wind is not launched in the outer Galactic region, strongly depend on the choice of the environmental parameter, especially on the gas density and temperature. Here, in order to make the analysis easier to interpret we only considered the radial dependence of the CR source distribution and of the magnetic field. However, a more complete study should also include the possible radial dependence of the halo density and temperature. With such radial dependence, the wind may be launched also in the outer Galactic region.

Finally, notice that here we only considered CRs of energy $\sim$ 20 GeV, but observations of the diffuse $\gamma-$ray emission also provide information on the radial distribution and slope of CRs of higher energies. A simple prediction of our calculations is that at higher energies, for which diffusion dominates over advection at all R, the spectral hardening due to advection should disappear.

Conclusions

In this thesis we developed a semi-analytical calculation of the structure of a CR-driven Galactic wind that allows to determine the hydrodynamical structure of the wind (velocity and pressure of the plasma), and at the same time the distribution function of CRs at any location in the disc or in the wind region. The transport of CRs is described as advective and diffusive. Diffusion is due to scattering off self-generated Alfvén waves, excited by the same CRs due to streaming instability, while advection is due to the self-generated waves and to the wind.
Most of current models of CR Galactic propagation assume that CR transport properties are the same in the whole Galaxy and that they do not depend on the CR distribution. However, CR transport is affected by the properties of the ISM and by the dynamical action that CRs themselves exert on the environment. Due to the CR density gradient between the Galactic disk and the halo, CRs can excite the streaming instability, leading to the generation of Alfvén waves which move in the direction of the decreasing CR density (see e.g Skilling (1975); Holmes (1975)). CR scattering off self-generated waves affects the CR diffusive properties, while advection with such waves influences their convective transport (see Blasi et al. (2012); Aloisio & Blasi (2013)). Moreover, CRs escaping from the Galaxy exert a force, $-\nabla P_c$, directed away from the disk and opposite to the Galactic gravitational force (which is the result of the gravitational contribution of the Galactic bulge and disk and of the Dark Matter halo). If this force is larger than the gravitational pull it can lift ionized gas from the disk and launch a wind. The possible presence of Galactic winds would have an important impact both on the CR convective motion and on the evolution and ecology of the Galaxy.
The dynamics of CR-driven winds and the CR transport in such winds, including the self-generation of plasma waves, is intrinsically non linear, since the CR density gradient is responsible for the generation of the Alfvén waves and of the wind which together determine the CR transport.
CR-driving has been widely recognized as an appealing mechanism for wind formation in the Milky Way (see e.g Ipavich (1975); Breitschwerdt et al. (1991)) and the hydrodynamics of Galactic CR-driven winds has been extensively studied (see e.g Breitschwerdt et al. (1991); Everett et al. (2008)),

while no information was retained on the CR spectrum. Nevertheless the CR spectrum provides a strong constraint for Galactic wind models and its prediction is crucial in the study of CR-driven Galactic winds. The first, and, to our knowledge, the only attempt to account for both CR-driven winds and their effects of the CR transport was made by Ptuskin et al. (1997). The authors used a simplified approach to the characteristics of the wind to infer some general implications for the spectrum of CRs. However, their method is too simplified and is not able to predict the CR spectrum in a CR-driven wind with accuracy.

In this thesis we developed a semi-analytical technique which allows to determine at the same time the properties of a CR-driven wind (velocity, density and temperature of the plasma) and the corresponding distribution function of CRs. In our approach CRs diffuse by means of self-generated Alfvén waves and advect along the direction of the same self-generated waves and with the wind. The diffusion coefficient is calculated from the spectrum of waves exited by streaming instability and locally damped through non linear Landau damping.
In agreement with previous calculations of the hydrodynamics of CR-driven winds, we found that CRs can drive winds in our Galaxy. The possibility to launch a wind and the wind properties, strongly depend on the conditions of the ISM. The latter are constrained by observations and depend on the location considered in the Galaxy. For instance, the Galactic gravitational potential and, in particular, the contribution of the DM halo, changes appreciably depending on the position in the Galaxy. Contrary to previous calculations, we also computed the CR distribution function in a CR-driven wind, and in particular we computed the CR spectrum observed at Earth. We found that in many cases, winds launched with parameters compatible with the observed ISM properties in the vicinity of the Sun lead to a CR spectrum which is not in agreement with observations. This is mainly due to the fact that CR advection in such winds is strong, leading to spectra at low energies which are harder than the observed spectrum. At high energy, instead, the wind expansion, together with the steep energy dependence of the self-generated diffusion coefficient, leads to spectra which are steeper than the observed spectrum. However, these conclusions strongly depend on the wind launching parameters and on the physical conditions in the near-disk region (in particular on the amount and on the filling factor of the neutral gas). The presence of pre-existing turbulence in the near-disk region can lead to a spectral hardening in the high energy part of the spectrum, in agreement with observations.
Both the CR density and spectral slope in the Galaxy, as inferred by the $\gamma-$ray emission in the Galactic disk, change appreciably as functions of the Galactocentric distance. This finding is difficult to explain in the framework of most current models of CR propagation, which assume that the CR trans-

port properties are the same in the whole Galaxy. Several empirical models have been proposed which relax the assumption of spatially constant diffusion coefficient and try to reproduce the CR spatial gradient, however, the problem of these approaches is the lack of a physical motivation to justify the assumed spatial dependence of the CR transport properties. On the other hand, the CR propagation in the presence of self-generated waves and, possibly, of CR-driven winds, naturally provides, trough the radial dependence of the properties of the ISM, a spatial dependence for the CR transport properties. In fact, we found that it is possible to reproduce the observed radial dependence of the CR density and spectral slope in the framework of our non linear CR propagation model.

The technique developed here is very general and can be extended to study the possible existence of CR-driven winds and their implications, both for the Milky Way and for other galaxies.
In the present work we focused on the propagation of CR protons. However, with the addition of spallation and nuclear decay terms in the transport equation, it is possible to study also the effect of CR-driven winds on the propagation of heavier nuclei and the implications for important observables such as the B/C ratio.
An additional possible development of this work concerns the Galactic termination shock. In fact, in the presence of Galactic winds, the hot supersonic plasma ejected from the disk will eventually impinge on the IGM and create a shock. Analogously to what happens at SN shocks, CRs can be accelerated at the wind termination shock and may even reach very high energies in this reacceleration process. This may have important implications on the observed spectrum, especially on the transition from Galactic to extragalactic CRs. From the technical point of view, a termination shock can be included in our calculation of the CR transport as a discontinuity in the advection velocity.
Galactic winds can eject several $M_{\odot}/\mathrm{yr}$ and can transport hot ionized plasma and metals from the disk to the outer halo. According to our results, the estimated mass loss rate for the Milky Way is of the order of $\sim 1\, M_{\odot}/\mathrm{yr}$. Considering that the star formation rate in the Milky Way is also $\sim 1\, M_{\odot}/\mathrm{yr}$, one can easily understand that galactic winds are of crucial importance in modeling the evolution of both our Galaxy and other galaxies. This conclusion acquires even more importance if we recall that galactic models usually overpredict the star formation rate unless some mechanism able to subtract gas from the galaxy is included. In addition, due to processes of charge exchange, the neutral gas in the ISM can couple to the ionized gas and may also be transported away from the disk. This would have important implications for CR transport (due to wave damping by ion-neutral friction), for the star formation rate and for the properties of the halo (such as the chemical composition and the cooling rate).

An important limitation of our work is that we only considered stationary outflows. This simplification can be considered a good approximation in many cases and is helpful in developing an understanding of the CR-driven wind problem, but can also be used to check more sophisticated time-dependent approaches. Notice however that our stationary computation may be inadequate in describing important types of flows which may take place in our Galaxy (or in other galaxies). For instance, this may be the case of the so called "galactic fountains" which happen when some gas is ejected from the disk due to thermal and CR pressure gradients, but then it cools down in the halo and falls back. In addition, an interesting aspect of time dependent winds is the possible formation of multiple termination shocks propagating through the halo at which CRs may be reaccelerated to very high energies. In summary, the calculation developed here is very general and can be applied to a variety of problems concerning the formation of CR-driven winds and the related CR transport. Moreover, our work paved the way to more complex studies involving time dependent flows.

Bibliography

Acero F., et al., 2016, preprint, (arXiv:1602.07246)

Ackermann M., et al., 2011, ApJ, 726, 81

Ackermann M., et al., 2012, A&A, 538, A71

Adriani O., et al., 2011, Science, 332, 69

Aguilar M., et al., 2015, Physical Review Letters, 114, 171103

Aloisio R., Blasi P., 2013, J. Cosmology Astropart. Phys., 7, 001

Aloisio R., Blasi P., Serpico P. D., 2015, Astronomy & Astrophysics, 583, A95

Anderson M. E., Bregman J. N., 2010, The Astrophysical Journal, 714, 320

Baade W., Zwicky F., 1934, Proceedings of the National Academy of Science, 20, 254

Berezinskii V. S., Bulanov S. V., Dogiel V. A., Ptuskin V. S., 1990, Astrophysics of cosmic rays

Bernardo G. D., Evoli C., Gaggero D., Grasso D., Maccione L., 2010, Astroparticle Physics, 34, 274

Bertone G., Hooper D., Silk J., 2005, Phys. Rep., 405, 279

Bhat C. L., Mayer C. J., Rogers M., Wolfendale A. W., Zan M., 1986, Journal of Physics G Nuclear Physics, 12, 1087

Blasi P., 2013, Astron. Astrophys. Rev., 21, 70

Blasi P., 2014, Nucl. Phys. Proc. Suppl., 256-257, 36

Blasi P., Amato E., Serpico P. D., 2012, Physical Review Letters, 109, 061101

Bloemen J. B. G. M., et al., 1986, A&A, 154, 25

Booth C. M., Agertz O., Kravtsov A. V., Gnedin N. Y., 2013, ApJ, 777, L16

Breitschwerdt D., Schmutzler T., 1994, Nature, 371, 774

Breitschwerdt D., Schmutzler T., 1999, A&A, 347, 650

Breitschwerdt D., McKenzie J. F., Voelk H. J., 1991, A&A, 245, 79

Breitschwerdt D., McKenzie J. F., Voelk H. J., 1993, Astronomy and Astrophysics (ISSN 0004-6361), 269, 54

Burkert A., 1995, ApJ, 447, L25

Case G. L., Bhattacharya D., 1998, ApJ, 504, 761

Cheng K.-S., Chernyshov D. O., Dogiel V. A., Ko C.-M., Ip W.-H., 2011, ApJ, 731, L17

Chevalier R. A., Clegg A. W., 1985, Nature, 317, 44

Cox D. P., 2005, Annual Review of Astronomy and Astrophysics, 43, 337

Crain R. A., Eke V. R., Frenk C. S., Jenkins A., McCarthy I. G., Navarro J. F., Pearce F. R., 2007, MNRAS, 377, 41

Dalgarno A., McCray R. A., 1972, ARA&A, 10, 375

Dorfi E. A., Breitschwerdt D., 2012, A&A, 540, A77

Dougherty K. M., Breitschwerdt D., Völk J. H., 1990, International Cosmic Ray Conference, 3, 319

Erlykin A. D., Wolfendale A. W., Dogiel V. A., 2016, Advances in Space Research, 57, 519

Everett J. E., Zweibel E. G., 2011, The Astrophysical Journal, 739, 60

Everett J. E., Zweibel E. G., Benjamin R. A., McCammon D., Rocks L., Gallagher J. S., 2008, The Astrophysical Journal, 674, 258

Evoli C., Gaggero D., Grasso D., Maccione L., 2012, Physical Review Letters, 108, 211102

Faucher-Giguère C.-A., Kaspi V. M., 2006, ApJ, 643, 332

Ferrière K. M., 2001, Reviews of Modern Physics, 73, 1031

Ferriere K. M., Zweibel E. G., Shull J. M., 1988, ApJ, 332, 984

Gaggero D., Urbano A., Valli M., Ullio P., 2015a, Phys. Rev. D, 91, 083012

Gaggero D., Grasso D., Marinelli A., Urbano A., Valli M., 2015b, ApJ, 815, L25

Ginzburg V. L., Syrovatsky S. I., 1961, Progress of Theoretical Physics Supplement, 20, 1

Girichidis P., et al., 2016, ApJ, 816, L19

Green D. A., 2015, MNRAS, 454, 1517

Holmes J. A., 1975, Royal Astronomical Society, 170, 251

Hunter S. D., et al., 1997, ApJ, 481, 205

Innanen K. A., 1973, Ap&SS, 22, 393

Ipavich F. M., 1975, Astrophysical Journal, 196, 107

Irrgang A., Wilcox B., Tucker E., Schiefelbein L., 2013, A&A, 549, A137

Jansson R., Farrar G. R., 2012, ApJ, 757, 14

Jones T. W., 1993, ApJ, 413, 619

Kalberla P. M. W., Dedes L., 2008, A&A, 487, 951

King A., Pounds K., 2015, ARA&A, 53, 115

Kulsrud R. M., Cesarsky C. J., 1971, Astrophys. Lett., 8, 189

Lacki B. C., 2014, MNRAS, 444, L39

Lamers H. J. G. L. M., Cassinelli J. P., 1999, Introduction to Stellar Winds:. Cambridge University Press, Cambridge, doi:10.1017/CBO9781139175012, https://www.cambridge.org/core/books/introduction-to-stellar-winds/6E24600EDAD99F2B7839BBA190C115C0

Martin C. L., Shapley A. E., Coil A. L., Kornei K. A., Bundy K., Weiner B. J., Noeske K. G., Schiminovich D., 2012, The Astrophysical Journal, 760, 127

Maurin D., Melot F., Taillet R., 2014, A&A, 569, A32

Miller M. J., Bregman J. N., 2015, The Astrophysical Journal, 800, 14

Miyamoto M., Nagai R., 1975, PASJ, 27, 533

Murray N., Quataert E., Thompson T. A., 2005, ApJ, 618, 569

Navarro J. F., Frenk C. S., White S. D. M., 1996, ApJ, 462, 563

Nesti F., Salucci P., 2013, J. Cosmology Astropart. Phys., 7, 016

Parker E. N., 1965, Space Sci. Rev., 4, 666

Ptuskin V., 2006, Journal of Physics: Conference Series, 47, 113

Ptuskin V. S., Zirakashvili V. N., 2003, A&A, 403, 1

Ptuskin V. S., Voelk H. J., Zirakashvili V. N., Breitschwerdt D., 1997, A&A, 321, 434

Recchia S., Blasi P., Morlino G., 2016a, Monthly Notices of the Royal Astronomical Society

Recchia S., Blasi P., Morlino G., 2016b, Monthly Notices of the Royal Astronomical Society: Letters

Ruszkowski M., Yang H.-Y. K., Zweibel E., 2016, preprint, (arXiv:1602.04856)

Salem M., Bryan G. L., 2014, MNRAS, 437, 3312

Salucci P., Nesti F., Gentile G., Frigerio Martins C., 2010, A&A, 523, A83

Scoville N., 2003, Journal of Korean Astronomical Society, 36, 167

Skilling J., 1971, Astrophysical Journal, 170, 265

Skilling J., 1975, MNRAS, 173, 255

Sofue Y., 2012, PASJ, 64

Stanev T., 1997, ApJ, 479, 290

Stecker F. W., Jones F. C., 1977, ApJ, 217, 843

Strong A. W., Mattox J. R., 1996, A&A, 308, L21

Strong A. W., Moskalenko I. V., Reimer O., Digel S., Diehl R., 2004, A&A, 422, L47

Tomassetti N., 2012, ApJ, 752, L13

Uhlig M., Pfrommer C., Sharma M., Nath B. B., Enßlin T. A., Springel V., 2012, MNRAS, 423, 2374

Veilleux S., Cecil G., Bland-Hawthorn J., 2005, ARA&A, 43, 769

Walker M. A., 2016, ApJ, 818, 23

Wolfire M. G., McKee C. F., Hollenbach D., Tielens A. G. G. M., 2003, ApJ, 587, 278

Yang R.-z., Aharonian F., Evoli C., 2016, preprint, (arXiv:1602.04710)

Zhou Y., Matthaeus W. H., 1990, J. Geophys. Res., 95, 10291

Zirakashvili V., Voelk H., 2006, Advances in Space Research, 37, 1923

Zirakashvili V. N., Breitschwerdt D., Ptuskin V. S., Voelk H. J., 1996, A&A, 311, 113

Zubovas K., King A. R., Nayakshin S., 2011, MNRAS, 415, L21

Appendix A

Derivation of the hydrodynamic equations

In this section we derive the hydrodynamic equations used throughout this paper. They describe the macroscopic behaviour of the thermal plasma and CRs and their mutual interactions. As we already pointed out in Chapter 2, the wave component is not present in these equations because we are assuming that all Alfvén waves (generated through CR streaming instability) are locally dumped on short time scales, so that the energy fed by CRs into waves just results in the heating of the gas. Here we are also neglecting any external loss of mass, momentum and energy. A general form of those equations, with and without damping of waves, is reported in Breitschwerdt et al. (1991).

A.1 Gas mass conservation and equation of motion

In absence of any mass and momentum external loss, the time dependent gas mass conservation and equation of motion read

$$\frac{D\rho}{Dt} = -\rho\vec{\nabla}\cdot\vec{u}, \tag{A.1}$$

$$\rho\frac{D\vec{u}}{Dt} = -\vec{\nabla}(P_g + P_c) - \rho\vec{\nabla}\Phi, \tag{A.2}$$

where ρ, $\vec{u}$, P_g, P_c and Φ are the gas density, velocity and pressure, the CR pressure and the galactic gravitational potential respectively. $D/Dt = \partial/\partial t + \vec{u}\cdot\vec{\nabla}$ is the convective derivative.

A.2 Gas internal energy and total energy

The internal energy of the gas in a volume V is given by

$$\epsilon_g = \frac{PgV}{\gamma_g - 1} \tag{A.3}$$

and its time evolution is given by

$$\frac{D\epsilon_g}{Dt} = -Pg\frac{DV}{Dt} - \vec{v}_A \cdot \vec{\nabla} P_c V \tag{A.4}$$

where on the right hand side we find the work done on the gas when V changes and the energy input due to damping of the self generated Alfvén waves. In fact, as it will be shown in Sec. A.4, the hydrodynamic counterpart of the CR streaming instability is given by the term $\vec{v}_A \cdot \vec{\nabla} P_c$, where $\vec{v}_A$ is the Alfvén speed and P_c the CR pressure. In terms of ρ, and using Eq. A.1, we get

$$\frac{D}{Dt}\left(\frac{Pg}{\gamma_g - 1}\frac{1}{\rho}\right) = -\frac{P_g}{\rho}\vec{\nabla} \cdot \vec{u} - \frac{1}{\rho}\vec{v}_A \cdot \vec{\nabla} P_c. \tag{A.5}$$

The gas total energy per unit volume is the sum of the kinetic and internal energy per unit volume

$$\epsilon = \frac{1}{2}\rho u^2 + \frac{Pg}{\gamma_g - 1}. \tag{A.6}$$

Making use of Eq. A.1, A.2 and A.5, we get the equation for the gas total energy

$$\begin{aligned}\frac{D}{Dt}\left(\frac{1}{2}\rho u^2 + \frac{Pg}{\gamma_g - 1}\right) = &-\vec{\nabla} \cdot \vec{u}\left(\frac{1}{2}\rho u^2 + \frac{\gamma_g Pg}{\gamma_g - 1}\right) \\ &- \vec{u} \cdot \vec{\nabla}(P_g + P_c) - \vec{v}_A \cdot \nabla P_c - \rho \vec{u} \cdot \vec{\nabla}\Phi.\end{aligned} \tag{A.7}$$

A.3 CR energy

The time dependent CR transport equation reads

$$\frac{\partial f}{\partial t} + (\vec{u} + \vec{v}_A) \cdot \vec{\nabla} f = \vec{\nabla} \cdot \left[D\vec{\nabla} f\right] + \left[\vec{\nabla} \cdot (\vec{u} + \vec{v}_A)\right] \frac{p}{3}\frac{\partial f}{\partial p} \tag{A.8}$$

where f is the CR distribution function and D the CR diffusion coefficient. We also introduce the CR energy density and pressure

$$\epsilon_c = \int_0^\infty dp\, 4\pi p^2 T(p) f(z,p), \tag{A.9}$$

$$P_c = \int_0^\infty dp\, \frac{4\pi}{3} p^2 p v f(z,p), \tag{A.10}$$

where $T(p) = \sqrt{p^2c^2 + (mc^2)^2} - mc^2$ is the kinetic energy. Multiplying the transport equation by $4\pi\ p^2 T(p)$ and integrating in p we get

$$\frac{\partial \epsilon_c}{\partial t} + (\vec{u} + \vec{v}_A) \cdot \vec{\nabla} \epsilon_c = \vec{\nabla} \cdot \left[\overline{D} \vec{\nabla} \epsilon_c \right] + \\ + \vec{\nabla} \cdot (\vec{u} + \vec{v}_A) \int_0^\infty \frac{4}{3} \pi dp p^3 T(p) \frac{\partial f}{\partial p}, \tag{A.11}$$

where we introduced the average diffusion coefficient

$$\overline{D}(z) = \frac{\int_0^\infty dp\ 4\pi p^2 T(p) D(z,p) \vec{\nabla} f}{\int_0^\infty dp\ 4\pi p^2 T(p) \vec{\nabla} f}. \tag{A.12}$$

The last integral can be performed by parts, using the fact that $dT(p)/dp = v$. After rearranging terms and introducing the effective CR adiabatic index $\epsilon_c = P_c/(\gamma_c - 1)$ we obtain:

$$\frac{\partial \epsilon_c}{\partial t} + \vec{\nabla} \cdot \left[(\vec{u} + \vec{v}_A) \frac{\gamma_c P_c}{\gamma_c - 1} \right] = \vec{\nabla} \cdot \left[\overline{D} \frac{\vec{\nabla} P_c}{\gamma_c - 1} \right] + (\vec{u} + \vec{v}_A) \cdot \vec{\nabla} P_c. \tag{A.13}$$

A.4 Wave energy

The time evolution of the Alfvén wave spectral energy density $W(\vec{z}, p)$, taking into account wave advection by the thermal plasma and wave generation by CR streaming instability, is given in Jones (1993)

$$\frac{\partial W}{\partial t} + \vec{\nabla} \cdot \left[\left(\frac{3}{2} \vec{u} + \vec{v}_A \right) W \right] = \frac{1}{2} \vec{u} \cdot \vec{\nabla} W - \Gamma_{\rm CR} W \tag{A.14}$$

where Γ_{CR} (see also Eq. 2.20) is the wave growth rate due to CR streaming instability (k is the wave number and B_0 the average magnetic field)

$$\Gamma_{\rm CR} = \frac{16\pi^2}{3} \frac{\vec{v}_A}{k W B_0^2} \cdot \int_0^\infty dp p^4 v(p) \delta \left(p - \frac{q B_0}{kc} \right) \vec{\nabla} f. \tag{A.15}$$

We also define the wave energy density and pressure

$$\epsilon_w = \int_{k_0}^\infty \frac{{B_0}^2}{4\pi} W(z,k) dk \tag{A.16}$$

$$P_w = \frac{\epsilon_w}{2}. \tag{A.17}$$

The hydrodynamic version of the wave equation can be obtained by integrating in $\int_{k_0}^{\infty} \frac{{B_0}^2}{4\pi} dk$. The integration of the streaming instability term gives

$$\begin{aligned}
&\int_{k_0}^{\infty} \frac{{B_0}^2}{4\pi} \Gamma_{\rm CR} W(z,k) dk \qquad (A.18)\\
&= \int_0^{\infty} \int_{k_0}^{\infty} \frac{4\pi}{3} \frac{\vec{v}_A}{k} \cdot \vec{\nabla} f p^4 v(p)\, \delta\left(p - \frac{qB_0}{kc}\right) dpdk \\
&= \int_0^{\infty} \int_{k_0}^{\infty} \frac{4\pi}{3} \vec{v}_A \cdot \vec{\nabla} f p^4 v(p) \frac{kc}{qB_0}\, \delta\left(k - \frac{qB_0}{pc}\right) dpdk \\
&= \vec{v}_A \cdot \vec{\nabla} \int_0^{\infty} \frac{4\pi}{3} f v(p) p^3 dp \\
&= \vec{v}_A \cdot \vec{\nabla} P_c
\end{aligned}$$

where we used the properties of the Dirac's delta and the definition of P_c given in Eq. A.10. Finally, the equation for the wave energy is

$$\frac{\partial \epsilon_w}{\partial t} + \vec{\nabla} \cdot \left[(3\vec{u} + 2\vec{v}_A)\, P_w \right] = \vec{u} \cdot \vec{\nabla} P_w - \vec{v}_A \cdot \vec{\nabla} P_c. \qquad (A.19)$$

In our approach we assume that all generated waves are locally and immediately dumped, so that the hydrodynamic equation for waves is not necessary. On the other hand, the term of wave generation by CR streaming instability, $\vec{v}_A \cdot \vec{\nabla} P_c$, enters the right hand side of the equation for the gas pressure A.5 because the damped waves result in gas heating.

Appendix B

Stationary hydrodynamic equations in the flux tube

We are dealing with a steady one-dimensional flow, in which the flux tube geometry is preassigned as shown in Fig. 2.1. The stationary regime is obtained by setting $\partial/\partial t = 0$ in the hydrodynamic equations. The stationary hydrodynamic equations are listed in Chapter 2. As for the flux tube geometry, referring to Fig. 2.1, if z is the vertical coordinate and $A(z)$ the flux tube area, the divergence and gradient operators become

$$\vec{\nabla} S = \frac{dS}{dz}\hat{z} \tag{B.1}$$

$$\vec{\nabla} \cdot \vec{V} = \frac{1}{A(z)}\frac{d}{dz}\left[\vec{A}(z) \cdot \vec{V}\right]. \tag{B.2}$$

By applying this prescription for the gradient and divergence operators to the stationary equations we get

$$\rho u A = \text{const}, \tag{B.3}$$

$$AB = \text{const}, \tag{B.4}$$

$$\rho u \frac{d}{dz}\left(\frac{u^2}{2} + \Phi\right) = -u\frac{d}{dz}\left(P_g + P_c\right), \tag{B.5}$$

$$\frac{dP_g}{dz} = \gamma_g \frac{P_g}{\rho}\frac{d\rho}{dz} - (\gamma_g - 1)\frac{v_A}{u}\frac{dP_c}{dz} \tag{B.6}$$

$$\rho u A \frac{d}{dz}\left(\frac{u^2}{2} + \frac{\gamma_g}{\gamma_g - 1}\frac{P_g}{\rho} + \Phi\right) = -A(u + v_A)\frac{dP_c}{dz}, \tag{B.7}$$

$$\frac{dP_c}{dz} = \gamma_{eff}\frac{P_c}{\rho}\frac{2u + v_A}{2(u + v_A)}\frac{d\rho}{dz}. \tag{B.8}$$

In the derivation of Eq. B.8 we defined

$$\frac{\gamma_{eff}}{\gamma_{eff} - 1} = \frac{\gamma_c}{\gamma_c - 1} - \frac{\overline{D}}{(\gamma_c - 1)(u + v_A)P_c}\frac{dP_c}{dz}. \tag{B.9}$$

and we used

$$\frac{d(uA)}{dz} = -\frac{uA}{\rho}\frac{d\rho}{dz} \tag{B.10}$$

$$\frac{d(v_A A)}{dz} = -\frac{v_A A}{2\rho}\frac{d\rho}{dz}. \tag{B.11}$$

B.1 First integrals

It is possible to derive from the hydrodynamic equations two first integrals which come in handy when searching for the wind solution. The first one derives directly from the total energy conservation: summing equations 2.5 and 2.6 and moving to the flux tube geometry, we get

$$\frac{u^2}{2} + \frac{\gamma_g}{\gamma_g - 1}\frac{P_g}{\rho} + \Phi + \frac{\gamma_{eff}}{\gamma_{eff} - 1}\frac{P_c}{\rho}\frac{u + v_A}{u} = \text{const.} \tag{B.12}$$

The other first integral is obtained from Eq. B.8 when we can treat γ_{eff} as constant (this was the case in Breitschwerdt et al. (1991), where it was assumed $\overline{D} = 0$ and $\gamma_c = 4/3$). In fact, using Eq. B.10 and B.11

$$\frac{d}{dz}\left(A(u + v_A)\right) = -\frac{A(2u + v_A)}{2\rho}\frac{d\rho}{dz}, \tag{B.13}$$

thus dP_c/dz in Eq. B.8 becomes

$$\frac{dP_c}{dz} = -\gamma_{eff}\frac{P_c}{A(u + v_A)}\frac{d}{dz}\left[A(u + v_A)\right] \tag{B.14}$$

from which we finally get

$$P_c\left[A(u + v_A)\right]^{\gamma_{eff}} = \text{const.} \tag{B.15}$$

B.2 The wind equation

Starting from Eq. B.5 and using Eq. B.6 and B.8 we get the so-called wind equation, i.e an equation for the flow speed,

$$\frac{du}{dz} = u\frac{c_*^2\frac{1}{A}\frac{dA}{dz} - \frac{d\Phi}{dz}}{u^2 - c_*^2} \tag{B.16}$$

where we defined the “compound sound speed"

$$c_*^2 = \gamma_g\frac{P_g}{\rho} + \gamma_{eff}\frac{P_c}{\rho}\left[1 - (\gamma_g - 1)\frac{v_A}{u}\right]\frac{2u + v_A}{2(u + v_A)}. \tag{B.17}$$